



SAPIENZA
UNIVERSITÀ DI ROMA

Sapienza University of Rome

Department of Mechanical and Aerospace Engineering
PhD in Aeronautics and Space Engineering

THESIS FOR THE DEGREE OF DOCTOR OF PHILOSOPHY

**Multi-disciplinary design and
multi-objective optimization of
solid- and liquid- rocket based
launch vehicles**

Advisor
Prof. Franco Mastroddi

PhD candidate
Lucandrea Mancini

Co-advisor
Ing. Agostino Neri

Academic Year MMXXIII-MMXXIV (XXXVI cycle)

*To my daughter
who was born
during this PhD research*

*"Fatti non foste a viver come bruti,
ma per seguir virtute e canoscenza."*

Inferno, Canto XXVI, Dante Alighieri

Abstract

Nowadays there is a tremendous competitiveness in the space sector, especially in the production of new launch vehicles. Launch Vehicle design is a complex topic, because it requires the knowledge of different disciplines such as propulsion, structures, aerodynamics, trajectory and controls, which are strongly coupled between each others. Therefore, Multidisciplinary Design Optimization is the correct approach to study and develop new launch vehicle configurations. Each discipline requires the adoption of a proper engineering model to accurately describe its physic. Many researches have been carried out on launch vehicle design optimization. However, the exploitation of finite element model and computational fluid dynamics inside an optimization loop is still not common due to the huge computational time required to perform a structural and an aerodynamic analysis.

This thesis proposes a methodology for a fast and effective multidisciplinary design optimization using a high fidelity structural model generator, surrogate and reduced order models to accelerate the phase A of development of new launch vehicles, balancing accuracy and computational time. Indeed, the use of finite element surrogate models together with the real finite element solver enhances the process of identifying the optimal design by enabling reduction in the running time of the optimization procedure, making the finite element analysis suited for conceptual studies. While, the use of a reduced order model for aerodynamic permits to complete avoid computational fluid dynamics calculation inside the optimization loop.

More specifically, it is developed a procedure which, starting by a target payload and mission, calculates the optimal propellant distribution between the stages in order to minimize the launch vehicle mass. Then, once defined the mass budget and the external geometry, the trajectory up to target orbit is evaluated and consequently the flight loads necessary to carry out the structural analysis using both a refined finite element model and its surrogate. The multidisciplinary design optimization procedure is managed in an advanced optimization environment in order to find the best values of design variables that minimize or maximize the cost functions while respecting the mission constraints. In order to validate this methodology, two launch vehicle configurations have been studied: a three stages solid- and a two stages liquid- rocket based launch vehicle. On the three stages configuration have been firstly carried out a structural optimization and after the complete multidisciplinary optimization considering single and multiple objectives. Instead on the two stages has been performed a complete multidisciplinary design optimization cycle with two separated objectives.

Keywords: Launch Vehicle, Multidisciplinary Design Optimization, Reduced Order Models, Surrogate Models, Finite Element Method.

© 2024 Lucandrea Mancini. All rights reserved

Author's email lucandrea.mancini@uniroma1.it

Contents

List of Figures	vi
List of Tables	ix
Nomenclature	xi
Acronyms	xiii
Summary of the thesis	1
Research motivation	1
Multi-disciplinary design optimization of launch vehicle: a literature review	3
Methodology, objectives and activities description	5
Thesis outline	6
1 Multi-disciplinary Design Optimization theoretical issues	8
1.1 Multi-disciplinary Design Optimization	8
1.2 Single vs Multi Objective Optimization	9
1.3 Design of Experiments	11
1.4 Architectures	13
1.5 Methods	15
1.5.1 Genetic Algorithm	15
1.5.2 Gradient based algorithm	17
2 Launch Vehicle Design	18
2.1 Design Process	18
2.2 Orbit energy requirements and velocity losses	23
2.3 Propulsion system	25
2.3.1 Solid Rocket Motor	25
2.3.2 Liquid Rocket Engine	30
2.4 Weight estimation and preliminary sizing	32
2.4.1 Solid Rocket Motor	32
2.4.2 Liquid Rocket Engine	34
2.4.3 Interstage	36
2.4.4 Upper composite module	37
2.4.5 Avionic and wiring	37
2.5 Aerodynamic of axisymmetric bodies	37
2.5.1 Supersonic regime	38
2.5.2 Subsonic regime	44
2.6 Trajectory analysis	45
2.6.1 Gravity and atmospheric model	45
2.6.2 Ascent trajectory	46
2.7 Structural Model Generator	49

2.7.1	FE model geometry	50
2.7.2	FE model loads and load-cases	54
2.7.3	Static analysis	59
2.7.4	Buckling analysis	60
2.8	Surrogate FE model	60
3	Application cases on different Launch Vehicle Configurations	63
3.1	VEGA inspired structural optimization	63
3.2	VEGA inspired MDO	67
3.2.1	Single-objective MDO	68
3.2.2	Multi-objective MDO	80
3.3	TSTO LRE based MDO	90
3.4	MDO computational aspects	100
	Conclusion and future remarks	101
	Future developments	102
	Bibliography	104
A	Lagrangian optimizer for staging	112
B	Response Surface Models	114
B.1	Radial Basis Functions	114
B.2	Gradient Boosting Machine	115
C	Neural Network based LV aerodynamic	117

List of Figures

1	First stage SRM thrust shape.	2
1.1	Single objective.	9
1.2	Multi objective.	10
1.3	Comparison between different DOE schemes.	12
1.4	IDF architecture.	13
1.5	MDF architecture.	14
1.6	CO architecture.	14
1.7	ASO architecture.	14
1.8	GA flowchart.	16
1.9	Genetic operators.	16
1.10	Example of gradient based algorithm.	17
2.1	LV scheme.	18
2.2	Theoretical performance of a SSTO.	19
2.3	LV MDO flowchart.	21
2.4	LV MDO schematic.	21
2.5	Velocity losses of Titan IV LV	25
2.6	From burning surface to thrust.	29
2.7	Main LRE feed system.	30
2.8	From mass flow rate to thrust.	31
2.9	Example of LV profile.	39
2.10	Example of 3D aerodynamic mesh.	39
2.11	Panel angle.	39
2.12	Slender body profile.	41
2.13	Mach's anti-cone projection for two different Mach numbers.	42
2.14	Comparison between CFD and analytic method.	43
2.15	Comparison between CFD and analytic drag coefficient $AoA = 0$	45
2.16	Phases of first stage maneuver.	47
2.17	Bi-Linear tangent steering law.	48
2.18	Structure of nodes ID matrix.	50
2.19	Structure of a plate element nodes matrix.	51
2.20	Comparison between SRM scheme and mesh.	52
2.21	Comparison between LRE separated tanks scheme and mesh.	53
2.22	Comparison between LRE common bulkhead tanks scheme and mesh.	53
2.23	Liquid propellant modeling.	54
2.24	Comparison between inter-stage scheme and mesh.	55
2.25	Stringers types.	55
2.26	Comparison between upper composite scheme and mesh.	56
2.27	External forces acting on LV.	57
2.28	Lateral force distribution implementation.	58
2.29	Load cases.	59

2.30	Main outputs residuals charts for RBF surrogate FEM.	61
3.1	Structural optimization flowchart.	64
3.2	Static and buckling analysis after the three optimization cycles.	65
3.3	Objective function and main constraints trend for the three optimization cycles.	66
3.4	Buckling analysis in the five critical load cases at the end of C1.	67
3.5	First bending mode at the end of C1.	67
3.6	Cost function VEGA inspired SO.	70
3.7	Main constraint VEGA inspired SO.	71
3.8	Altitude history VEGA inspired SO.	71
3.9	Relative speed history VEGA inspired SO.	72
3.10	Mission velocity partition VEGA inspired SO.	72
3.11	SRMs maneuvers VEGA inspired SO.	75
3.12	AVUM maneuvers VEGA inspired SO.	75
3.13	Angle of attack VEGA inspired SO.	76
3.14	Aero-thermal heat flux VEGA inspired SO.	76
3.15	Dynamic pressure and $q \cdot AoA$ VEGA inspired SO.	77
3.16	Acceleration VEGA inspired SO.	77
3.17	Ground track VEGA inspired SO.	78
3.18	SRMs thrust and pressure VEGA inspired SO.	79
3.19	Aerodynamic forces distribution at q_{max} ($Mach = 1.89$) VEGA inspired SO.	79
3.20	FEM geometry at q_{max} VEGA inspired SO.	80
3.21	Static stress tensor at q_{max} VEGA inspired SO.	80
3.22	First buckling mode at q_{max} VEGA inspired SO.	80
3.23	Pareto plot VEGA inspired MO.	81
3.24	Altitude history VEGA inspired MO.	82
3.25	Relative speed history VEGA inspired MO.	83
3.26	Mission velocity partition VEGA inspired MO.	83
3.27	SRMs maneuvers VEGA inspired MO.	84
3.28	AVUM maneuvers VEGA inspired MO.	84
3.29	Angle of attack VEGA inspired MO.	85
3.30	Aero-thermal heat flux VEGA inspired MO.	85
3.31	Dynamic pressure and $q \cdot AoA$ VEGA inspired MO.	86
3.32	Acceleration VEGA inspired MO.	86
3.33	Ground track VEGA inspired MO.	87
3.34	SRMs thrust and pressure MO.	88
3.35	Aerodynamic forces distribution at q_{max} ($Mach = 1.89$) VEGA inspired MO.	88
3.36	FEM geometry at q_{max} ($Mach = 1.72$) VEGA inspired MO.	89
3.37	Static stress tensor at q_{max} VEGA inspired MO.	89
3.38	First buckling mode at q_{max} VEGA inspired MO.	89
3.39	Pareto plot TSTO.	93
3.40	Altitude history TSTO.	93
3.41	Relative speed TSTO.	94
3.42	Mission velocity partition TSTO.	94
3.43	LREs maneuver TSTO.	95
3.44	Angle of attack TSTO.	96
3.45	Aero-thermal heat flux TSTO.	96
3.46	Dynamic pressure and $q \cdot AoA$ TSTO.	97
3.47	Acceleration TSTO.	97
3.48	Ground track TSTO.	98
3.49	1 st stage mass flow rate and thrust TSTO.	98
3.50	Aerodynamic forces distribution at q_{max} ($Mach = 1.80$) TSTO.	99

3.51	FEM geometry at q_{max} TSTO.	99
3.52	Static stress tensor at q_{max} TSTO.	100
3.53	First buckling mode at q_{max} TSTO.	100
B.1	Radial basis functions plot.	115
C.1	LV axis from space to time discretization.	119
C.2	Dataset for NN training and validation.	119
C.3	Neural Network scheme.	120
C.4	Neural Network LV aerodynamic results.	121

List of Tables

- 2.1 Objectives. 22
- 2.2 Design variables. 22
- 2.3 Constraints. 23
- 2.4 Average combustion chamber characteristic length. 35
- 2.5 Assumed value for feeding and injection system length. 35
- 2.6 Calculation of C_p based on profile zone for $Mach \leq 3$ 43
- 2.7 Calculation of C_p based on profile zone $Mach > 3$ 43
- 2.8 Materials properties. 50
- 2.9 RBF residuals summary for q_{max} load case. 61
- 2.10 GMB residuals summary for q_{max} load case. 62

- 3.1 Comparison of optimal design variables for the three optimization cycles. 64
- 3.2 Comparison of optimal results of the three optimization cycles. 65
- 3.3 Design variables VEGA inspired SO. 69
- 3.4 Constraints VEGA inspired. 70
- 3.5 Comparison between VEGA LV and VEGA inspired SO configuration. 78
- 3.6 Comparison between VEGA LV and VEGA inspired MO configuration. 87
- 3.7 Design variables TSTO. 91
- 3.8 Constraints of TSTO. 92
- 3.9 Optimal TSTO configuration. 95
- 3.10 MDO computational cost. 100

- B.1 Available RBFs. 115

Nomenclature

χ_{Al}	Percentage of aluminum
χ_{AP}	Percentage of AP
χ_{HTPB}	Percentage of HTPB
Δv	Velocity increment
η_{c^*}	Combustion efficiency
η_{CF}	Thrust efficiency
η_p	Propellant filling coefficient
ρ_p	Propellant density
σ	Static stress
σ_{UTS}	Ultimate tensile strength
θ_{nzl}	Nozzle semiapex angle
ε	Nozzle area ratio
A_w	Combustion chamber wet area
c^*	Characteristic velocity
C_D	Drag coefficient
C_p	Pressure coefficient
D	Drag
D_{cc}	Combustion chamber diameter
D_{cs}	Case diameter
D_e	Nozzle exit diameter
D_t	Throat diameter
H_d	Dome height
I_{sp}	Specific impulse
k_s	Structural coefficient
L_{cs}	Case length
$L_{nzl_{LRE}}$	LRE nozzle length

$L_{nzl_{SRM}}$	SRM nozzle length
L_{sub}	Percentage of nozzle submergence
m	Mass
m_{cs}	Case mass
m_{fuel}	Fuel mass
m_{ign}	Igniter mass
m_{ins}	Insulation mass
m_{nsm}	Non structural mass
$m_{nzl_{sys}_{SRM}}$	SRM nozzle system mass
m_{ox}	Oxidizer mass
m_{pb}	Polar boss mass
m_p	Propellant mass
m_{sk}	Skirt mass
m_s	Structural mass
m_{tank}	Tank mass
MR	Mass ratio
p_c	Chamber pressure
r_b	Burning rate
R_{cs}	Case radius
S_{ref}	Reference surface
SF	Scale Factor
T	Thrust
t_b	Burning time
t_{cs}	Case thickness
V_{cav}	Cavity volume
V_{cs}	Case volume
v_c	Circular orbit velocity
V_{d_l}	Lower dome volume
$V_{d_{up}}$	Upper dome volume
v_e	Effective exhaust velocity

Acronyms

ANNE	Artificial Neural Network Ensemble
AOCS	Attitude and Orbit Control Subsystem
AP	ammonium perchlorate
ASO	Asymmetrical Subspace Optimization
AVUM	Attitude and Vernier Upper Module
BLISS	Bi-Level Integrated System Synthesis
blt	bi-linear tangent steering
CEA	Chemical Equilibrium with Applications
CFD	Computational Fluid Dynamic
CFRP	Carbon Fiber Reinforced Polymer
CNN	Convolutional Neural Network
CO	Collaborative Optimization
DOE	Design of Experiments
EB	Equipment bay
ECEF	Earth-Centered Earth-Fixed
FEA	Finite Element Analysis
FEM	Finite Element Method
FoS	Factor of Safety
GA	Genetic Algorithm
GLOM	Gross Lift-Off Mass
GMB	Gradient Boosting Machine
GNC	Guidance, navigation & control
HTPB	hydroxyl-terminated polybutadiene
IDF	Individual Discipline Feasible

IS Interstage

ISF Incremental Space Filler

LEO Low Earth Orbit

LRE Liquid Rocket Engine

LV Launch Vehicle

MDF MultiDisciplinary Feasible

MDO Multidisciplinary Design Optimization

MEOP Maximum Expected Operative Pressure

NARX Nonlinear Autoregressive Exogenous Model

PLA Payload adapter

PSO Particle Swarm Optimization

RBF Radial Basis Function

RNN Recurrent Neural Network

ROM Reduced Order Model

RR Retro-Rockets

RSMs Response surface methods

SRM Solid Rocket Motor

SSTO Single Stage to Orbit

TSTO Two Stage To Orbit

TVC Thrust Vector Control

ULH Uniform Latin Hypercube

VEGA Vettore Europeo Generazione Avanzata

Summary of the thesis

Research motivation

A Launch Vehicle (LV) is a rocket-propelled vehicle able to transport a payload outside the Earth's atmosphere, whose boundary is the so-called Karman line set to 100 km . Launch vehicles are complex systems because of the multiple top-level requirements they must fulfill to reach outer space. The greatest engineering challenge lies in overcoming the energy required to reach orbit. To achieve this, they must contain a large amount of propellant and power within a structure that is as light as possible. Furthermore, in the early days of the space race, the financial allocation to develop and produce a launch vehicle posed no concerns; nevertheless, in the present era, reducing time and cost is crucial to remain competitive in the marketplace. Indeed, nowadays, due to the huge competition in the space transportation sector, reduction of development time is a central key as concerns the design of new launch vehicles. Every mission lifetime cycle is composed by 7 phases: from phase 0 (mission analysis) to phase F (disposal). At the end of phase A (feasibility), the 80 % of the entire life cost is already determined (see Ref. [1]). Therefore, it is crucial to use a correct approach to evaluate all the possible design choices. By definition the design of a launch vehicle is multidisciplinary, because it results as a trade-off between Propulsion, Structures, Aerodynamics, Flight mechanics and Guidance, navigation & control (GNC). As a practical example, the requirement of a different nozzle expansion ratio of an upper stage implies a variation of the interstage length, and in turn, a consequent modification of the mass and the launch vehicle profile, impacting on aerodynamic and trajectory. Another relevant example is the determination of the thrust shape of a first stage Solid Rocket Motor (SRM). Fig. 1 represents the correct thrust vs time trend that a first stage SRM must have to correctly flight inside the atmosphere, as it has been investigated in Refs. [2] and [3]. Since the SRM thrust is designed a priori according to the propellant grain shape, the thrust history is subjected to many constraints related to the mission to be accomplished by the LV. During the first stage flight, five phases can be distinguished:

- I The first phase coincides with lift-off. The initial thrust level is determined by the minimum thrust-weight ratio, in fact to quickly overcome the first layers of the atmosphere, the duration of the vertical ascent must be as short as possible. In addition, the maximum thrust must be such that divided by the nozzle throat area, the resulting pressure must not exceed the Maximum Expected Operative Pressure (MEOP). This upper limit sometimes also features the imposition of a maximum acceleration value to limit aerodynamic losses.
- II During the second phase, the thrust must decrease in order to maintain the dynamic pressure and its product with the angle of attack under a determinate threshold. However, the thrust

level must not decrease too much, otherwise there is a performance drop due to the increment of drag losses.

- III In the third phase the thrust can slightly increase due to the overcoming of the time instant of the maximum dynamic pressure. This phase ends when the maximum acceleration induced to payload is reached.
- IV During phase four the thrust must decrease again. Indeed the thrust level must balance the loss of propellant mass to keep the acceleration under its threshold.
- V The last phase is the tail-off, which corresponds to the sharp drop-off of the pressure due to the depletion of the combustion surface. This phase presents two bounds. The lower bound is given by the dynamic pressure at stage separation which must be below its upper limit. This constraint can be satisfied or having a minimum burning time or increasing the pitch angle (this last solution can have a huge impact on the entire mission due to the strong augment of gravity losses). The upper limit of the tail-off phase is given by the maximum burning time that the nozzle throat can afford (more the burning time, more the throat erosion).

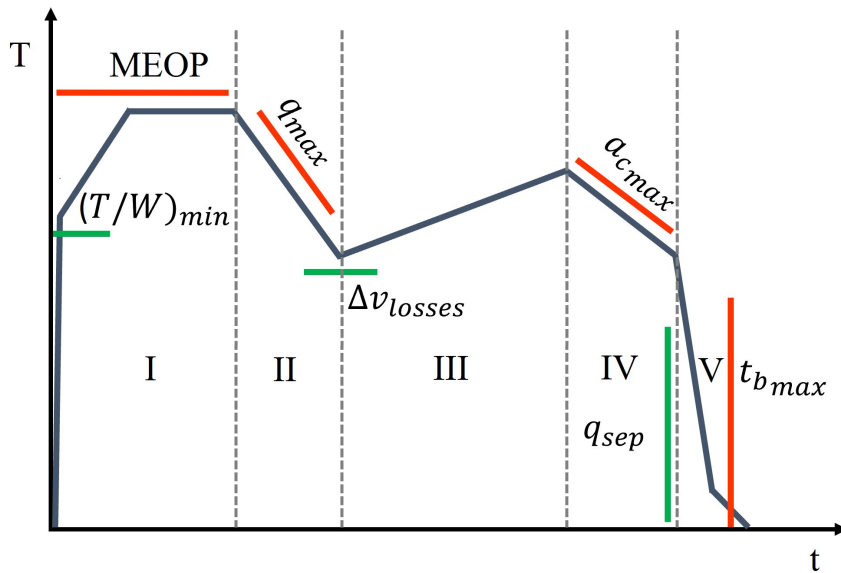


Figure 1: First stage SRM thrust shape.

The conventional method of designing launch vehicles involves a cyclical sequence of steps performed with high fidelity tools by experts in the respective disciplines involved in the process. The main issue with this approach is that these experts optimize the LV to fulfill the requirements and constraints of their specific discipline (leaving fixed other design variables), potentially leading to a sub-optimal LV configuration. Moreover, several cycles are necessary to reach a design that meets the overall mission requirements, with a consequent increase of design time. The limitations of this conventional approach are surpassed by adopting Multidisciplinary Design Optimization (MDO), which is a technique that optimizes engineering systems by considering the mutual interaction between all the involved disciplines, taking into account the simultaneous variation of all design variables. Moreover, MDO necessitates a significant number of iterations, which, nonetheless, demands a considerably reduced computational time with respect to the classical approach (on the

scale of hours to days). Many MDO's researches have been carried out on Launch Vehicles and missions (see Refs. [4], [5], [6], [7], [8] and [9]), however, inside an optimization loop, the structural analysis performed by a Finite Element Method (FEM) solver and aerodynamic investigation using Computational Fluid Dynamics (CFD) are still not common due to the huge computational time, so the analytical models are preferred with a consequent increase of approximation.

This thesis is framed within a research activity commissioned by the European Space Agency (ESA) about launch vehicle MDO in order to study and design new European LV configuration taking advantage of the emerging machine learning techniques. Indeed, the real novelty of this work is the adoption of a high fidelity model to perform Finite Element Analysis (FEA) and the creation of its surrogate. In addition, a Reduced Order Model (ROM) has been created for aerodynamics and the foundation has been laid for the development of a surrogate model of the Computational Fluid Dynamic (CFD).

In fact, the main objective of this thesis is to present a methodology to perform launch vehicle multidisciplinary design optimization combining good accuracy with high computational speed. Regarding the LV structure, this goal can therefore be addressed by using a FEM solver in conjunction with a surrogate model that utilizes Response surface methods (RSMs), which have been extensively employed in many scientific fields in recent years, including aircraft design (see Ref. [10]) and launch vehicle design (see Ref. [11]) balancing accuracy and speed. Two RSMs have been exploited: Radial Basis Function (RBF) and Gradient Boosting Machine (GBM). RBF are a powerful tool that interpolates the data in an irregular grid with proper known functions. GBM is a machine learning method which utilizes decision trees coupled with gradient optimization to minimize the residuals between observed and predicted output refining progressively the surrogate model. It has been observed that when the number of design variables is high, GBM is preferred with respect to RBF. Instead, regarding the LV aerodynamic the CFD is replaced by a reduced order model (ROM) based on panels method. As concerns the optimization algorithms, the Genetic Algorithm (GA), originally developed by Holland in Ref. [12] and Goldberg in Ref. [13] can widely explore the space of solutions. Indeed, the research of the optimum does not start from a single point, but from an initial population called Design of Experiments (DOE), which is created through different sampling techniques, such as the Uniform Latin hypercube (ULH) scheme (see Ref. [14]). Then, this population is updated at each generation by using the genetic operators of crossover, mutation and selection. However, also the gradient based methods, such the ones described in Refs. [15] and [16] can be helpful to increase the solution accuracy found by the GA.

Multi-disciplinary design optimization of launch vehicle: a literature review

Optimization from a mathematical point of view originated in 1788 (see Ref. [17]) with Lagrange who, thanks to his multipliers, was able to find the maximum of constrained functions. The first application of optimization came at the end of 1910s with Goddard who formulated the problem of rocket ascent in Ref. [18], which consisted to reach a given altitude with the minimum fuel consumption, by applying an optimal thrust control. Then, in the 1920s Oberth gave an approximated solution of this problem in Ref. [19]. In the same decade Hohmann in Ref. [20] proposed an orbital maneuver, called Hohmann transfer orbit, through which a spacecraft is transferred between two

different orbits around the same body using the minimum amount of propellant. Between 1940s and 1950s the optimization has been applied to solve the optimal staging problem: Malina in Ref. [21] studied the effect of the number of stages on the velocity of a rocket; Vertregt in Ref. [22] proposed an uniform system of notation for multistage rockets and Goldsmith (see Ref. [23]) and Hall (see Ref. [24]) gave a solution for optimal staging respectively for a 2 and 3 stages rockets. Another relevant application of optimization in engineering came in the 1960s with Schmit (see Ref. [25]), who applied it in the field of structural design by minimizing the weight of a structure respecting the constraints on maximum allowable stress. Further improvements were achieved in the 1970s by Berke in Ref. [26] and Khot in Ref. [27] who studied the structural optimization of aerospace vehicles considering a large number of design variables. Although the first coupling between disciplines occurred with the emergence of aeroelasticity in the 1930s (see Ref. [28]), aerodynamics and structures were only integrated with each other at equation level. The integration at discipline level occurred in the 1980s with Sobieszczanski-Sobieski who developed the linear decomposition technique in Refs. [29] and [30]; the same author studied also the interaction of the disciplines which can be hierarchic or non-hierarchic in Ref. [31]. In the 1990s more MDO architectures for aerospace application were exploited, two in particular were the most important: the Collaborative Optimization (CO) technique, which decomposes a complex system into subsystems that are optimized in parallel was implemented in Ref. [32] by Braun and the Bi-Level Integrated System Synthesis (BLISS) architecture which was developed in Ref. [33] in order to handle problem with a huge number of design variables. In the 2000s, the advancement of computational resources conveyed MDO research from theory to practical applications: in fact in that years, MDO was adopted to design vehicles (Refs. [34] and [35]), satellites (Ref. [36]), spacecrafts (Ref. [37]), ships (Ref. [38]) and turbine blades (Ref. [39]). In these years the response surface methods (RSMs) started to be investigated for MDO engineering application, like in Ref. [40] where the kriging models have been applied to the MDO of an aerospike nozzle.

As concerns the design of launch vehicle, the application of MDO started in the 1990s with Braun, who applied his CO technique to study different LV configurations. In Ref. [41], the author compared two methods: the first one is a sequential approach, where each discipline is optimized separately and then integrated into a system-level solution; the second method is the concurrent approach, where all disciplines are optimized simultaneously using a collaborative optimization framework. The same author showed the applicability of the concurrent approach in Ref. [42], where a Two Stage To Orbit (TSTO) reusable launch vehicle has been optimized demonstrating the efficiency of the CO method. While in Ref. [43], the same method has been applied to the design of the Delta Clipper-Experimental Advanced (DC-XA), which was a single-stage-to-orbit rocket prototype built by McDonnell Douglas, and the X-33, that was a reusable launch vehicle demonstrator developed by NASA and Lockheed Martin. In the 2000s and in the 2010s, the additional computing power available made it possible to apply MDO for more complex problems considering more disciplines involved in launch vehicle design. In Ref. [44], four optimization techniques (fixed-point iteration, partial and full optimization based decomposition and CO) have been compared to simultaneously optimize the ascent, orbital and re-entry branches of trajectory of the Kistler K-1 launch vehicle, which originally were treated as three separated sequential optimization sub-problems. Another kind of trajectory optimization inside an MDO loop has been carried out in Ref. [45] where a three stages LV has been optimized considering the coupling between trajectory

and engine throttling; moreover in the same work a support vector regression has been exploited to create meta-models of the involved disciplines. In Ref. [46] the GA was applied to minimize the mass and the cost of a three and four stages SRMs based LV, taking in consideration the interaction of trajectory, propulsion, aerodynamic and mass properties. In Ref. [47] the MDO of a small satellite launch vehicle was performed using Particle Swarm Optimization (PSO) algorithm, while in Ref. [48] there is a comparison between the MDO of an air versus ground launch vehicle using PSO and GA algorithms. Instead in Ref. [49] the Sequential quadratic programming (SQP) algorithm and the Latin hypercube scheme are adopted to perform a reliability-based MDO of a TSTO expendable LV considering also the uncertainty on the design variables. In Ref. [50] single- and multi-objective MDO of expendable launch vehicles have been performed by comparing PSO, Non-Dominated Sorting Genetic Algorithm (NSGAI) and WORHP (acronym of "We Optimize Really Huge Problems"). The latter is a software mathematical library, developed by the University of Bremen to solve nonlinear programming problems that have a large number of design variables and constraints. WORHP has been adopted as optimizer by ESA ESTEC during the ESA PRES-TIGE program within which the work of Ref. [5] stands as a milestone for the development of MDO applied on European launch vehicles Vettore Europeo Generazione Avanzata (VEGA) and Ariane 5. Another optimization on a VEGA launch vehicle configuration has been performed in Ref. [7] considering just the coupling between trajectory and thrust profile shape. In Ref.[51] the effect of the uncertainties on the launch vehicle design MDO has been studied to improve the robustness of the solutions. The same author studied also a partially re-usable launch vehicle configuration using surrogate model applied to MDO (see Ref. [52]). For additional details on some of the cited papers mentioned in this paragraph, the reader is invited to consult the work of Ref. [6], which is a survey of launch vehicle MDO applications up to the 2010s. Regarding the MDO architectures, the most used in LV design optimization is the Multidisciplinary Design Feasible (MDF), that is described in Sec. 1.4; however in Ref. [53] a new approach called stage wise decomposition was explored: it consists in dividing the problem considering the single stage design instead of the disciplines. Thus there is a global optimizer which manages the design of each stage independently.

Methodology, objectives and activities description

In the field of launch vehicle design, taking into account the growing demand for launch services and leveraging the increase in computational resources, the objectives of this thesis are the following:

- understanding the complex interaction between disciplines in the field of launch vehicle system engineering;
- creation of a tool to perform launch vehicle MDO exploiting the adoption of high fidelity models and their surrogates;
- practical use of the tool to reduce the time and therefore the cost of development of new launch vehicles.

Thus, the thesis is focused on two main aspects: launch vehicle design and optimization. The first aspect implies the implementation of the suitable engineering model for every discipline involved; the second aspect involves the integration of these disciplines inside a proper MDO architecture. In order to achieve these goals, the activities carried out are:

-
- bibliography research on launch vehicle design and MDO;
 - implementation and validation of a mathematical, physical and numerical model for each discipline in terms of input-output *black box*. In particular, within a Matlab© environment, a model has been created for: calculation of the **energy** to reach the orbit in terms of Δv , characterization of the **propulsion** system with regard to thrust and specific impulse, determination of vehicle **geometry** sizing and **mass** budget, **aerodynamic** coefficients calculation, LV **trajectory** evaluation from lift-off to orbit insertion, considering also empty stages fallout points and FEM **structural** analysis.¹
 - creation of FE surrogate model in order to increase the computational speed. Indeed the time of a structural analysis with NASTRAN©, described in Ref. [54], (which is the standard FEA solver in aerospace applications) is of the order of minutes, thus, for a complete MDO loop consisting of tens of thousands of iterations, this involves a substantial computational time.
 - building of the optimization workflow by integrating the *black boxes* linked between each others. Specifically the chosen architecture between the ones categorized in Ref. [55] is the Asymmetrical Subspace Optimization (ASO). An internal optimization loop is performed with Lagrangian's multipliers on propulsion, geometry and mass budget to find the optimal staging and an external optimization loop is carried out connecting all the other disciplines (aerodynamic, trajectory and structures).
 - choice of design variables together with their range bounded by the lower and upper limits, acting a trade-off between speed and exploration of the space of solution and considering the physical and manufacturing feasibility
 - testing of different optimization algorithms, such as the modeFRONTIER© built in GA MOGA-II and *NSGA-II*, gradient based and hybrid.
 - performing single- and multi- objectives disciplinary design optimization of a solid rocket motor and a liquid rocket engine based launch vehicle. Results were discussed from engineering, mathematical and computational perspectives, highlighting the usefulness of the combined adoption of high-fidelity models and their surrogates.

Thesis outline

This Ph.D. thesis is divided into three chapters. The first is devoted to MDO theory, the second to launch vehicle design and the third one to the results. In addition, there are three supporting appendices.

In Chapter 1 is described the theoretical background of Multidisciplinary Design Optimization focusing on the mathematical aspects. It is defined the difference between single and multi-objective

¹The Guidance, Navigation, and Control (GNC) discipline's *black box* was not developed within the scope of this thesis, as the Launch Vehicle (LV) design is executed and optimized during phase A of design. The incorporation of a GNC *black box* is recommended for subsequent design phases, as elaborated in the future remarks section. Nevertheless, the imposed design constraints consider the capability of the Thrust Vector Control (TVC) to control the LV maintaining a static controllability margin at the maximum $q \cdot \alpha$ of 1.5 as explained in Chpt. 3.

MDO, the principal algorithms to create a Design of Experiments are compared, the main architecture are displayed and the principal optimization algorithms adopted in the thesis are discussed.

In Chapter 2, there is a complete descriptions of all the engineering models necessary to design a launch vehicle and its mission. In particular, the models of orbital energy, propulsion, geometry, mass estimation, aerodynamic and structure are described.

In Chapter 3 the results of the optimization are discussed: firstly a structural optimization of a VEGA inspired LV to validate the structural model generator, then a single and multi-objective MDO of another VEGA inspired LV to validate the MDO architecture and finally a multi-objective MDO of an LRE based launch vehicle. Furthermore, comprehensive details are available concerning the computation time of optimization cycles.

In Appendix A the Lagrangian optimizer for LV staging is described.

In Appendix B there is a theoretical overview of the machine learning techniques used for the surrogate FEM: radial basis function and gradient boosting machine.

In Appendix C the neural network model for LV aerodynamic is discussed.

Chapter 1

Multi-disciplinary Design Optimization theoretical issues

Multidisciplinary Design Optimization (MDO) is a powerful and comprehensive approach that has gained significant attention in engineering and design fields. As systems become increasingly complex, with multiple interacting disciplines involved, the need for an integrated approach to optimize design solutions becomes imperative. In the aerospace field, MDO aims to bridge the gaps between different disciplines, such as Propulsion, Structures, Aerodynamics, Flight Mechanics, and GNC, by considering their inter-dependencies and interactions.

In this chapter a general overview of MDO will be given with a particular focus on the mathematical aspects.

1.1 Multi-disciplinary Design Optimization

At its core, MDO seeks to find the best design solution that meets one or multiple objectives respecting constraints. This can include improving performance metrics, such as maximizing efficiency or minimizing weight, while simultaneously satisfying various design constraints, such as stress limits or manufacturing feasibility. By considering these factors simultaneously, MDO provides a holistic and optimized approach to engineering design. As explained in the introduction, the state of the art in MDO involves the development of advanced algorithms, optimization techniques, and computational tools. These tools enable efficient handling of the complex interactions among different disciplines, leveraging mathematical models and simulation techniques. For instance, surrogate modeling techniques, such as response surface modeling, can be employed to approximate the behavior of the system and reduce the computational time of the optimization process.

In recent years, the advancement of high-performance computing and parallel processing has significantly contributed to the evolution of MDO. These computational tools allow for the analysis and optimization of large-scale, computationally intensive problems within reasonable time frames. As a result, engineers can explore more complex design spaces and make informed decisions based on comprehensive optimization results. The field continues to evolve and adapt to the ever-changing demands of complex engineering systems, offering immense potential for improving design outcomes and driving innovation across various industries.

1.2 Single vs Multi Objective Optimization

The objectives of an optimization problem can be one or more. In presence of just one objective, the optimal design inside the space of solution is only one. Mathematically, the problem consists to find the minimum of the cost function $J(x)$, where x is the vector of the design variables.

$$\begin{aligned}
 & \text{minimize :} && J(x) \\
 & \text{inequality constraints :} && g_k(x) \leq 0 \text{ for } k = 1, \dots, n_1 \\
 & \text{equality constraints :} && h_j(x) = 0 \text{ for } j = 1, \dots, n_2 \\
 & \text{lower \& upper bounds :} && x_{i_{LB}} \leq x_i \leq x_{i_{UP}} \text{ for } j = 1, \dots, n
 \end{aligned} \tag{1.1}$$

In case of constrained problem, $J(x)$ is subjected to inequality $g(x)$ and equality $h(x)$ constraints. Moreover, every design variable x must relies in an appropriate range which is delimited by lower x_{LB} and upper x_{UB} bounds. The choice of these side constraints is the result of a trade off, indeed, if the ranges are too large, the computational cost increases, while if the range is too short, the space of solution decreases and the found solution is probably a local optimum. In Fig. 1.1 is displayed

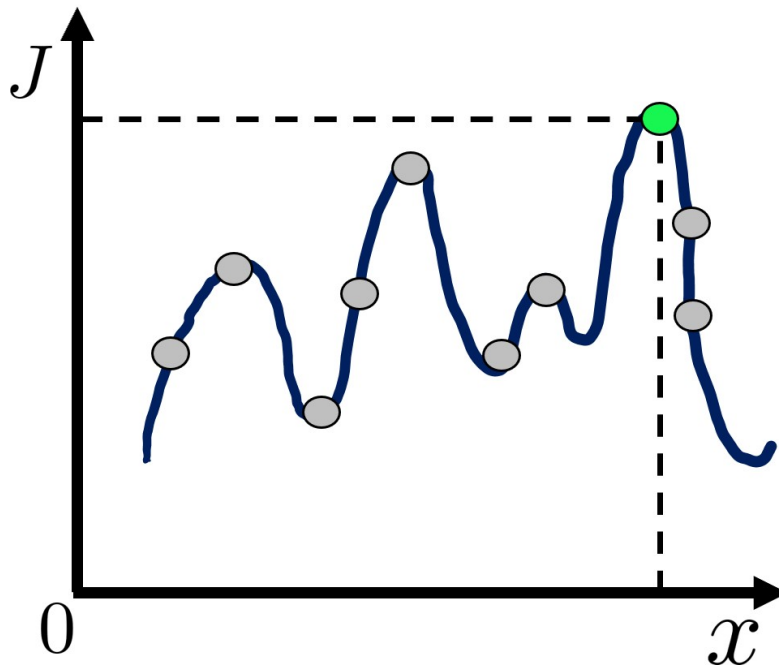


Figure 1.1: Single objective.

an example of a one dimensional unconstrained objective function J . This function exhibits several maximum and minimum points as x varies. Every circle signifies an iteration during which J is assessed, with the light green circle denoting the global maximum.

Instead, when there are multiple objectives, the mathematical formulation changes, because must be minimized the vector composed by m cost functions $\iota(x)$.

$$\begin{aligned}
 \text{minimize : } & \iota(x) = [J_1(x), \dots, J_m(x)] \\
 \text{inequality constraints : } & g_k(x) \leq 0 \quad \text{for } k = 1, \dots, n_1 \\
 \text{equality constraints : } & h_j(x) = 0 \quad \text{for } j = 1, \dots, n_2 \\
 \text{lower \& upper bounds : } & x_{i_{LB}} \leq x_i \leq x_{i_{UP}} \quad \text{for } j = 1, \dots, n
 \end{aligned} \tag{1.2}$$

In order to satisfy the minimization of all the cost functions, the optimal design is no more unique. For instance, with 2 objectives, the best solutions are placed on a $1D$ curve called Pareto front (see Ref. [56]), while with 3 objectives the best designs are part of $2D$ surface. Thus the Pareto frontier has a dimension of $n - 1$. In Fig. 1.2 is displayed an example with 2 objective functions J_1 and J_2 . These functions are inversely proportional, meaning that as one increases, the other decreases. Each circle signifies an iteration in which the two functions are evaluated. The green circles, positioned closest to the origin of the axes, depict the Pareto front. The three light green circles represent: the solution with the minimum of J_1 , the one with the minimum of J_2 , and the solution demonstrating the best trade-off between the two cost functions, which is the one closest to the origin of the axes.

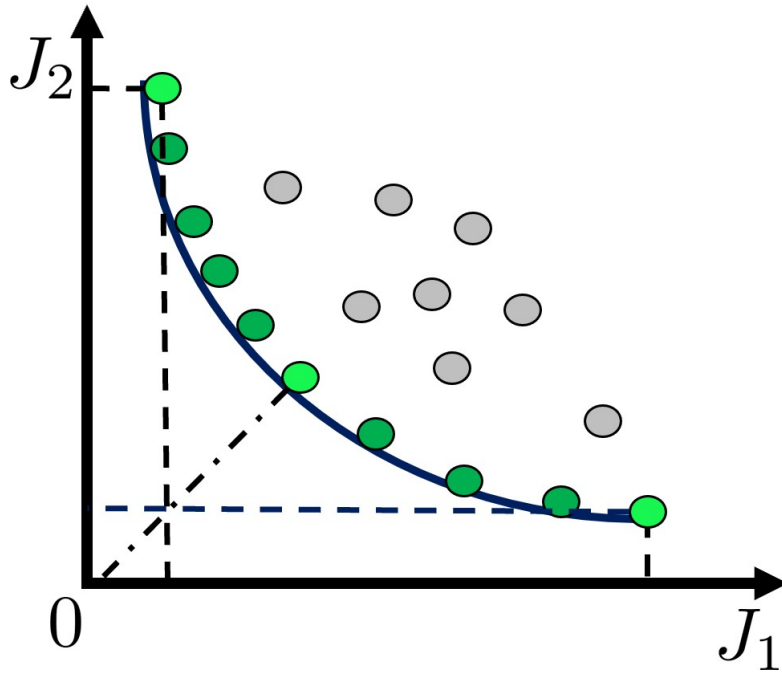


Figure 1.2: Multi objective.

In both the single and multi-objective cases, the design variables can be continuous or discrete. The last ones can be classified in ordered or unordered. An example of discrete ordered design variable is the number of reinforcements that can assume only a natural number. Instead, an example of discrete unordered is the kind of reinforcements, that is still a natural number associated to a particular shape (for instance: 1 for circular, 2 for rectangular).

1.3 Design of Experiments

In order to start a stochastic method is necessary to create an initial population composed by a set of design variables called DOE. Inside a DOE, every design variable changes following a precise scheme. The goal is to cover the design space to correctly explore the space of solution. In fact, the DOE technique was invented by R. Fisher in Ref. [57] as a method to maximize the knowledge of a system using a minimum number of experiments. In MDO the most used DOE algorithm are: random, Uniform Latin Hypercube (ULH), Sobol, Incremental Space Filler (ISF), full factorial and orthogonal.

The random scheme is based on the mathematical theory of random number generation which relies on methods like the one described in Ref. [58]. The drawback of this scheme is that randomness can cause clustering of samples.

A way to solve this issue is the implementation of the Sobol scheme (see Ref. [59]), which creates a quasi-random distribution of samples that are maximally spaced between each other. The issue of the Sobol consists in the tendency of creating cluster of samples in the diagonal direction.

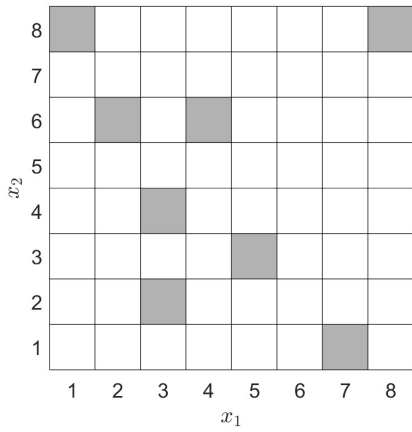
ISF is an algorithm which adds new points starting by the middle of each design variable. Every points is added by maximizing the minimum distance between the previous ones. A methodology to create an ISF DOE is the Greedy algorithm, which use a simple distance based metric to maximize the distance between points (see Ref. [60]).

ULH, described in Ref. [14], is an advanced Monte Carlo sampling. Each design variable range is split in n intervals and in every of them is selected a random value. In this way the design space is uniformly covered, even with few points.

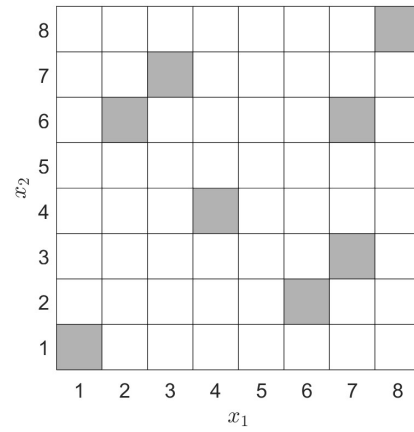
Another DOE algorithm is the full factorial one (see Ref. [61]), which divides every design variable ranges in levels and then perform all the possible factor combinations. It is very time consuming and it is not suitable the number of levels is low.

A variation of the full factorial is the orthogonal DOE developed in Ref. [62]. With this method the design variables are divided into orthogonal arrays.

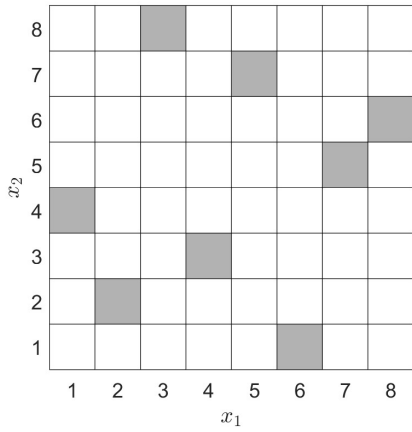
The difference between the different DOE algorithms is shown in Fig. 1.3. A design space with 64 points has been created, comprising 2 variables: x_1 and x_2 . Then 8 samples have been chosen according to the different DOE algorithms. It can be noticed that the best scheme which better covers the design space is the ULH (see Fig. 1.3(c)).



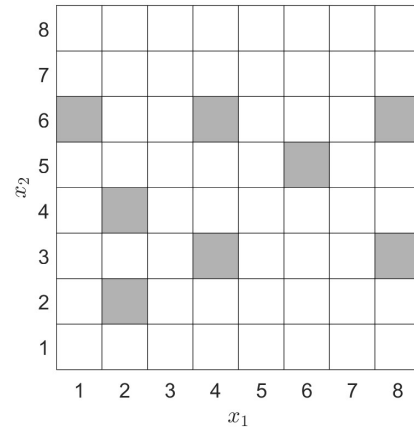
(a) Random scheme



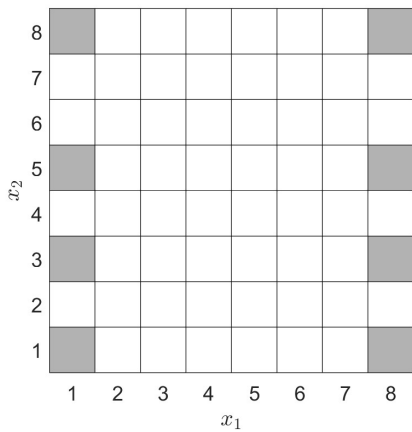
(b) Sobol scheme



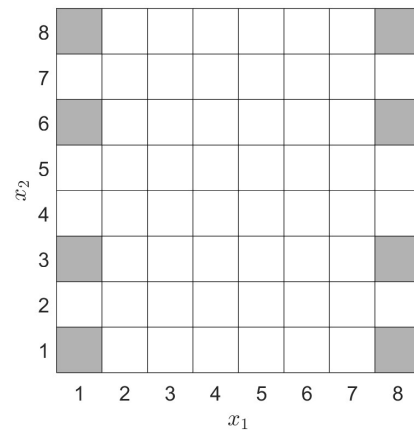
(c) ULH scheme



(d) ISF scheme



(e) Full factorial scheme



(f) Taguchi orthogonal scheme

Figure 1.3: Comparison between different DOE schemes.

1.4 Architectures

There are multiple ways to solve the same optimization problem. For instance, it is possible to have different inter-connections or between the disciplines or a diverse logic flow order. In Ref. [55] a survey of multidisciplinary design optimization architecture is cataloged and described in detail. The main architectures found in literature are displayed in the Figures below.

Figure 1.4 shows the Individual Discipline Feasible (IDF) architecture, according to which the involved disciplines are independent and do not exchange information with each other. However it is necessary to include consistency constraints to assure the connection between the disciplines.

In Figure 1.5 is displayed the MultiDisciplinary Feasible (MDF), according to which all the disciplines are coupled between each other, exchanging input/output.

Another kind of architecture is the CO, which is shown in Fig. 1.6. In this kind of architecture each discipline is optimized separately by a dedicated sub-optimizer, besides all the process is still managed by an external optimizer.

The architecture chosen for this thesis is the ASO, described in Fig. 1.7. Primarily, it is an MDF approach. However, the interconnected disciplines are overseen by a sub-optimizer, and the feedback loop between disciplines external to the internal optimizer is eliminated to enhance computational speed.

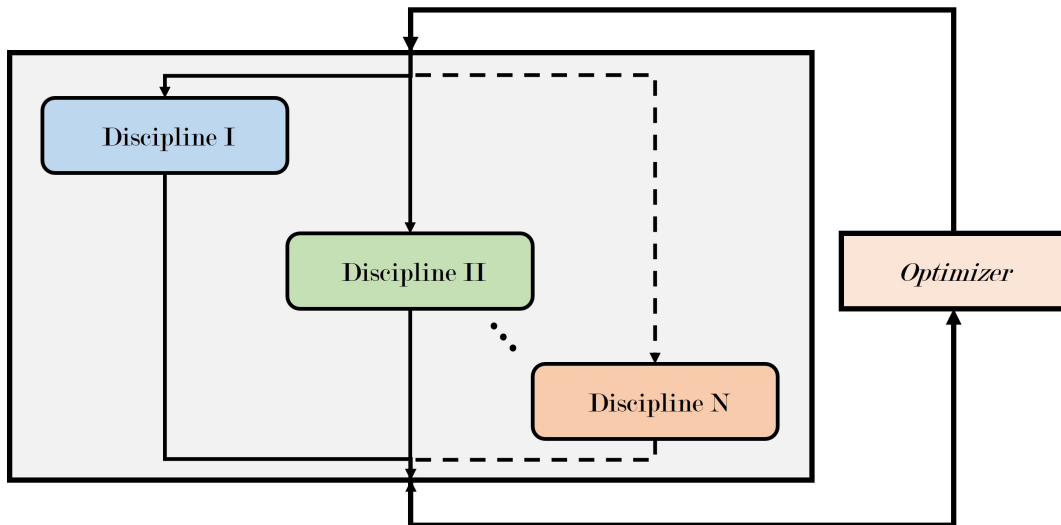


Figure 1.4: IDF architecture.

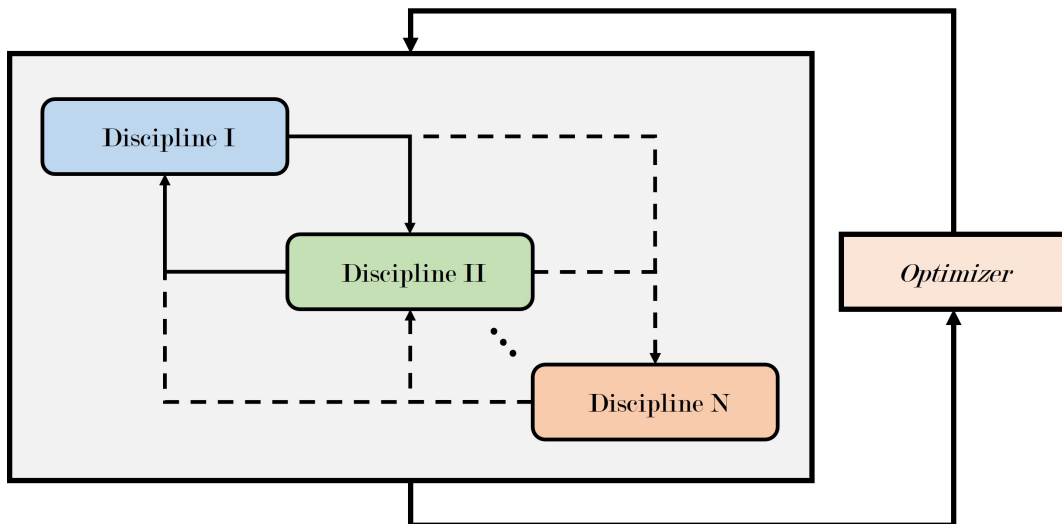


Figure 1.5: MDF architecture.

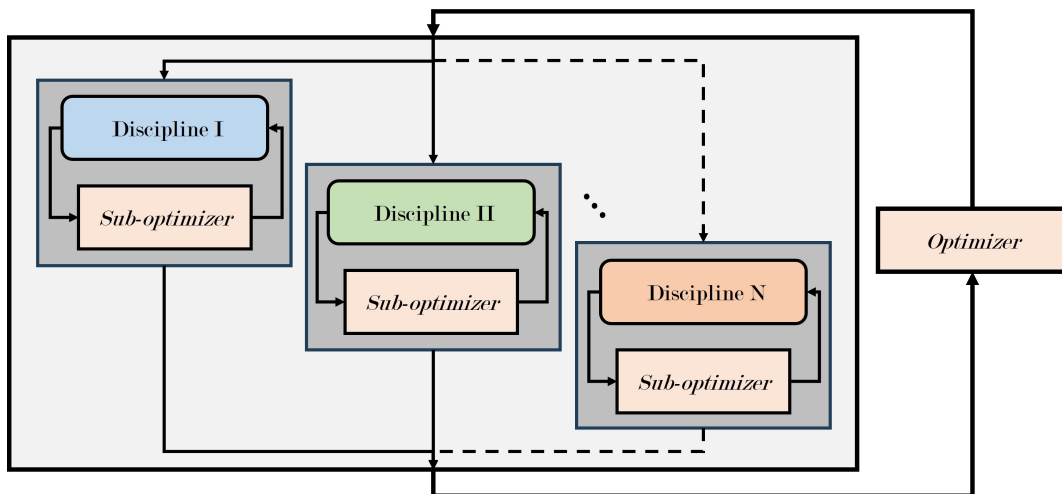


Figure 1.6: CO architecture.

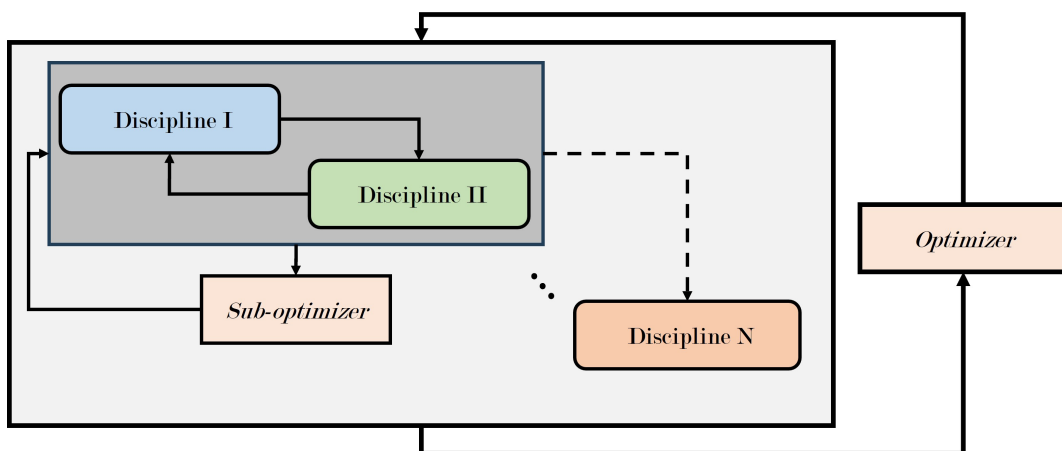


Figure 1.7: ASO architecture.

1.5 Methods

There are numerous methods to solve optimization problems, as indicated in Refs. [63] and [64]. The choice of the method depends by the problem formulation, in fact, there is not a single method which is valid for every MDO formulation. The methods can be divided in two categories: deterministic and stochastic. Deterministic methods are based on the evaluation of the gradient of the cost function, thus they can be used only for problems in which the derivatives of the objective functions can be defined. Besides, their efficiency is determined by the smoothness of the functions. The drawback of gradient-based method is that they can remain stuck in local optimum. On the other hand, stochastic methods does not evaluate gradient but rely on a random process to find the optimum. These methods include evolutionary algorithms, genetic algorithm, particle swarm optimization and game theory based.

1.5.1 Genetic Algorithm

Genetic algorithms (GA) are classical examples of evolutionary algorithms in which a population of individuals evolves based on the logic of natural selection. In fact, the GA works with the same principles of the Darwin's theory of evolution, which is explained in the 1859 book *"On the Origin of Species by Means of Natural Selection, or Preservation of Favoured Races in the Struggle for Life."* As Darwin suggested, small hereditary variations can accumulate if they induce an increase in fitness, or the ability to reproduce. It should also be noted that the cumulative selection of "most suitable" genes over time has resulted in the development of new species (see Ref. [65]). The algorithm, originally developed by Holland in Ref. [12] and Goldberg in Ref. [13], utilizes the genetic operators of cross-over, selection and mutation. Indeed, every design variable is seen as a gene and a vector of design variables is like a chromosome (or individual). A group of individuals represents a population, which changes at each generation through the genetic operators. The flowchart of a typical genetic algorithm is displayed in Fig. 1.8. Once generated the initial population, for each individual it is calculated the cost function and the constraints i.e. the fitness value. The individuals that present the best fitness values are selected and they exchange their genetic material (design variables) between each other through the crossover mechanism to produce a percentage of individuals of the next generation. In order to assure the genetic diversity, another percentage of the next generation is created with the mutation operator which changes one or more genes inside the chromosomes. This mechanism avoids that the algorithm remains stuck in local optima. An example of applications of the genetics operators is displayed in Fig. 1.9: two vectors composed by 8 genes which can assume either values 0 or 1 are selected; then two new individuals are generated by crossover and other two by mutation. The algorithm utilized in this thesis is the built in *MOGA-II* (Multi-Objective Genetic Algorithm) of ESTECO© modeFRONTIER, described in Ref. [66]. This algorithm, which has been used for various MDO problem in aerospace like the ones in Refs. [67] and [68], presents four variants that differ based on diverse workflow management and different crossover and mutation rates. In particular, the probability of classical crossover $P_{C_{co}}$ depends on the probabilities of directional crossover $P_{D_{co}}$, selection P_S and mutation P_M (see Eq. (1.3)). Classical crossover means that two individuals of the population exchange their genes in order to create a new design for the next generation. Instead, directional crossover implies that the direction of improvement can be detected among the individuals of the same generation, comparing the fitness

of three random individuals and moving the genes of the new individual in a weighted direction between the three. Selection consists in copying the individuals with the best fitness directly in the next generation. Mutation implies that some genes of an individual are randomly modified. A high probability of classical crossover allows the algorithm to span the design space more efficiently, resulting in a more robust, but slower algorithm.

$$P_{C_{co}} = 1 - (P_{D_{co}} + P_S + P_M) \quad (1.3)$$

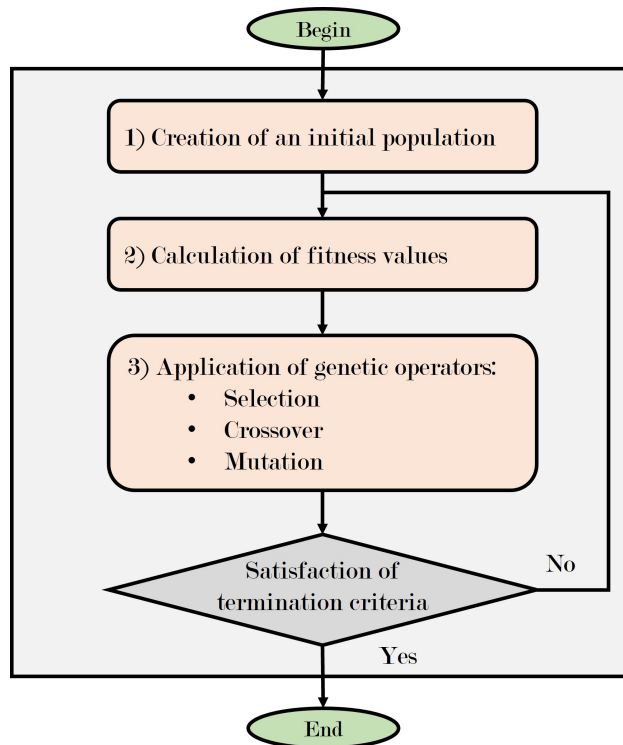


Figure 1.8: GA flowchart.

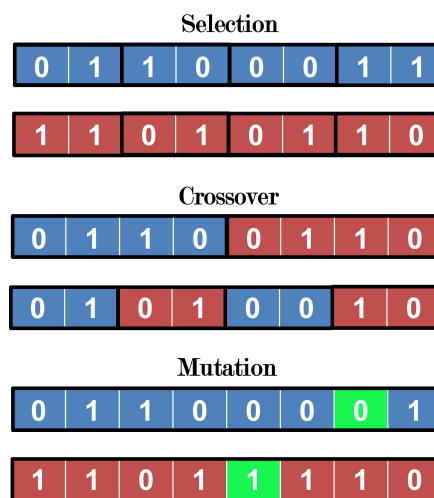


Figure 1.9: Genetic operators.

1.5.2 Gradient based algorithm

The gradient based algorithm finds the minimum of a function starting by a point inside the domain and moving in the opposite direction of the gradient. This idea is attributed to Cauchy as described in Ref [69]. The application of this algorithm to non-linear optimization problems was studied by Curry (see Ref [70]). Considering a continuous and differentiable multi-variable function $F(x)$, starting by a first guess point x_n , the next point x_{n+1} is obtained by subtracting the product between the gradient of the function $\nabla F(x_n)$ and the step size γ_n .

$$x_{n+1} = x_n - \gamma_n \nabla F(x_n) \quad (1.4)$$

The choice of the step size is the result of a trade-off between accuracy and computational time. A small step size implies a higher number of iterations to reach the minimum, while a high step size can lead to divergence and overshoot. In Fig. 1.10 is displayed an example of application of the gradient based algorithm. The function $F(x_1, x_2) = x_1^2 + x_2^2$ is continuous and derivable in the interval $[-1, +1]$, thus the algorithm can be applied. Starting from the point $(-1, -1)$, where the function equals 2, the minimum point $(0, 0)$ is reached, where the function equals 0.

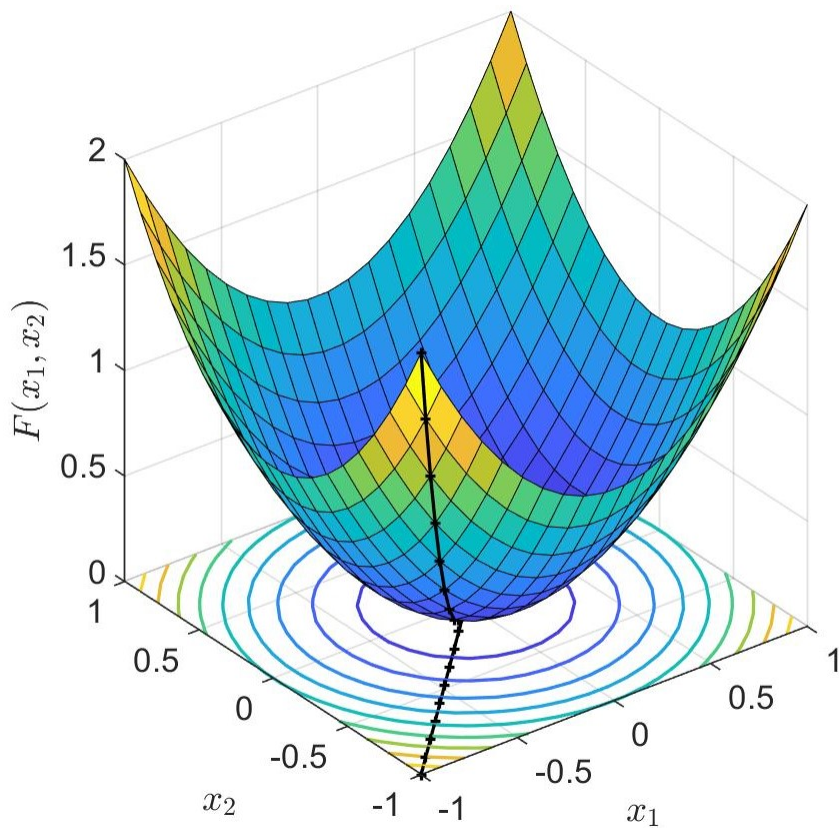


Figure 1.10: Example of gradient based algorithm.

Chapter 2

Launch Vehicle Design

This chapter presents the design process logic and the engineering models related to each discipline necessary to carry out the MDO of Launch Vehicle. These disciplines are described in the next sections, following the same logical order with which they interact in the code, thus: propulsion, mass budget, aerodynamic, trajectory and structure.

2.1 Design Process

As it can be seen in Fig. 2.1, every launch vehicle is composed by three kind of masses: propellant mass m_p , structural mass m_s and payload mass m_u .

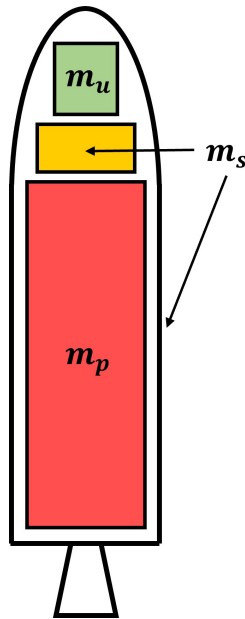


Figure 2.1: LV scheme.

The efficiency of an LV is measured by the payload ratio, that is the ratio between the payload mass and the initial one at lift-off m_0 .

$$\lambda_u = \frac{m_u}{m_0} \quad (2.1)$$

Therefore for the same payload mass, the most efficient LV is the one with the lowest sum of propellant and structural mass. Indeed, Eq. (2.1) can be written in function of the structural mass,

considering that $m_u = m_f - m_s$. So similarly, it can be said that for the same initial mass, the most efficient LV is the one with the lowest structural mass. The governing equation to design a launch vehicle is the Tsiolkovsky's rocket equation published in 1903 (see Ref. [71]).

$$\Delta v = v_e \ln \frac{m_0}{m_f} \quad (2.2)$$

This equation is valid under the following assumptions: the only force acting on the LV is the thrust (free gravity, free drag space flight), thrust parallel to velocity vector and constant effective exhaust velocity v_e . Introducing the mass ratio MR between final and initial mass

$$MR = \frac{m_f}{m_0} \quad (2.3)$$

and the structural coefficient k_s , which is an indicator that express the relative amount of structural mass,

$$k_s = \frac{m_s}{m_p + m_s} \quad (2.4)$$

Eq. (2.2) can be also written as:

$$\Delta v = -v_e \ln \left[\lambda_u \left(1 - k_s \right) + k_s \right] \quad (2.5)$$

Eq. (2.5) encapsulates all the physical principles and disciplines for designing a LV. In fact, the term v_e represents the propulsion system, k_s the structure, λ_u the mass budget and Δv is the energy necessary to go to orbit, which depends by the aerodynamic shape, trajectory and GNC. Supposing $\lambda_u = 0$, the maximum Δv that can be produced is

$$\Delta v = v_e \ln \frac{1}{k_s} \quad (2.6)$$

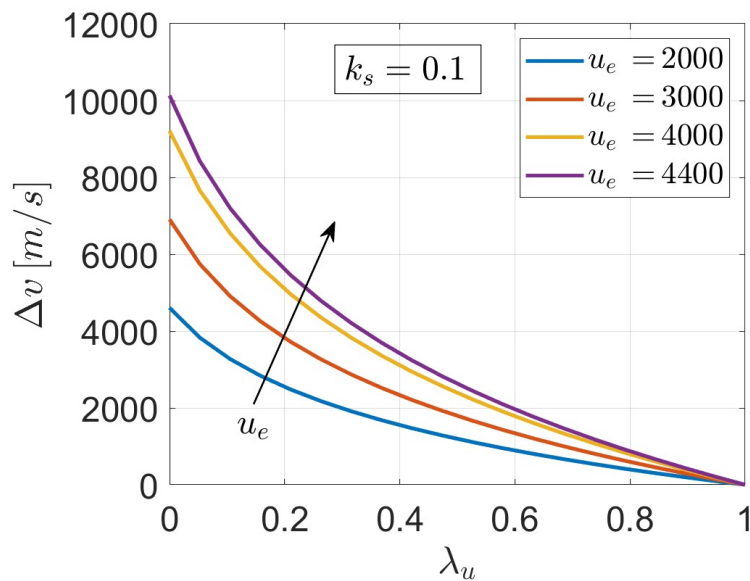


Figure 2.2: Theoretical performance of a SSTO.

In Fig. 2.2 is shown the Δv in function of the payload ratio and the effective exhaust velocity for a fixed structural coefficient of 0.1. It can be noticed that with the current available technology, considering an hypothetical Single Stage to Orbit (SSTO) propelled by liquid oxygen and hydrogen, the maximum velocity gain is 10 km/s . This amount of energy is just enough to get into Low Earth Orbit (LEO), however the payload mass is equal to zero, carrying into space just the LV structure. For this reason, the possible ways to augment the payload mass are to reduce the structural coefficient or to resort to staging. Thus, the LV is divided N stages which vary from 2 to 4 and the Eq. (2.2) becomes:

$$\Delta v = - \sum_{j=1}^N u_{e_j} \ln(MR_j) \quad (2.7)$$

In this thesis, the launch vehicle has been designed following the flowchart displayed in Fig. 2.3.

- a) Once the inputs are defined, the most important of which are payload mass and the target orbit, the design process starts by calculating the total mission Δv . This quantity represents the energy necessary to reach the orbit and it principally depends by the launch site latitude, the orbital parameters and the velocity losses, which are not known a priori but are estimated through one of the design variables.
- b) The next step consists in the definition of the propulsion system and the launch vehicle mass budget. These two aspects are strongly coupled, indeed they interact inside a design loop managed by a Lagrangian optimizer described in detail in App. A. The optimizer finds the propellant mass distribution that minimizes the LV global lift off mass while respecting the constraint of total mission velocity, including the velocity losses estimated previously.
- c) At the end of this loop it is also determined the LV geometry profile necessary to evaluate the aerodynamic coefficients. In particular, the drag coefficient is fundamental to determine the trajectory of the launch vehicle.
- d) At this point, the mass, geometry and the loads are known, thus the process ends with the creations of the FEM model and the structural analysis (modal, static and buckling) can be carried out by the real FEM solver or its surrogate.

Nevertheless, this design process achieves convergence when the total mission velocity, computed post-trajectory analysis, aligns with the a priori educated estimate made at the outset (via the corresponding design variable of velocity losses). Besides, the mission must comply several constraints such as maximum acceleration induced to payload, maximum angle of attack, minimum transfer orbit perigee altitude, defined falling points of the stages, etc. Therefore, the process is managed by an external optimizer which chooses the proper design variables to minimize or maximize the objective functions while respecting all the mission constraints. From the MDO point of view the design process is shown also in Fig. 2.4 through the discipline interaction matrix. The objectives of the launch vehicle MDO, shown in Tab. 2.1, are the payload mass, which must be maximized and the Gross Lift-Off Mass (GLOM) which has to be minimized. The total amount of input is about 350, however about 60 are design variables, as it can be noticed in Tab. 2.2. For every design variable is expressed the number of appearances in function of the number of stages N . The constraints are listed in Tab. 2.3, their total number is about 40, meaning that the studied problem is highly constrained. The design blocks will be discussed in detail in the following sections of this chapter.

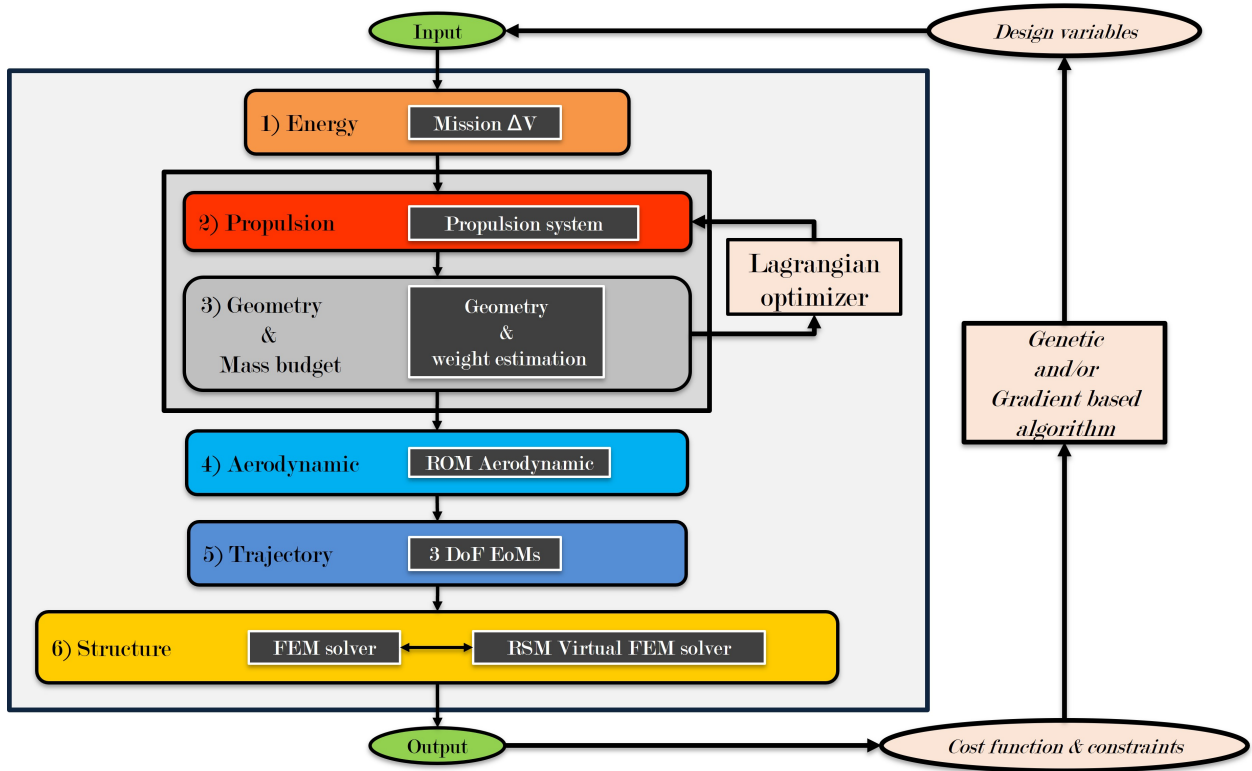


Figure 2.3: LV MDO flowchart.

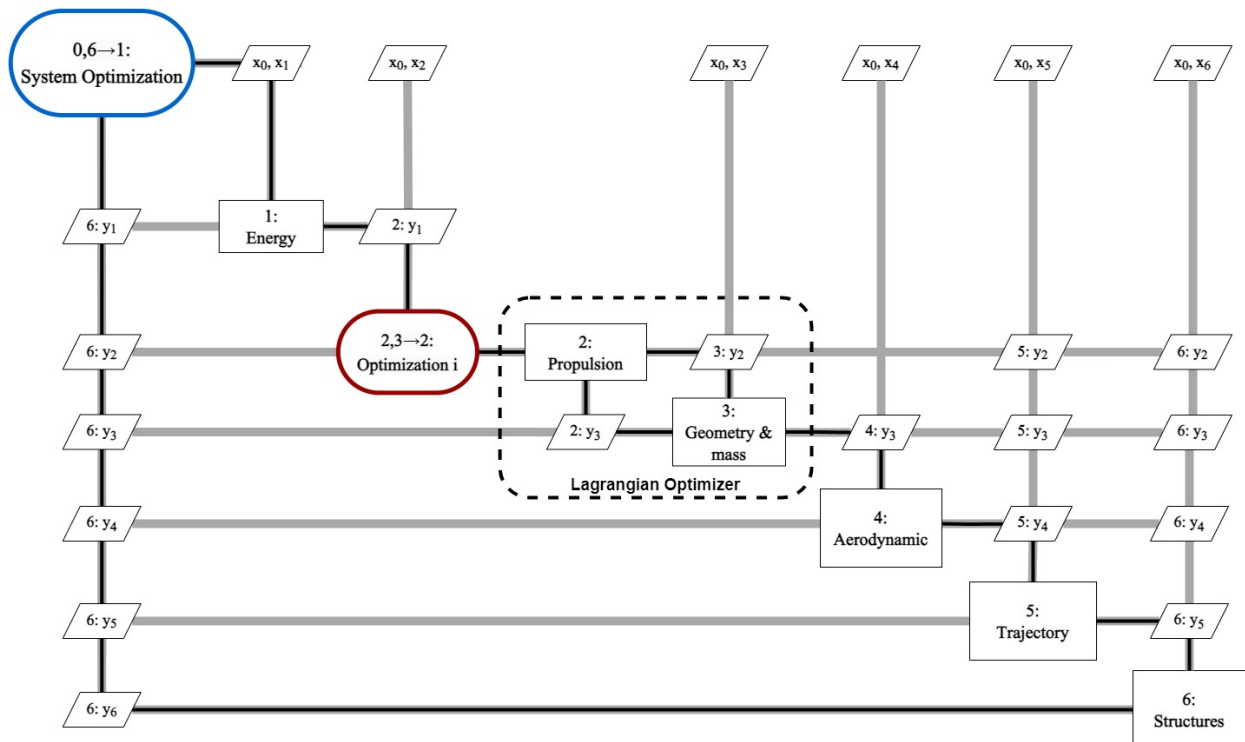


Figure 2.4: LV MDO schematic.

Table 2.1: Objectives.

Output parameter	Symbol	Number	Type	Class
GLOM	m_0	1	minimize	mass
Payload mass	m_{pl}	1	maximize	mass

Table 2.2: Design variables.

Variable	Symbol	Number	Type	Class
Upper mass	m_{up}	1	continuous	mass
Percentage of velocity losses	$\eta_{\Delta V}$	1	continuous	energy
1 st stage diameter	D_{s_1}	1	continuous	structure
Upper stages diameter	$D_{s_{up}}$	$N - 1$	continuous	structure
Tank flattening coefficient	h_d/R_s	N	continuous	structure
Interstage thickness	t_{is}	$N - 1$	continuous	structure
Interstage stringers number	N_{str}	$N - 1$	discrete	structure
Interstage stringers dimension	r_{str}	$N - 1$	continuous	structure
Equipment bay thickness	t_{eb}	1	continuous	structure
Throat diameter	D_t	N	continuous	propulsion
Nozzle expansion ratio	ε	N	continuous	propulsion
SRMs web fraction	wf	N	continuous	propulsion
1 st stage adimensional web points	X_w	6	continuous	propulsion
1 st stage adimensional burning surface points	Y_{S_b}	6	continuous	propulsion
Upper stage max burning time	$\tau_{b_{up}}$	1	continuous	propulsion
Azimuth	A_z	1	continuous	trajectory
Pitch over angle	ϑ_{po}	1	continuous	trajectory
Pitch over time	τ_{po}	1	continuous	trajectory
Coasting time	τ_c	$N + 1$	continuous	trajectory
Stage initial cmd angle	ϑ_{cmd_i}	$N + 1$	continuous	trajectory
Stage final cmd angle	ϑ_{cmd_f}	$N + 1$	continuous	trajectory
Stage bts coefficient	ξ_{bts}	$N + 1$	discrete	trajectory

Table 2.3: Constraints.

Output parameter	Symbol	Number	Type	Class
Stage length vs diameter ratio	L/D	N	inequality	propulsion
Nozzle exit vs stage diameter ratio	D_e/D_c	N	inequality	propulsion
Nozzle exit vs separation pressure ratio	p_e/p_{sep}	1	inequality	propulsion
Upper stage burning total time	$\tau_{burn_{max}}$	1	inequality	propulsion
Maximum dynamic pressure	q_{max}	1	inequality	trajectory
Angle of attack SRM endo-atm	$AoA_{endo_{max}}$	$N - 1$	inequality	trajectory
Angle of attack SRM exo-atm	$AoA_{exo_{max}}$	$N - 2$	inequality	trajectory
Product between q & AoA	$(q \cdot AoA)_{max}$	1	inequality	trajectory
q at 1 st stage separation	$q_{1_{sep}}$	1	inequality	trajectory
Aero-thermal heat flux after F/S	\dot{q}_{max}	1	inequality	trajectory
Pitch over angular rate	$\dot{\vartheta}_{po}$	1	inequality	trajectory
Transfer orbit perigee	h_{ptr}	1	inequality	trajectory
Stage falling point latitude	lat_f	$N - 1$	inequality	trajectory
Stage falling point longitude	lat_f	$N - 1$	inequality	trajectory
Delta target orbit perigee	Δh_p	1	inequality	trajectory
Delta target orbit apogee	Δh_a	1	inequality	trajectory
Delta target orbit inclination	Δi_t	1	inequality	trajectory
Acceleration induced to payload	a_c	N	inequality	structure
Buckling load multiplier at max $q \cdot AoA$	blm	5	inequality	structure
Static stress vs ultimate static stress	σ/σ_{UTS}	N	inequality	structure

2.2 Orbit energy requirements and velocity losses

Ideally, for a circular orbit, the total mission velocity coincides with the velocity of the orbit, which is given by Eq. (2.8).

$$v_c = \sqrt{\frac{\mu_{\oplus}}{r_c}} \quad (2.8)$$

In reality, to achieve a circular orbit around a central body, a launch vehicle must produce a change in magnitude velocity greater than the net inertial velocity of the orbit v_c , because of losses due to gravity Δv_g , steering Δv_s and drag Δv_d . Indeed, the total mission Δv_{tot} is expressed as follows:

$$\Delta v_{tot} = v_c + \Delta v_g + \Delta v_d + \Delta v_s \pm \Delta v_{rot} \quad (2.9)$$

where Δv_{rot} is the Earth's rotational velocity. Depending on the launch direction (westward or eastward), it results in either an addition or a reduction of the required mission velocity.

Gravity losses represent the amount of energy needed to overcome gravity, in fact, during the flight, gravity continues to retard the vehicle and the gravity loss term increase.

$$\Delta v_g = \int_{t_0}^{t_f} g(r) \sin \gamma dt \quad (2.10)$$

It is noted that the gravity losses are as low as the flight path angle is close to zero. This would

suggest to start the LV with a horizontal axis, rather than vertical, but this would lead to a long portion of the trajectory developed within the atmosphere, with consequent unacceptable lateral loads on the launch vehicle. These losses can be contained reducing the combustion time, which means to increase the thrust to leave the total impulse unchanged. However the thrust increment implies an augment of the acceleration induced to payload. Lastly the gradual decay of the local gravity acceleration does not compensate for the growth of other terms, indeed the local g at 300 km is 91 % of the reference value on Earth's surface (see Ref. [72]).

Drag losses represent the losses due to the aerodynamic drag D which always acts in the opposite direction of the relative speed.

$$\Delta v_d = \int_0^{t_f} \frac{D}{m} dt \quad (2.11)$$

To contain these losses, it is necessary to have an LV silhouette with a low aerodynamic coefficient C_D and to quickly cross the lower, denser layers of the atmosphere. It is then observed that the magnitude of the ratio D/m is proportional to the ratio S_{ref}/m , which in turn is proportional to the ratio S_{ref}/V ; therefore, these losses are relatively unimportant for heavy launch vehicle.

Steering losses appears when the direction of the thrust T does not coincide with the one of the velocity vector.

$$\Delta v_s = \int_0^{t_f} \frac{T}{m} [1 - \cos(\delta_{TVC} + \alpha)] dt \quad (2.12)$$

To reduce these losses the angle of attack, α should be close to zero for the entire flight, however this condition does not satisfy the actuation of the maneuvers required by trajectory optimization.

The choice of the launch site can represent a velocity gain or loss depending on the latitude, the kind of orbit and the azimuth. The velocity due to the Earth rotation in function of the launch site latitude δ_{LS} is given by:

$$\Delta v_{rot} = \omega_{\oplus} R_E \cos \delta_{LS} \quad (2.13)$$

where ω_{\oplus} is the Earth spin rate and R_E is the equatorial radius. The Earth rotates towards the east, therefore, launching eastward permits to take advantage of the Earth's rotation; on the other hand, launching other azimuth directions means that this velocity term must be canceled out, becoming a velocity loss.

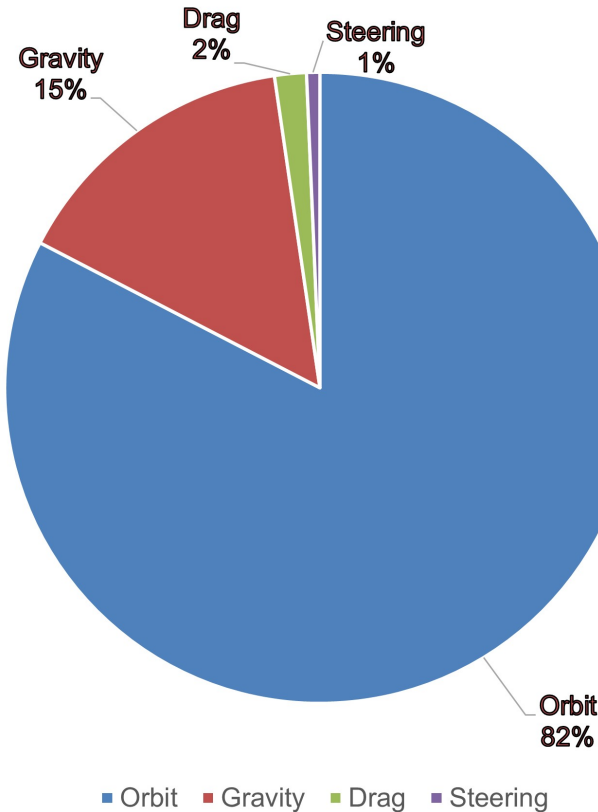


Figure 2.5: Velocity losses of Titan IV LV (data taken from Ref.[72]).

An example of total mission velocity breakdown of a launch vehicle is displayed in Fig. 2.5, in which there are the percentage of velocity losses of Titan IV launch vehicle, tanking the data from Ref. [72].

The total mission velocity is the sum of the ideal velocity and the velocity losses, whose amount is not known until the trajectory analysis, thus in order to proceed with the LV design process, it is necessary to introduce an educated guess of the velocity losses $\eta_{\Delta v}$. The definition of this term allows to write the total mission velocity in function of the ideal one.

$$\Delta v_{tot} = \frac{\Delta v_{id}}{1 - \eta_{\Delta v}} \quad (2.14)$$

2.3 Propulsion system

The second phase of the design process consists in the choice of the propulsion system. In this thesis have been considered solid rocket motor and liquid rocket engine.

2.3.1 Solid Rocket Motor

A solid rocket motor houses propellants (fuel and oxidizer) in a solid state. Hence, a power supply system, like in LRE, is not required resulting in a minimal number of components with reduced complexity. Indeed it is constituted only by these parts: motor case, propellant grain, thermal protection, igniter, nozzle and TVC. The igniter initiates the combustion process, causing the propellant grain to burn and generate hot gases that pressurize the chamber. The resulting combustion

products are expelled through the nozzle, converting thermal energy into kinetic energy and creating thrust. The propellant grain's shape is the main focus of the design, as the thrust history is linked to the burning surface area. This aspect holds great significance since a basic SRM, once ignited, can not be shut off. The advantages of these motors compared to liquid engines are: their simple design ensures reliability by eliminating accessory components that could fail; possibility of increasing the thrust simply augmenting the length of the propellant grain and low productions costs. However, the specific impulse is lower compared to LRE since the oxidizers restrict the chemical energy due to mechanical constraints. Additionally, re-ignition is impractical as the motor can only be turned off by destroying the casing while the propellant is still burning. Furthermore, the absence of an active cooling system imposes a limitation on the combustion time, because a high burning time increases the throat erosion with a consequent decrease of performance.

Solid rocket propellants are a mixture of fuel and oxidizer. Their composition must meet precise criteria to ensure safety and stability throughout storage and combustion. They need high chemical energy to boost specific impulse, high density to minimize case volume, solid mechanical attributes to endure thermal and dynamic loads, and minimal sensitivity to ambient temperature. They can be classified in two categories: double-base and composite. Regarding the first type, both fuel and oxidizer are stored separately in two distinct mono-propellants like nitroglycerin [$C_3H_5(NO_3)_3$] and nitrocellulose [$C_6H_{10-x}O_{5-x}(NO_3)_x$]. On the other hand, the second type is a heterogeneous blend of fuel, oxidizer, and a binder, such as metallic powders (aluminum), ammonium perchlorate (AP) [NH_4ClO_4] and hydroxyl-terminated polybutadiene (HTPB). The binder's purpose is to maintain the cohesion of metallic powders and crystalline oxidizer against pressure, temperature, and acceleration changes. The propellant grain is manufactured by casting a blend that starts as a liquid and then solidifies, conforming to the shape of the mandrel within the combustion chamber. The governing equation of the combustion process is the De Vieille-Saint Robert law (Eq. (2.15)), which links the chamber pressure p_c and the propellant burning rate r_b :

$$r_b = a(T_i) p_c^n \quad (2.15)$$

where $a(T_i)$ is a parameter that depends on the initial temperature T_i and n is the combustion index. The motor functioning is based on the balance between the mass flow rate of the combustion gasses produced by the burning propellant \dot{m}_b and the mass flow rate of the nozzle \dot{m}_t . However this balance is affected by several uncertainties, which are taken into account by the non-ideal ballistic parameters: scale factor SF , *hump*, combustion and thrust efficiencies, respectively η_{c^*} and η_{c_F} . The scale factor SF explains the differing behavior of small-scale bombs (used to measure the burning rate of a particular propellant) compared to real SRMs. In fact, the scale factor of a larger propellant grain is higher due to increased thermal exchange. Typically, the scale factor ranges from 1% to 7% as indicated in Ref. [73].

The *hump* effect refers to a change in burning rate across the propellant web due to the higher burn rate along the flow lines formed during casting. Studies suggest that this effect is caused by the non-spherical shape of AP particles, which align their axes during casting. As a result, the burning rate can be 5% to 10% higher along the web. Consequently, the motor bore exhibits a low-high-low burning rate behavior as it burns back as reported in Ref. [74].

The combustion efficiency η_{c^*} , measures the shift of the grain combustion products composition

and combustion chamber conditions with respect to the ideal equilibrium conditions. This parameter swings between a minimum of 95 % and a maximum of 99 % as indicated in Ref. [75].

$$\eta_{c^*} = \frac{\int_0^{t_b} \frac{p_c(t) A_t(t)}{c^*(t)} dt}{m_p} \quad (2.16)$$

The thrust efficiency η_{c_F} characterizes all the thrust losses, divergence, boundary layer losses, two phase, and kinetics effects in the nozzle flow (see Ref. [75]) To evaluate it, if has been performed a static firing test in a vertical test bench is used Eq. (2.17)

$$\eta_{c_F}(t) = \frac{\tilde{R}(t) - \left[m_{SRM}(t=0) - \int_0^t \frac{p_c(\tau) A_t(\tau)}{c^*(\tau)} d\tau \right] g_0}{C_F(t) p_c(t) A_t(t)} \quad (2.17)$$

otherwise, in case of horizontal test bed or instrumental flight measures is adopted Eq. (2.18).

$$\eta_{c_F}(t) = \frac{T(t)}{C_F(t) p_c(t) A_t(t)} \quad (2.18)$$

The mean value of η_{c_F} usually is 93 %.

SRM propulsion model

Our solid rocket motor propulsion model is based on the prediction model developed in Ref. [76]. The vacuum thrust $T_{vac}(t)$ is calculated directly starting from the combustion surface vs web trend $S_b(w)$ passing through the chamber pressure $p_c(t)$: ($S_b(w) \mapsto p_c(t) \mapsto T_{vac}(t)$). The burning surface is the area of the propellant grain exposed to combustion gases. The propellant grain recedes normally to its surface along the web. Thus, the $S_b(w)$ depends on the geometrical shape of the propellant grain. In this thesis, the burning surface is evaluated through linear interpolation of specific reference points on the plane S_b vs web, as it is shown in Fig. (2.6(a)); X_w coordinates are normalized on the maximum web w_{max} i.e. the maximum thickness of propellant grain measured in radial direction; while Y_{S_b} coordinates are normalized on the average burning surface, which is the ratio between propellant volume V_p and w_{max} ($S_{b_{avg}} = V_p/w_{max}$).

$$\begin{aligned} X_w &= \frac{w}{w_{max}} \\ Y_{S_b} &= \frac{S_b}{S_{b_{avg}}} \end{aligned} \quad (2.19)$$

The others required input of the prediction model are all the non-ideal ballistic parameters and efficiencies. Consequently, the steps of the algorithm are as follows in order to obtain SRM behavior and performance:

1. establishing the first equilibrium point at steady state;
2. interpolation of combustion surface vs web table, hump evaluation via polynomial approximation, characteristic velocity estimation through chemical equilibrium tables or analytical relationship;
3. calculation of nozzle throat erosion rate and consequently throat area;

4. evaluation of equilibrium pressure and thrust;
5. evaluation of the global performance parameters of the SRM (total and specific impulse).

It is possible to obtain the real mass balance between propellant and throat mass flow rate based on the hypothesis of the zero-dimensional steady-state model (i.e. steady-state conditions, perfect gasses, absence of pressure drop along the motor axis, so the variation of the parameters in only function of time), taking into account the non-ideal ballistic parameters introduced in the previous sections (scale factor SF and $hump$) and related efficiencies (combustion η_{c^*} and thrust efficiency η_{C_F}) as shown in Eq. (2.20):

$$\rho_p S_b(web(t)) SF \cdot hump(w(t)) a(T_i) \left(\frac{p_c(t)}{p_{ref}} \right)^n = \frac{p_c(t) A_t(t)}{\eta_{c^*} c^*(p)} \quad (2.20)$$

where ρ_p is the propellant density, $c^*(p)$ is the characteristic velocity which depends on pressure p , A_t is the nozzle throat area and p_{ref} is the reference pressure. Rearranging this equation the chamber pressure function of time is obtained:

$$p_c(t) = \left(SF \cdot hump(w(t)) \rho_p \eta_{c^*} c^*(p) \frac{a(T_i) S_b(w(t))}{p_{ref}^n A_t(t)} \right)^{\frac{1}{1-n}} \quad (2.21)$$

As derived in Ref. [77], the erosion rate \dot{r}_t is function of the density of the nozzle throat thermal protection ρ_{TP} , the amount of the oxidizing species in the chamber (mainly water vapor M_{ox}), chamber pressure, throat diameter D_t and the nozzle shape (r_{ct} is the radius of curvature at nozzle throat).

$$\dot{r}_t = f \left(\rho_{TP}, M_{ox}, p_c^{0.8}, D_t^{-0.2}, \left(\frac{D_t}{r_{ct}} \right)^{0.1} \right) \quad (2.22)$$

Based on the experimental data on the nozzle throat erosion gained from the experience of VEGA SRM (P80, Zefiro 23, Zefiro 9), this semi-empirical/reduced-order model has been found to be extremely reliable and also to be able to accurately predict the erosion behavior of this class of solid rocket motors very closely, comparable to the results from full CFD simulations. Due to the typical combustion chamber temperature induced by aluminized, high-performance propellants, this model is valid in the diffusion-limited regime, which is applicable for almost the entire combustion time of the SRM. Hence, the throat diameter vs time is calculated by integrating the erosion rate between 0 and burning time t_b (see Eq. (2.23)) and consequently the throat area.

$$D_t(t) = D_{t_i} + 2 \int_0^{t_b} \dot{r}_t dt \quad (2.23)$$

The next step to calculate the vacuum thrust T_{vac} is the evaluation of the vacuum thrust coefficient, which represents the contribution of the nozzle on the thrust. $C_{F_{vac}}$ depends on specific heat ratio γ , Γ (function of γ), nozzle exit pressure p_e , chamber pressure and nozzle area ratio ε as shown in Eq. (2.24).

$$C_{F_{vac}}(t) = \Gamma \sqrt{\frac{\gamma}{\gamma-1} \left\{ 1 - \left[\frac{p_e(t)}{p_c(t)} \right]^{\frac{\gamma-1}{\gamma}} \right\}} + \varepsilon(t) \frac{p_e(t)}{p_c(t)} \quad (2.24)$$

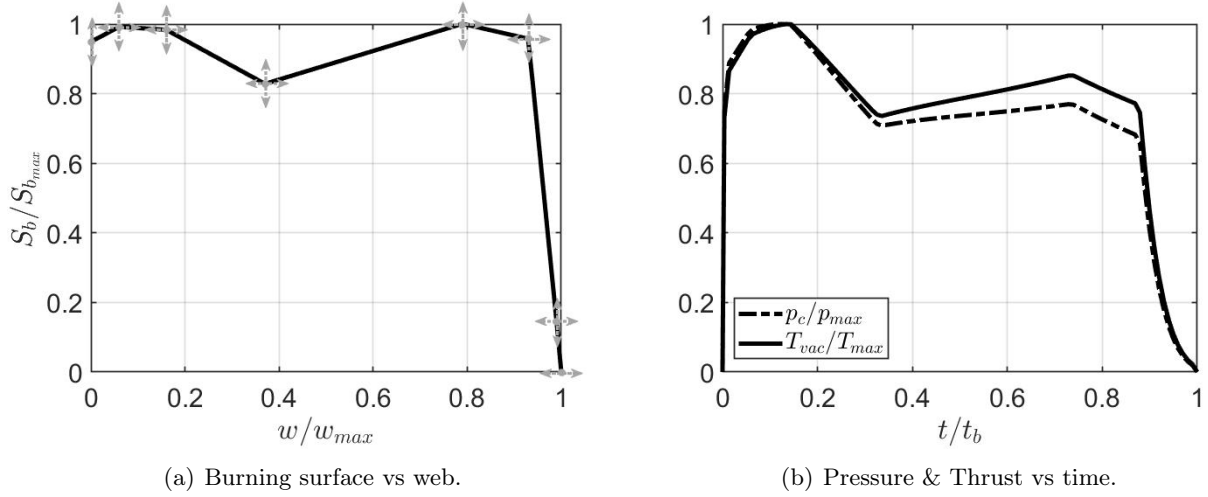


Figure 2.6: From burning surface to thrust.

The vacuum thrust vs time is obtained by multiplying the three terms: $p_c(t)$, $A_t(t)$ and $C_{F_{vac}}(t)$ considering also the thrust efficiency η_{C_F} :

$$T_{vac}(t) = \eta_{C_F} C_{F_{vac}}(t) p_c(t) A_t(t) \quad (2.25)$$

In case of first stage SRM it is necessary to calculate also the atmospheric thrust T (see Eq. (2.26)) that is determined by subtracting to the vacuum one the product between the nozzle exit area A_e and the atmospheric pressure p_a which is function of the flight altitude $h(t)$.

$$T(t) = T_{vac}(t) - p_a(h(t)) A_e \quad (2.26)$$

As regards the vacuum specific impulse $I_{sp_{vac}}$ (Eq. (2.27)), it is defined as the ratio of the total impulse and the product between propellant weight.

$$I_{sp_{vac}} = \frac{\int_0^{t_b} T_{vac}(t) dt}{m_p g_0} \quad (2.27)$$

While the specific impulse at sea level $I_{sp_{sl}}$ is obtained from Eq. (2.26) by dividing each term by the product of average mass flow rate and g_0 .

$$I_{sp_{sl}} = I_{sp_{vac}} - \frac{p_a A_e}{\frac{m_p}{t_b} g_0} \quad (2.28)$$

In Fig. 2.6 is displayed the prediction process of the thrust starting from the burning surface vs time with its relevant points with their degrees of freedom (for physical reasons, first and last point are respectively blocked in web and S_b). Therefore, modifying the positions of the combustion surface vs web relevant points results in a change of the thrust shape. In choosing to act directly on the combustion surface, two objectives are pursued: the first is to determine the impact of the SRM ballistic on the entire design of the launch vehicle; and the second is that this approach lays the foundation for future advances in motor development that directly alter grain geometry.

2.3.2 Liquid Rocket Engine

Liquid Rocket Engine (LRE) uses liquid propellants stored in external tanks and then pumped into the combustion chamber. LREs can be classified on the basis of the propellant combination type or feed system. The propellant combination (oxidizer and fuel) can be cryogenic (liquid oxygen and liquid hydrogen or liquid oxygen and methane), cryogenic-storable (liquid oxygen and kerosene RP1) or storable (nitrogen tetroxide NTO and hydrazine MMH). Liquid rocket engines feed systems (see Fig. 2.7) are divided in pressure feed and pump feed. Each feed system has its own advantages and disadvantages in terms of complexity, reliability, performance and cost. Pressure-fed system (see Fig. 2.7(a)) uses high-pressure gas (mainly helium) to push the propellants into the combustion chamber, which is simple but limits the chamber pressure and thrust. The primary pump feed systems, arranged in terms of generated chamber pressure, are as follows: expander cycle (EC), gas generator (GG), and staged combustion (SC). Expander cycles, illustrated in Fig. 2.7(d), leverage the heat generated from the nozzle or combustion chamber to vaporize propellants and drive the pumps. This method is reliable and allows for efficient cooling, but it imposes constraints on both chamber pressure and thrust. Gas generator cycles, depicted in Fig. 2.7(b), involve the combustion of a portion of the propellants in a distinct chamber to drive the pumps. While this approach is more efficient, it results in the wastage of some propellants. Staged combustion cycles, shown in Fig. 2.7(c), encompass the combustion of all propellants in two stages. The initial stage occurs in a pre-burner to drive the pumps, followed by combustion in the main chamber. This method is highly efficient but entails significant complexity due to the substantial thermal load.

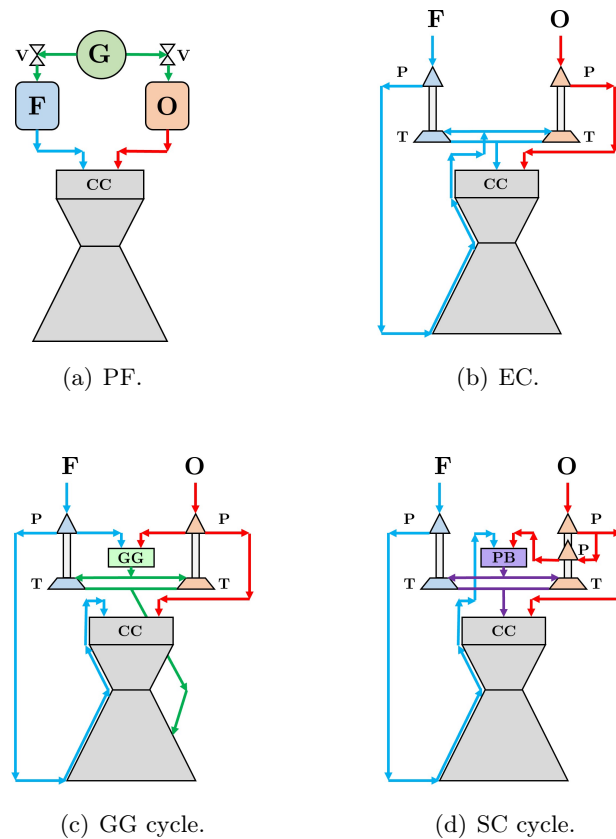


Figure 2.7: Main LRE feed system.

LRE propulsion model

LRE propulsion model is based on Eq. (2.29) where $\dot{m}_p(t)$ is the mass flow rate and I_{spvac} is the vacuum specific impulse. The vacuum thrust trend is directly proportional to the mass flow rate vs time. Having a constant thrust could be an issue due to the progressive increment of the acceleration induced to payload; moreover in case of LRE based first stage is necessary to keep the dynamic pressure under its threshold. Thus in this thesis a simple control law on the mass flow rate has been implemented. Indeed, as shown in Fig. 2.8(a), it is possible to move five control points in the plane mass flow rate vs time in order to reduce the thrust.

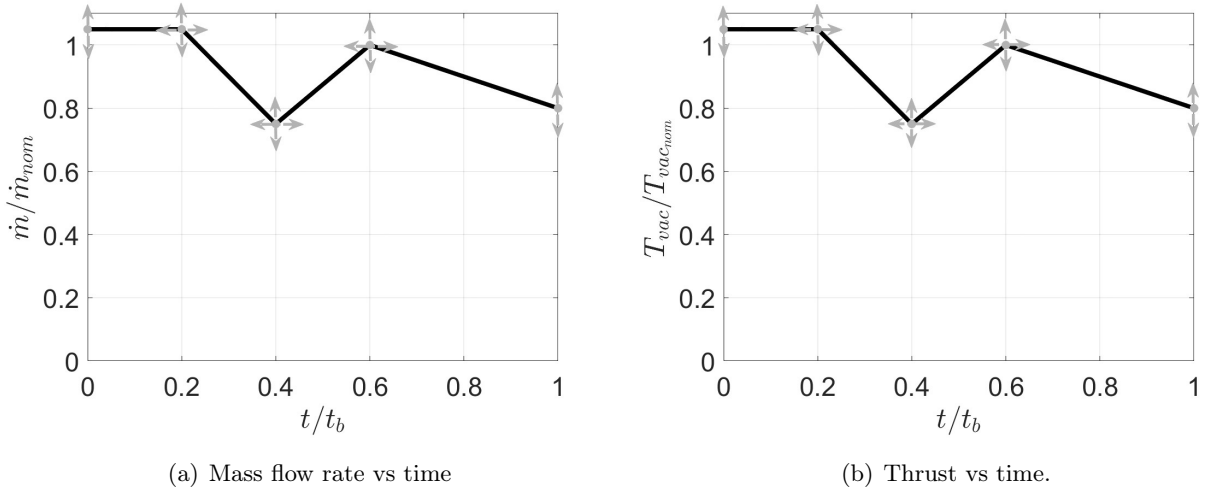


Figure 2.8: From mass flow rate to thrust.

$$T_{vac}(t) = \dot{m}_p(t) I_{spvac} g_0 \quad (2.29)$$

The vacuum specific impulse is given by the product of the theoretical specific impulse $I_{spvac_{th}}$ and combustion and thrust efficiency.

$$I_{spvac} = \eta_{c^*} \eta_{C_F} I_{spvac_{th}} \quad (2.30)$$

The specific impulse at sea level is calculated in the same way of Eq. (2.28).

$$I_{sp_{sl}} = I_{spvac} - \frac{p_a A_e}{\dot{m}_{nom} g_0} \quad (2.31)$$

The theoretical specific impulse depends on the propellant combination (oxidizer and fuel type), mixture ratio O/F , chamber pressure and nozzle expansion ratio.

$$I_{spvac_{th}} = f(ox, fuel, O/F, p_c, \varepsilon) \quad (2.32)$$

This theoretical quantity is evaluated by the computer program *Chemical Equilibrium with Applications (CEA)* of NASA described in Refs. [78] and [79]. The program is written in Fortran and it requires a text input file; two example are reported hereunder:

[E1]: Example of input file for a first stage: Lox-Methane, $O/F = 3$, $p_c = 100$, $p_c/p_e = 1000$
prob case = rocket frozen nfz=2

```

o/f=3.000000
p,bar=100.000000
pip=1000.000000
reac
fuel CH4(L) wt=1. t,k=111.643000
oxid O2(L) wt=1. t,k=90.170000
output massf trans siunits trace=1e-6
plot
o/f aeat(fr) pip(fr) t isp(fr) ivac(fr) cf(fr) gamma pranfz vis
end

```

[E2]: Example of input file for a second stage: Lox-Hydrogen, $O/F = 6$, $p_c = 80$, $\varepsilon = 150$

```

prob case = rocket frozen nfz=2
o/f=6.000000
p,bar=80.000000
supar=150.000000
reac
fuel H2(L) wt=1. t,k=20.270000
oxid O2(L) wt=1. t,k=90.170000
output massf trans siunits trace=1e-6
plot
o/f aeat(fr) pip(fr) t isp(fr) ivac(fr) cf(fr) gamma pranfz vis
end

```

For the two examples the common required input are propellant type and temperature, mixture ratio, chamber pressure. Then the code needs or nozzle pressure ratio or nozzle expansion ratio. In case of a first stage it is better to give in input the pressure ratio, to avoid flow separation at sea level; on the other hand for an upper stage is better to directly provide area ratio as it flights in vacuum condition.

2.4 Weight estimation and preliminary sizing

The mass budget of the launch vehicle is strictly connected to the propulsion systems described in the previous section. Indeed, the third phase of the design process is the preliminary sizing of the launch vehicle. There are three ways of calculating the mass of each component of the launch vehicle: based on its geometric characteristics, through mass estimation relationships, or directly given as input.

2.4.1 Solid Rocket Motor

A solid rocket motor's geometrical characteristics are primarily determined by its propellant mass and composition. Generally, the propellant is composed by ammonium perchlorate (NH_4ClO_3), a binder like HTPB and aluminum. The propellant density is determined by the amount of these components.

$$\rho_p = \frac{1}{\frac{\chi_{Al}}{\rho_{Al}} + \frac{\chi_{HTPB}}{\rho_{HTPB}} + \frac{\chi_{AP}}{\rho_{AP}}} \quad (2.33)$$

Essentially, the combustion chamber volume V_{cs} depends on the propellant filling coefficient η_p , whose typical value is around 0.9 as indicated in Ref. [80].

$$V_{cs} = \frac{\frac{m_p}{\rho_p}}{\eta_p} \quad (2.34)$$

The combustion chamber is composed by a cylindrical part and an upper and a lower dome. Geometrically these domes are ellipsoids and for the upper one the volume V_{dup} is given by

$$V_{dup} = \frac{2}{3} \pi R_{cs}^2 H_d \quad (2.35)$$

where R_{cs} is the case radius and H_d is the dome height. Instead, the lower dome is open, so its volume (V_{dl}) is the difference between the spheroid and the empty spheroidal cap:

$$V_{dl} = \frac{2}{3} \pi R_{cs}^2 H_d - \frac{\pi R_{cs}^2 H_e^2}{3 H_d} (3 H_d - H_e) \quad (2.36)$$

where H_e is the height of the empty part. Thus knowing the domes volume the combustion chamber length L_{cs} is given by (Eq. (2.37)),

$$L_{cs} = \frac{V_{cs} - V_{dup} - V_{dl}}{\pi R_{cs}^2} + 2 H_d - H_e \quad (2.37)$$

Mariotte's law for pressure vessel determines the case thickness t_{cs} (Eq. (2.38)) where P_b is the *MEOP* and σ_{UTS} is the material ultimate tensile strength.

$$t_{cs} = \frac{P_b R_{cs}}{\sigma_{UTS}} \quad (2.38)$$

In this work, the thickness of the aft and forward skirt is the same of the case and the skirt length is proportional to the case one. The polar boss is modeled as a toroidal reinforcement around the lower dome opening. As regards the nozzle, its length depends on the divergence angle θ_{div} , the throat D_t and the exit diameter D_e . The constant k_{nzl} is equal to 1 for ideal conical nozzle, instead is equal to 0.8 for bell shaped nozzle.

$$L_{nzl} = k_{nzl} \frac{D_e - D_t}{2 \tan \theta_{div}} \quad (2.39)$$

Solid Rocket Motor (SRM) geometry is needed in order to determine the mass of each component. Specifically, the case mass m_{cs} , motor skirts m_{sk} , and polar bosses m_{pb} are calculated by multiplying the volume by the material density. As for the igniter, the nozzle and the thermal insulation, their masses are estimated in accordance with the relationships found in Ref. [72]. Accordingly, the igniter mass is directly proportional to the SRM cavity empty volume V_{cav} (Eq. (2.40)). The thermal protection mass is primarily a function of the "wet" area of the combustion chamber that is exposed to the burning gases A_w in Eq. (2.41), where L_{cs}/D_{cs} is the case length vs diameter ratio and L_{sub} is the percentage of case length in which the nozzle is submerged. Eq. (2.42) represents the nozzle mass which is correlated to all motor parameters. The factor k_{TVc} which is equal to 1.5

accounts for the weight of the TVC system.

$$m_{ign} = 0.0138 V_{cav} (cm^3)^{0.571} \quad (2.40)$$

$$m_{ins} = 1.788 \cdot 10^{-9} m_p (kg)^{1.33} t_b^{0.965} \left(\frac{L_{cs}}{D_{cs}} \right)^{0.144} L_{sub}^{0.058} A_w (cm^2)^{2.69} \quad (2.41)$$

$$m_{nzlsys} = k_{TVC} \left\{ 0.256 \cdot 10^{-4} \left[\frac{[m_p (kg) c^*]^{1.2} \varepsilon^{0.3}}{p_c (MPa)^{0.8} t_b^{0.6} (\tan \theta_{div})^{0.4}} \right]^{0.917} \right\} \quad (2.42)$$

Therefore, the total *SRM* mass is the sum of all components mass, as described in Eq. (2.43), where m_{nsm} is the mass of non structural components (railways, cables, avionics, whose masses are estimated according to the relationships described in Sub-s. 2.4.5). This mass decomposition permits a higher level of design of both motor and launch vehicle.

$$m_{SRM} = m_{ign} + m_{cs} + m_{sk} + m_{pb} + m_{ins} + m_{nzlsys} + m_{nsm} \quad (2.43)$$

2.4.2 Liquid Rocket Engine

Liquid rocket engine mass principally depends on the propellant choice and the mixture ratio O/F . Indeed, knowing the propellant mass, can be determined the mass of oxidizer and fuel.

$$m_{ox} = m_p \frac{O/F}{1 + O/F} \quad (2.44)$$

$$m_{fuel} = m_p \frac{1}{1 + O/F} \quad (2.45)$$

Then, the volume is obtained considering a percentage for the unused propellant f_{un} , for the ullage f_{ull} and for the shrinkage f_{shr} (only for cryogenic propellant).

$$V_{ox} = (1 + f_{un}) (1 + f_{ull}) (1 + f_{shr}) \frac{m_{ox}}{\rho_{ox}} \quad (2.46)$$

$$V_{fuel} = (1 + f_{un}) (1 + f_{ull}) (1 + f_{shr}) \frac{m_{fuel}}{\rho_{fuel}} \quad (2.47)$$

Assuming a separated tanks configuration, independently by the presence of oxidizer or fuel, each tank length is given by:

$$L_{tank} = \frac{V_{tank} - 2V_d}{\pi R_s^2} + 2H_d \quad (2.48)$$

where V_d and H_d are respectively the volume and the height of the spheroidal dome.

$$V_d = \frac{2}{3} D_s^2 H_d \quad (2.49)$$

Instead, in case of common bulkhead, the length of the tank with just one dome is:

$$L_{tank} = \frac{V_{tank}}{\pi R_{cs}^2} \quad (2.50)$$

For LRE the engine length is the sum of three parts: combustion chamber, nozzle and feeding/injection system. The length of the combustion chamber depends on the characteristic length L^* , which represents the length of an equivalent cylindrical combustion chamber having a section area equal to the throat one. L^* is function of the propellant combination, because different propellants present a diverse characteristic time to correctly react in the chamber. In Tab. 2.4 are shown the typical values for some propellant combination deduced by Refs. [81] and [82].

Table 2.4: Average combustion chamber characteristic length, adapted from Refs. [81] and [82].

Propellant combination	type	L^* [m]
LOX/RP1	cryogenic - storable	1.14
LOX/LH2	cryogenic - cryogenic	0.89
LOX/CH4	cryogenic - cryogenic	2.26

Thus, the combustion chamber length is given by:

$$L_{cc} = \frac{L^* A_t}{A_{cc}} \quad (2.51)$$

where A_{cc} is the combustion chamber area which is equal to the product of the throat area and a contraction factor ε_{cc} that usually is comprised between 2 and 5, as described in Ref. [83]. Very high value of contraction ratio implies the detachment of the combustion chamber wall boundary layer, while very low contraction ratio means too high wall heat flux. The choice of this parameter determines also the length of the nozzle, which is the sum between the convergent and the divergent part:

$$L_{nzl_{LRE}} = \frac{D_{cc} - D_t}{2 \tan \theta_{conv}} + k_{nzl} \frac{D_e - D_t}{2 \tan \theta_{div}} \quad (2.52)$$

where D_{cc} is the combustion chamber diameter, θ_{conv} and θ_{div} are respectively the convergence and divergence angle, typical values are 45 deg and 15 deg . Then, the length of the feeding and the injection system is assumed as a percentage of the sum of the combustion chamber and nozzle length as indicated in Tab. 2.5 taken by Ref. [5].

Table 2.5: Assumed value for feeding and injection system length as taken from Ref. [5].

Feed system	Coefficient k_{fs}
Pressure feed	0.6
Expander cycle	0.8
Gas Generator	1
Staged combustion	1

$$L_{feed,inj} = k_{fs} (L_{cc} + L_{nzl_{LRE}}) \quad (2.53)$$

Therefore the overall liquid rocket engine length is given by:

$$L_{LRE} = L_{cc} + L_{nzl_{LRE}} + L_{feed,inj} \quad (2.54)$$

LRE geometry is needed to determine the mass of each component. Specifically, the mass of

the tanks m_t is principally constituted by the structure m_{st} which is calculated by multiplying the volume by the material density. In case of cryogenic propellant, it is necessary also the insulation m_{inst} , that depends on the propellant type and the internal area A_w .

$$m_{st} = V_{st} \rho_{st} \quad (2.55)$$

$$m_{inst} = k_{ins} A_w \quad (2.56)$$

The constant k_{ins} is equal to 2.88 for liquid hydrogen and 1.123 for LOX as indicated in Ref. [84], the value of 1.123 is assumed valid also for methane, however it is likely too large given the higher temperature of LCH₄, thus in Ref. [85] it is suggested a lower value of 0.98, which might reduce mass significantly. As for the LRE engine mass and its components, their masses are estimated in accordance with the relationships found in Ref. [84]:

$$m_{eng} = T(N) \left(7.81 \cdot 10^{-4} + 3.37 \cdot 10^{-5} \sqrt{\varepsilon} \right) + 59 \quad (2.57)$$

$$m_{ts} = 2.55 \cdot 10^{-4} T(N) \quad (2.58)$$

$$m_{gimb} = N_{eng} 237.8 \left[\frac{T(N)/N_{eng}}{p_c(Pa)} \right]^{0.9375} \quad (2.59)$$

where N_{eng} is the number of engines, which can be greater than one in case of clustering. Therefore, the total mass of an LRE is given by the sum of the tanks and the engine assembly.

$$m_{LRE} = m_t + m_{eng} + m_{ts} + m_{gimb} \quad (2.60)$$

2.4.3 Interstage

The Interstage (IS) is defined as either a cylindrical or truncated conical shell, depending on whether two consecutive stages have the same diameter or a different diameter. The IS height depends on the length of the upper stage nozzle and its diameter:

$$H_{IS} = L_{nzl_{up}} + k_{IS} D_{s_{up}} \quad (2.61)$$

the coefficient k_{IS} is equal to 0.2. The interstage usually presents both axial and longitudinal reinforcements (respectively stringers and formers). By knowing its geometric parameters, such as the thickness, the lower and upper diameters, the height, and the number and thickness of the stringers and formers, the interstage mass can be directly calculated. As an addition to this mass, Retro-Rockets (RR) and avionics have been included.

$$m_{IS} = m_{IS_s} + m_{IS_{avio}} + m_{IS_{RR}} \quad (2.62)$$

2.4.4 Upper composite module

The upper composite module consists of Equipment bay (EB), fairing, Payload adapter (PLA) and payload. The equipment bay is a cylindrical shell which separates the last stage and the payload adapter. It contains the on-board computer and, depending on the configuration, either the Attitude and Orbit Control Subsystem (AOCS) or a liquid rocket engine. The height of the equipment bay H_{EB} is given by the sum of the upper stage upper dome height h_{dup} and its diameter D_{sup} scaled by a factor k_{EB} which is equal to 0.3.

$$H_{EB} = H_{dup} + k_{EB} D_{sup} \quad (2.63)$$

The fairing is the casing that protects the payload from aerothermal loads. In this work, the fairing shape is inspired by the VEGA fairing; its profile is divided into four sections: truncated cone, cylinder, fillet and nose. The payload adapter is a truncated cone shell which connects the payload to the launch vehicle. In order to find the height of the PLA it has been considered an angle of the cone δ_{PLA} equal to 50 deg , thus the payload adapter height is equal to:

$$H_{PLA} = \tan \delta_{PLA} (R_{us} - R_{PLA}) \quad (2.64)$$

where R_{us} is the upper stage radius and R_{PLA} is the payload adapter upper radius, which can be related to the payload radius through the coefficient k_{PLA} , that can vary between 0.25 and 0.6.

$$R_{PLA} = k_{PLA} R_{PL} \quad (2.65)$$

2.4.5 Avionic and wiring

According to Ref. [84] the avionic mass $m_{avionic}$ is proportional to the lift-off mass m_0 :

$$m_{avionic} = TFR_{avionic} 10 [m_0(\text{kg})]^{0.361} \quad (2.66)$$

where $TFR_{avionic}$ is the the technology reduction factor, that is equal to 0.75 as suggested by Ref. [86]. This avionic mass is equally distributed along the stages.

Another mass that must be accounted is the one of the wiring m_{wiring} , which is calculated as indicated by Ref. [84]:

$$m_{wiring} = 1.058 \sqrt{[m_0(\text{kg})]} (L_{tot})^{0.25} \quad (2.67)$$

where L_{tot} is the total length of the LV. This mass is proportionally distributed to the length of each LV component.

2.5 Aerodynamic of axisymmetric bodies

The fourth stage of the design process involves the determination of aerodynamic properties. Typically, the aerodynamic flow field around a launch vehicle is assessed through CFD analysis. However, for this thesis, the incorporation of CFD within the MDO loop has been omitted due to the substantial computational time it demands. Thus, the LV aerodynamic is obtained through analytical relationships. Indeed, for the subsonic regime the aerodynamic coefficients are calculated consid-

ering the LV as the fuselage of an airplane. Instead, for the supersonic regime pressure and drag coefficients are obtained via the panel method.

2.5.1 Supersonic regime

The method is applied following these steps:

1. interpolation with the desired axial discretization of the LV profile given as input in the coordinate form (x,y) (see Fig. 2.9), where x is the axial coordinate and y is the radial one. The LV axis is so divided in J parts;
2. revolution of the profile of 360 degrees with the step in degrees given by the desired number of circumferential panels K (see Fig. 2.10);
3. for each panel, identified by the couple of values (j, k) is evaluated the angle between the flow and the tangent to the panel $\theta_{p\alpha_{jk}}$ (see Fig. 2.11);
4. the supersonic C_p is calculated according to the Mach number and the LV profile zone using a combinations of three methods: Newton modified theory, Krasnov's empirical formula for cones and supersonic source method for slender bodies;
5. the C_p is numerically integrated along the LV axis to calculate C_D , C_L e CoP, correction coefficients are used to mitigate the overestimation of C_p in the transonic region.

Thus, first it is necessary to create a 3D aerodynamic mesh and then to evaluate the C_p as all the other coefficients depends on it. The pressure coefficient by definition is the ratio between the difference of the total p_0 and static pressure p_s and the dynamic pressure:

$$C_p = \frac{p_0 - p_s}{\frac{1}{2} \rho_\infty v_\infty^2} \quad (2.68)$$

where ρ_∞ and v_∞ are the respectively the density and the velocity of the undisturbed fluid. Every launch vehicle profile can be seen as the combination of three analytical curves: circumferences, parabolas and straight lines. Indeed, a launch vehicle can be divided in zones: fairing nose, fairing tapered zone, conical and cylindrical zones.

The evaluation of the pressure coefficient changes according to the launch vehicle zones and the Mach number. As aforementioned, the C_p is calculated implementing the Newton modified theory, the Krasnov formula for cones in a supersonic flow and the supersonic sources method for slender bodies.¹

¹The supersonic source method, described in Subsec. 2.5.1, is valid only for axisymmetric flow with $AoA = 0$. Nevertheless, based on the satisfactory results achieved in Subsec. 2.5.1, there is a presumption that it can also be utilized in scenarios where AoA is greater than 0. Indeed, with the employed mesh discretization, the launch vehicle is segmented into "slices," each subjected to a flow characterized by a distinct relative angle of attack. This slicing approach provides the crucial information needed for the supersonic source method, specifically, the angle between the flow and each panel.

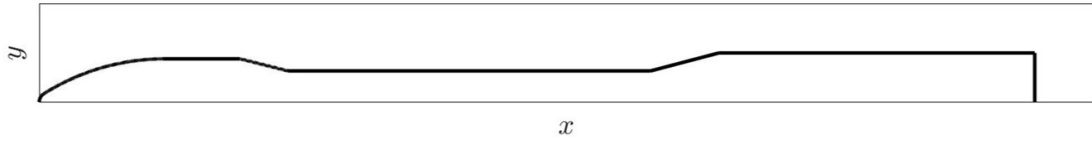


Figure 2.9: Example of LV profile.

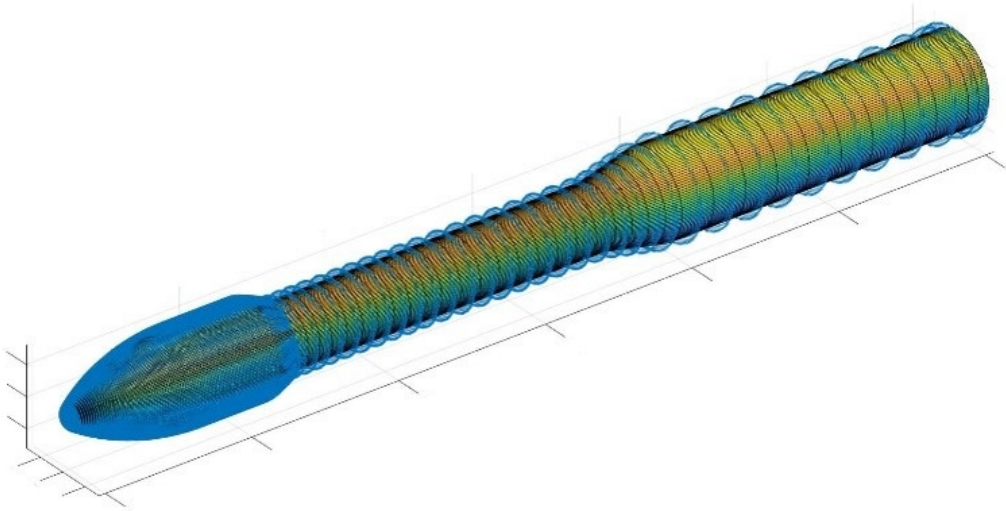


Figure 2.10: Example of 3D aerodynamic mesh.

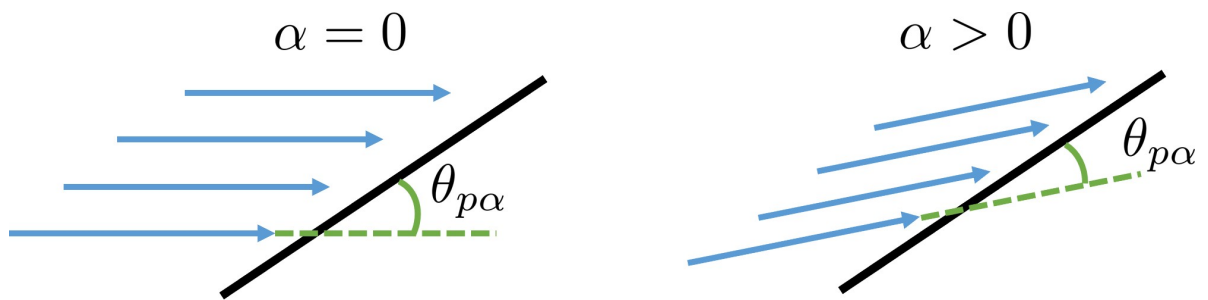


Figure 2.11: Panel angle.

Newton modified theory

According to Newton theory the pressure coefficient is only function of the angle between the body surface and the free stream θ_{p_α} , assuming that the tangential component of momentum is conserved after the interaction. Thus, for the panel (j, k) the value of the pressure coefficient C_{p_N} according to Newton theory is:

$$C_{p_{Njk}} = 2 \sin^2 \theta_{p_{\alpha jk}} \quad (2.69)$$

If, for some panels, the angle $\theta_{p_\alpha}(j, k)$ is negative, $C_{p_N}(j, k) = 0$, because those panels are not directly invested by the flow. However, this theory was modified by Lees (see Ref. [87]) in order to consider also the dependence by the Mach number. Close to the nose of the body, there is a normal shock wave, thus in the stagnation point is verified:

$$C_{p_{max}} = \frac{p_{02} - p_\infty}{\frac{1}{2} \rho_\infty v_\infty^2} = \frac{2}{\gamma M_\infty^2} \left[\frac{p_{02}}{p_\infty} - 1 \right] \quad (2.70)$$

where p_∞ e M_∞ are respectively the pressure and the Mach number of the undisturbed fluid and the total pressure p_{02} is equal to:

$$p_{02} = \left[\frac{(\gamma + 1)^2 M_\infty^2}{4 \gamma M_\infty^2 - 2(\gamma - 1)} \right]^{\frac{\gamma}{\gamma - 1}} \left[\frac{1 - \gamma + 2 \gamma M_\infty^2}{\gamma + 1} \right] \quad (2.71)$$

So, Eq. (2.69) becomes Eq. (2.72), where $C_{p_{N_m}}$ stands for pressure coefficient obtained by Newton modified theory.

$$C_{p_{N_m jk}} = C_{p_{max}} \sin^2 \theta_{p_{\alpha jk}} \quad (2.72)$$

Krasnov empirical equation

In case of conical bodies in an axisymmetric flow can be utilized the empirical formula found in Ref. [88], which is valid up to Mach 8 and cone semiapex angle of 50 degrees.

$$C_{p_{K_r jk}} = \left(0.0016 + \frac{0.002}{M_\infty^2} \right) \cdot \left(\theta_{p_{\alpha jk}}^{1.7} \right) \quad (2.73)$$

Supersonic sources method for slender bodies

The profile of slender bodies can be approximated by a succession of cones of different angles (see Fig. 2.12). However, Eq. (2.73) is valid only locally, so does not consider the effect of the previous profile zones. Thus, it is necessary to use another approach based on supersonic sources as described in Ref [89]. An axisymmetric flow is governed by the following equation:

$$\beta^2 \phi'_{,xx} - \phi'_{,rr} - \frac{1}{r} \phi'_{,r} = 0 \quad (2.74)$$

where ϕ is the potential and $\beta = \sqrt{M_\infty^2 - 1}$. A particular solution is:

$$\phi(x, y) = \int_0^{\xi_1} \frac{f(\xi)}{\sqrt{(x - \xi)^2 - \beta^2 r^2}} d\xi \quad (2.75)$$

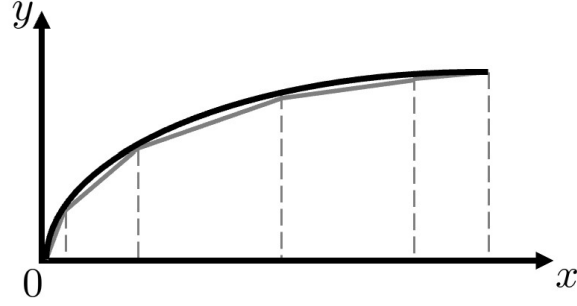


Figure 2.12: Slender body profile.

Inserting Eq. (2.75) in Eq. (2.74), it is satisfied for every function $f(\xi)$, which represents the intensity of the supersonic sources placed along the LV axis. The integral is defined from the origin up to the point $\xi_1 = x - \beta r$, that is the maximum value of ξ for which the integral of the function is real. The point ξ_1 has also a physical meaning, indeed, a point P with coordinates x and r is only influenced by the sources which are inside the Mach anti-cone that starts from point P (see Fig. 2.13). Considering the particular case for which:

$$f(\xi) = C \xi \quad (2.76)$$

and introducing the auxiliary variable,

$$z = \cosh^{-1} \frac{x - \xi}{\beta r} \quad (2.77)$$

the integral can be solved in closed form:

$$\phi = C \int_{\cosh^{-1} \frac{x}{\beta r}}^0 (x - \beta r \cosh z) dz = C x \left[-\cosh^{-1} \frac{x}{\beta r} + \sqrt{1 - \frac{\beta^2 r^2}{x^2}} \right] \quad (2.78)$$

Therefore, the velocity perturbation in axial and radial direction are respectively:

$$\phi_{,x} = C \int_{\cosh^{-1} \frac{x}{\beta r}}^0 dz = -C \cosh^{-1} \frac{x}{\beta r} \quad (2.79)$$

$$\phi_{,r} = -C \int_{\cosh^{-1} \frac{x}{\beta r}}^0 \beta r \cosh z dz = C \beta \sqrt{\frac{x^2}{\beta^2 r^2} - 1} \quad (2.80)$$

Thus, considering a slender body as the succession of n conical solution, can be calculated the value for every j point of the axis discretization:

$$\xi_j = x_j - \beta r_j \quad (2.81)$$

Then, indicating with k the index of the circular discretization, the radial velocity matrix presents the following components:

$$v_{r_{jk}} = \tan \theta_{p_{\alpha_{jk}}} \quad (2.82)$$

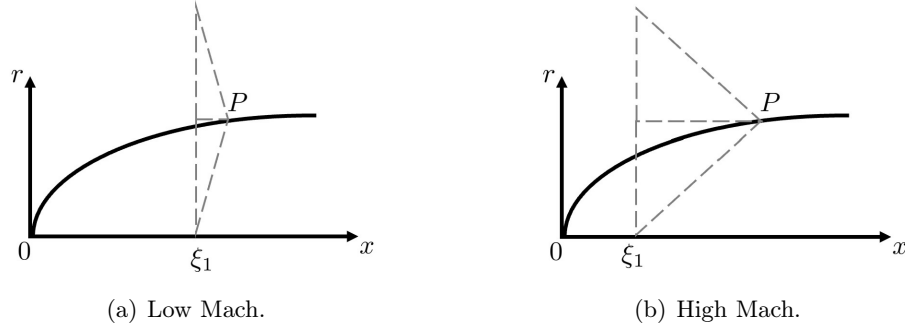


Figure 2.13: Mach's anti-cone projection for two different Mach numbers.

This matrix can be also written as the product of the vector c , that is the vector of the intensity of the supersonic sources and the matrix B :

$$v_{r_{jk}} = c_{jk} B_{jl} \quad (2.83)$$

This matrix is a lower triangular matrix defined as:

$$B_{jl} = \beta \sqrt{\frac{(x_j - \xi_{l-1})^2}{\beta^2 r_j^2} - 1} \quad (2.84)$$

Also the matrix of axial velocity can be written in function of the vector c :

$$v_{x_{jk}} = c_{jk} A_{jl} \quad (2.85)$$

introducing the lower triangular matrix A , defined as:

$$A_{jl} = \cosh^{-1} \left(\frac{x_j - \xi_{l-1}}{\beta r_j} \right) \quad (2.86)$$

Thus, the relationship between axial and radial velocity can be written by substituting the expression of the vector c derived by Eq. (2.83) in Eq. (2.85)

$$v_{x_{jk}} = A_{jl} B_{jl}^{-1} v_{r_{jk}} \quad (2.87)$$

and the pressure coefficient is obtained remembering that for the assumption of small perturbations:

$$C_{pS_{jk}} = -2 v_{x_{jk}} \quad (2.88)$$

Aerodynamic coefficients

The calculation of the pressure coefficient depends on both the mach number and the LV profile zone. Comparison of these analytical relationships with CFD showed that each zone of the LV profile has a better method than the others for estimating C_p . The zones and their methods are summarized in Tabs. 2.6 and 2.7. For Mach number ranges from 1 to 3, the LV profile is divided in three zones: zone I, which is geometrically the fairing nose; zone II, that is the part of LV profile in which the starting point of the supersonic source method is not defined, as the value ξ_j given by

Table 2.6: Calculation of C_p based on profile zone for $Mach \leq 3$.

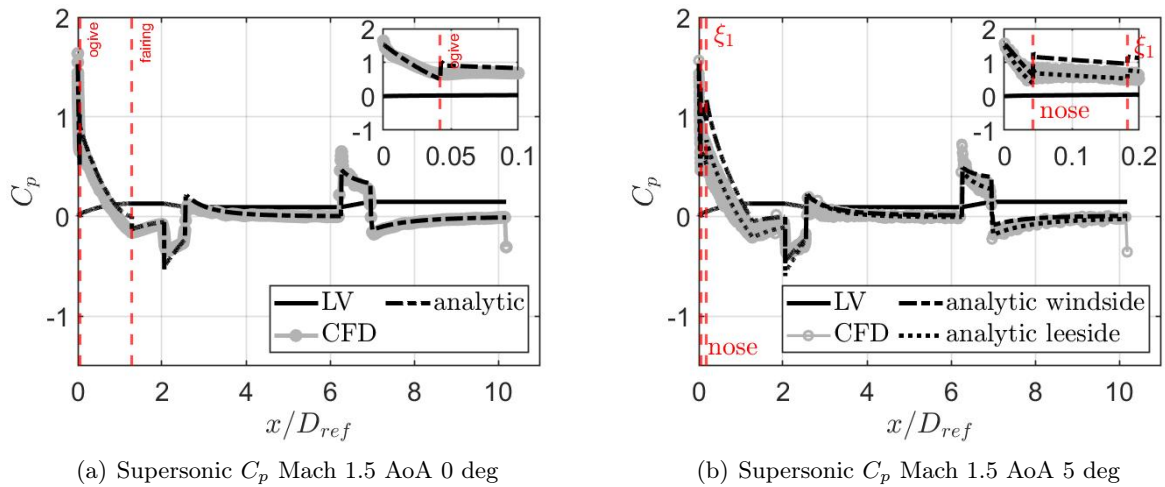
Profile zone	Range	Method
I	$0 < x \leq x \theta_p(x) = 35 \text{ deg}$	Newton modified theory
II	$x \theta_p(x) = 35 \text{ deg} < x \leq \xi_1$	Krasnov's equation
III	$\xi_1 \text{ deg} < x \leq L$	Supersonic source method

Eq. (2.81) is negative; in zone III instead the value of $\xi(j)$ is positive, thus the supersonic source method can be applied. However, the point $\xi(j)$ is function of the Mach number and the supersonic

Table 2.7: Calculation of C_p based on profile zone $Mach > 3$.

Profile zone	Range	Method
I	$0 < x \leq x \theta_p(x) = 35 \text{ deg}$	Newton modified theory
II	$x \theta_p(x) = 35 \text{ deg} < x \leq L$	Krasnov's equation

source method works well for Mach less than or equal to 3, after this limit this method can not be applied because, the starting point moves too far toward the end of the LV profile. The results have been compared with the computational fluid dynamics (CFD) obtained by Ansys Fluent©, as it can be seen in Fig. 2.14. In particular, in Fig. 2.14(a), it displayed the C_p trend along the LV axis for $Mach = 1.5$ at 0 AoA . The field is symmetric, thus for every circumferential zone the trend is unique. The vertical line represent the different zones of the profile in which have been used the aforementioned three different methods. At this Mach number, the aerodynamic code results match the CFD ones very well, specially considering that the running time was less than 0.1 s with respect to 30 minutes. In Fig. 2.14(b) is shown the C_p trend for $Mach = 1.5$ with an AoA of 5 deg ; in this case the field is not symmetric, indeed the CFD results are a band that sweeps all circumferential directions. Of these, there are two for which C_p has a maximum and minimum value, respectively windside (at lower part of the LV) and leeside (at the upper part). Comparing the results, the aerodynamic code overestimate the C_p in the fairing region, however the difference between windside and leeside matches the CFD.

**Figure 2.14:** Comparison between CFD and analytic method.

As for the drag coefficient, for supersonic flow it is calculated by integrating the projection of

C_p in the axial and lateral directions (see Eqs. (2.89) and (2.90)), where $R(x_j)$ is the radius of the annulus, N_{circ} is the number of circular panels, and $n_{ax_{jk}}$ and $n_{lat_{jk}}$ respectively the vectors of the axial and lateral components of the normal of the panel (j, k) .

$$f_{ax}(x_j) = \frac{2\pi R(x_j) \sum_{k=1}^{N_{circ}} C_{p_k}(x_j) n_{ax_k}(x_j)}{N_{circ}} \quad (2.89)$$

$$f_{lat}(x_j) = \frac{2\pi R(x_j) \sum_{k=1}^{N_{circ}} C_{p_k}(x_j) n_{lat_k}(x_j)}{N_{circ}} \quad (2.90)$$

$f_{ax}(x)$ e $f_{lat}(x)$ are non dimensional force per unit length, thus to obtain the dimensional axial $F_{ax}(x)$ and lateral $F_{lat}(x)$ force it is necessary to integrate along the LV axis and multiply for the dynamic pressure (Eqs. (2.89) and (2.90)).

$$F_{ax} = \frac{1}{2} \rho_{\infty} v_{\infty}^2 \int_0^l f_{ax}(x) dx \quad (2.91)$$

$$F_{lat} = \frac{1}{2} \rho_{\infty} v_{\infty}^2 \int_0^l f_{lat}(x) dx \quad (2.92)$$

The drag D is the combination of axial and lateral force considering the angle of attack α and it has the opposite direction of the relative speed vector. The drag coefficient C_D is obtained dividing D by the dynamic pressure.

$$D = F_{ax} \cos \alpha + F_{lat} \sin \alpha \quad (2.93)$$

$$C_D = \frac{D}{\frac{1}{2} \rho_{\infty} v_{\infty}^2 S_{ref}} \quad (2.94)$$

In addition, the center of pressure (CoP) is calculated by integrating the non-dimensional lateral force per unit length (Eq. (2.89)). This parameter is critical for balancing the torque acting on the launch vehicle and thus ensuring its stability.

$$x_{CoP} = \frac{\int_0^l x f_{lat}(x) dx}{\int_0^l f_{lat}(x) dx} \quad (2.95)$$

2.5.2 Subsonic regime

In subsonic regime, the flow field around the LV is more complex with respect to the supersonic one, since there is a mutual influence between the panels of the LV. For this reason, the logic already applied for the supersonic flow can not be implemented. Instead, for subsonic flow, the drag coefficient is assumed to be given by two contributions: C_{D_0} and base drag C_{D_b} . To estimate C_{D_0} a correlation was implemented based on the aerodynamic drag of the aircraft fuselage, described in Ref. [90], where C_{fe} is the equivalent viscous friction coefficient and S_{wet} is the wet surface area.

$$C_{D_0} = C_{fe} \frac{S_{wet}}{S_{ref}} \quad (2.96)$$

For the base drag it is implemented the relationship found in Ref. [91].

$$C_{D_b} = 0.12 + 0.13 M^2 \quad (2.97)$$

Thus in subsonic regime the drag coefficient is given by:

$$C_D = C_{D_0} + C_{D_b} \quad (2.98)$$

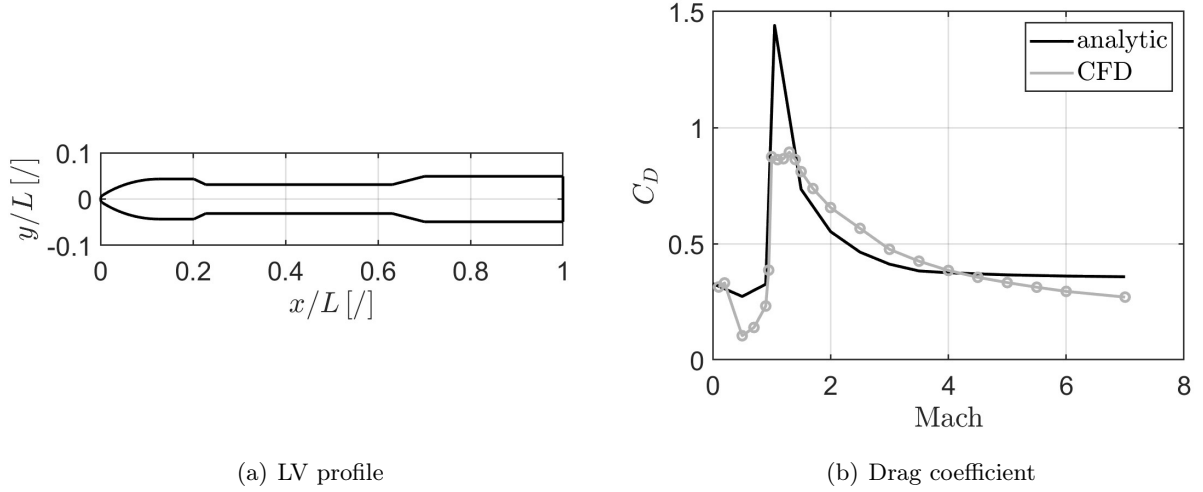


Figure 2.15: Comparison between CFD and analytic drag coefficient $AoA = 0$.

Figure 2.15 displays the comparison between the drag coefficient calculated by the described analytical method and the one obtained by CFD. The considered LV profile is shown in Fig. 2.15(a) at $AoA = 0$. The analytic C_D is the combination of Eqs. (2.98) and (2.94) and as it can be observed in Fig. 2.15(b) there is an overestimation of the drag coefficient in transonic regime caused by the low accuracy of the analytical method at low supersonic Mach. To account for this, correction coefficients were applied to the analytical C_D curve to match that obtained from CFD. The difference of the drag coefficient trends is balanced by the computational time: 12 h of CFD compared to 0.15 s of the analytic method. However to increase the accuracy of the aerodynamic model, a possible solution is the adoption of a neural network based aerodynamic described in App. C.

2.6 Trajectory analysis

Once defined the aerodynamic properties, the fifth phase of the design process is the trajectory analysis from lift-off to target orbit.

2.6.1 Gravity and atmospheric model

A spherical Earth model, as the one of Ref. [92], has been adopted considering the Earth mean radius R_{\oplus} , calculated considering equatorial R_e and polar radius R_p .

$$R_{\oplus} = \frac{2R_e + R_p}{3} = 6371 \text{ km} \quad (2.99)$$

Therefore, without taking into account the effect of the zonal harmonics J_2 , the Newton's law of gravitation has been implemented (see Eq. 2.100), where \mathbf{g} is the gravitational acceleration, \mathbf{r} is

the position vector and μ_{\oplus} is the Earth gravitational constant.

$$\mathbf{g} = -\frac{\mu_{\oplus}}{r^3}\mathbf{r} \quad (2.100)$$

As regards the evaluation of air density and pressure, until 86 km the values of the US standard atmosphere are interpolated (see Ref. [93]); while above this altitude is used the exponential law:

$$\rho_a = \rho_0 e^{-\frac{h}{H}} \quad (2.101)$$

where ρ_0 is the density at sea level and H is the atmospheric scale height, which has been set to 7200 m.

2.6.2 Ascent trajectory

In order to evaluate the trajectory, the 3 DoF model is adopted, so the LV is considered as concentrated mass point. The equations of motion can be projected on different reference frame. In this work, it is chosen the Earth-Centered Earth-Fixed (ECEF), because it is easier to interface with the other disciplines inside the MDO cycle. Thus, the EoMs, derived by Ref. [94] are the following:

$$\begin{aligned} \dot{r} &= v \sin \gamma \\ \dot{\lambda} &= \frac{v \cos \gamma \sin \chi}{r \cos \delta} \\ \dot{\delta} &= \frac{\cos \gamma \cos \chi}{r} \\ \dot{v} &= \omega_{\oplus}^2 r \cos \delta (\cos \delta \sin \gamma - \sin \delta \cos \gamma \cos \chi) - \frac{\mu_{\oplus}}{r^2} \sin \gamma + \frac{F_v}{m} \\ \dot{\gamma} &= \frac{v \cos \gamma}{r} + 2\omega_{\oplus} \cos \delta \sin \chi + \omega_{\oplus}^2 r \cos \delta \frac{(\cos \delta \cos \gamma + \sin \delta \sin \gamma \cos \chi)}{v} - \frac{\mu_{\oplus}}{r^2} \cos \gamma + \frac{F_{\rho}}{m v} \\ \dot{\chi} &= \frac{v \cos \gamma \tan \delta \sin \chi}{r} + 2\omega_{\oplus} (\sin \delta - \cos \delta \tan \gamma \cos \chi) + \frac{\omega_{\oplus}^2 r \cos \delta \sin \delta \sin \chi}{v \cos \gamma} + \frac{F_{\eta}}{m v \cos \gamma} \end{aligned} \quad (2.102)$$

where r is the position with respect to the center of the Earth, λ is the longitude, δ is the latitude, v is the relative speed to an Earth-fixed observer, γ is the flight-path angle (angle between local horizon and velocity), χ is the heading angle (angle formed by the component of the velocity projected onto the local horizontal plane and the north direction) and ω_{\oplus} is the Earth spin rate. Concerning the external forces acting on the launch vehicle, the thrust T , drag D , and lift L are represented in the wind reference frame, assuming that the thrust is aligned with the launch vehicle axis (i.e., thrust vector angle $\delta_{TV C}$ is zero). These forces are encapsulated within the terms F_v , F_{η} , and F_{ρ} in Eq. (2.103), where β denotes the slip angle.

$$\begin{aligned} F_v &= T \cos \alpha \cos \beta - D \\ F_{\rho} &= T \sin \alpha + L \end{aligned} \quad (2.103)$$

$$F_{\eta} = -T \cos \alpha \sin \beta$$

$$\begin{aligned} D &= \frac{1}{2} \rho v^2 C_D S_{ref} \\ L &= \frac{1}{2} \rho v^2 C_{N\alpha} \alpha S_{ref} \end{aligned} \quad (2.104)$$

While the gravity is described by the Newton's law (Eq. 2.99).

The ascent trajectory is divided in phases, which principally can be categorized in propulsive and coasting. Trivially a propulsive phase implies the presence of a non zero trust in the EoMs, conversely during coasting there is just the drag for atmospheric flight and no forces in the exoatmospheric flight. The number of propulsive phase is greater or equal to the number of stages, because LRE stage can be ignites more than one time. Between the propulsive phase, the one of the first stage is the most complex, because the LV needs to tilt from the initial vertical position of the lift-off. Indeed the first stage flight is divided in four sub-phases (see Fig. 2.16), that are categorized based on the value of the pitch angle ϑ , which is the angle between the LV axis and the local horizon:

I the first one is the vertical ascent which last until the altitude is greater than the launch pad;

$$\vartheta(t) = \pi/2 \quad (2.105)$$

II the second one is the pitch over maneuver during which the LV keeps a constant pitch rate to tilt its axis toward the local horizon, the duration is determined by the pitch time t_{po} ;

$$\vartheta(t) = \pi/2 - \frac{(\pi/2 - \vartheta_{po})}{t_{po}} (t - t_{i_{po}}) \quad (2.106)$$

III the third one is called pitch over recovery, in which the pitch is maintained constant to allow the alignment between the velocity vector and the LV axis, indeed this sub-phase ends when the angle of attack is equal to zero;

$$\vartheta(t) = \vartheta_{po} \quad (2.107)$$

IV the fourth one is the zero-lift gravity turn, which is called in this way because the pitch angle is kept constantly equal to the flight path angle, thus the angle of attack is null and consequently the lift is equal to zero. The direction of the thrust and the velocity vector coincides and the rotation of the LV axis towards the local horizon is produced by the gravity.

$$\vartheta(t) = \gamma_r(t) \quad (2.108)$$

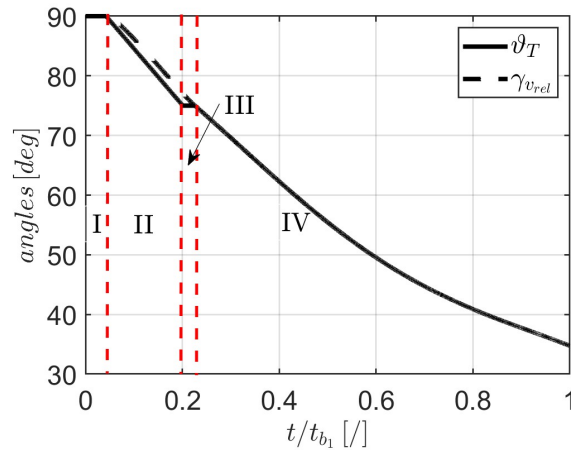


Figure 2.16: Phases of first stage maneuver.

The maneuver of gravity turn is not efficient from an energetic point of view, because it presents a high value of gravity losses, however it must be performed during first stage flight due to the presence of the atmosphere and the occurrence of maximum dynamic pressure q_{max} . Usually the first stage burn out happens in quasi-vacuum conditions, thus for the upper stage flight the steering strategy is different. The one adopted in this thesis is the bi-linear tangent steering (blt), the equation of the commanded pitch is:

$$\vartheta = \arctan \frac{k^\xi \tan \vartheta_i + (\tan \vartheta_f - k^\xi \tan \vartheta_i) \tau}{k^\xi + (1 - k^\xi) \tau} \quad (2.109)$$

where ϑ_i and ϑ_f are respectively the initial and final values of the pitch during the maneuver, k is a constant equal to 100, $\tau = (t - t_i)/(t_f - t_i)$ is an adimensional time and the parameter ξ , which varies between -1 and 0 , determines the shape of the pitch control curve, as shown in Fig. 2.17.

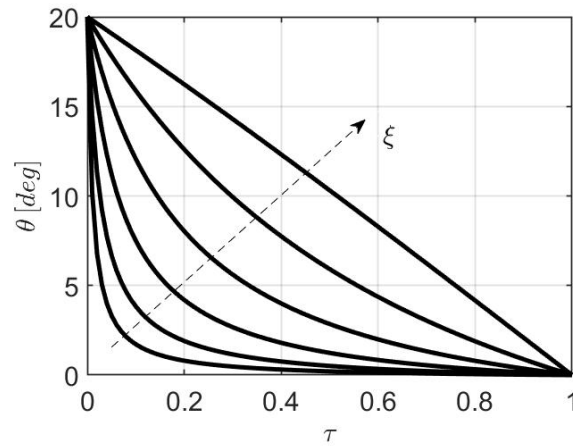


Figure 2.17: Bi-Linear tangent steering law.

In order to place the satellite into the target orbit, during the ascent, the launch vehicle must be placed in an elliptical transfer orbit. This occurs by providing a first velocity increment Δv_1 given by Eq. (2.110).

$$\Delta v_1 = \sqrt{\frac{\mu_\oplus}{r_1}} \left(\sqrt{\frac{2r_2}{r_1 + r_2}} - 1 \right) \quad (2.110)$$

Then at the end of the transfer orbit it is necessary a second velocity increment to circularize the orbit (see Eq. (2.111)).

$$\Delta v_2 = \sqrt{\frac{\mu_\oplus}{r_2}} \left(1 - \sqrt{\frac{2r_1}{r_1 + r_2}} \right) \quad (2.111)$$

This strategy involving two velocity increment is called Homann transfer orbit and the required total velocity is the sum of Δv_1 and Δv_2 . However, for some mission, the amount of velocity increment Δv_2 is provided by the payload and not by the launch vehicle.

Fairing jettisoning

Having a proper guidance law is especially beneficial to determine the correct time of fairing jettisoning. The fairing external temperature rises due to the aero-thermal heat flux \dot{q} , which is the

flow of energy per unit area per unit time, depending on the product between dynamic pressure and relative speed, as indicated in Eq. 2.112.

$$\dot{q} = q v = \frac{1}{2} \rho v^3 \quad (2.112)$$

This equation, as indicated in Ref. [7], is valid outside the continuous flow regime, i.e. when the Knudsen number K_n is greater than 10^{-2} . This number is defined as the ratio between the mean free path λ and the representative physical length L , it can be expressed in function of specific heat ratio γ , Mach M and Reynolds number R_e .

$$K_n = \frac{\lambda}{L} = \sqrt{\frac{\gamma \pi}{2}} \frac{M}{R_e} \quad (2.113)$$

The aero-thermal heat flux reaches a peak and then declines as the rise of relative speed is countered by the decrease of air density. The fairing can be safely jettisoned when \dot{q} falls below a certain level, indicating no more danger for the payload. Indeed, fairing separation can occur when the aerothermal heat flux is below the threshold of 1035 W/m^2 .

Falling points

To evaluate the falling points of the empty stages, the EoMs (2.102) have been used imposing both zero trust and mass flow rate and assuming $C_D = 0.5$. The state vector at stage separation has been taken as initial condition. The point of fallout represents a very dimensional constraint on the entire mission. In fact, empty stages and fairing must fall in desert areas or outside the territorial waters at a distance from the coast of minimum 12 mi (19.3 km) as indicated in Ref. [95].

2.7 Structural Model Generator

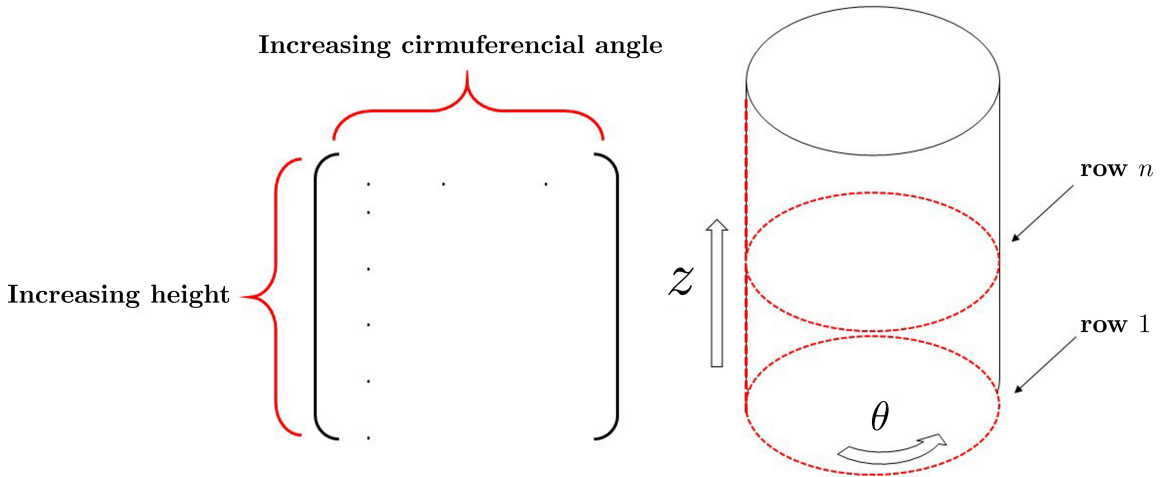
After the trajectory analysis, all the loads acting on the LV are known, thus the sixth phase of the design process is the structural analysis. In order to study thousands of LV configuration it is necessary to have finite element model generator which creates the input file to run the structural analysis in NASTRAN®. To analyze the entire mission from lift-off up to orbit insertion an essential point is being able to modify the geometry of the structure and coherently define the different loads acting on each component during every flight phase. Indeed, the finite element model is modular, that is, each part of the vehicle (stages, interstages, fairing and payload adapter) presents its own mesh, which is automatically generated depending on the design parameters. The overall structure is mainly described by means of plate elements whereas stringers, ordinates and polar bosses are modeled by means of beam elements. Solid elements are used to create the grain propellant and finally, nozzles, igniters, RR, LRE combustion chamber and payload are modeled as concentrated masses. The interface between contiguous parts with different meshes has been realized through glue elements. The considered materials are listed in Tab. 2.8. Carbon Fiber Reinforced Polymer (CFRP) is used for the solid rocket motor cases and payload adapter while aluminium alloy A7075 T6 is utilized for all the others LV components. The choice of only these two materials is dictated by the fact that these are the two main materials of the European launch vehicles studied in this thesis.

Table 2.8: Materials properties (Ref. [5]).

Material	Density [kg/m^3]	Young's module [GPa]	Ultimate tensile stress [MPa]
A7075 T6	2810	72	570
CFRP	1600	70	810

2.7.1 FE model geometry

The first step to generate the geometry is to define a reference frame, in this thesis the z axis coincides with the LV axis, while x and y lie in the plane orthogonal to z ; the origin of this reference frame is placed at the bottom of the LV. To render this process automatic, the LV geometry is divided in three main modules: stage, inter-stage and upper composite. For each module are defined three kind of matrices relative to geometric grid, nodes and elements. Indeed, every element is defined by the nodes surrounding it and every node is determined by its coordinates x, y, z . For each component, these coordinates are respectively contained in the geometric matrices X, Y, Z . The matrix of the nodes ND_{ID} , which contains the node identification number is built knowing the dimensions of the geometric matrices, according to the structure shown in Fig. 2.18. With a similar logic is created also the matrix EL_{ID} , which collects the identification number of the elements. Once defined these two matrices, it is possible to link the nodes to the elements, through the element nodes matrix EL_{ND} , that is a three dimensional matrix. For instance, for a plate element, this matrix is built following the structure displayed in Fig. 2.19, it is composed by 4 layers, each of which is in turn a part of the ND_{ID} matrix.

**Figure 2.18:** Structure of nodes ID matrix.

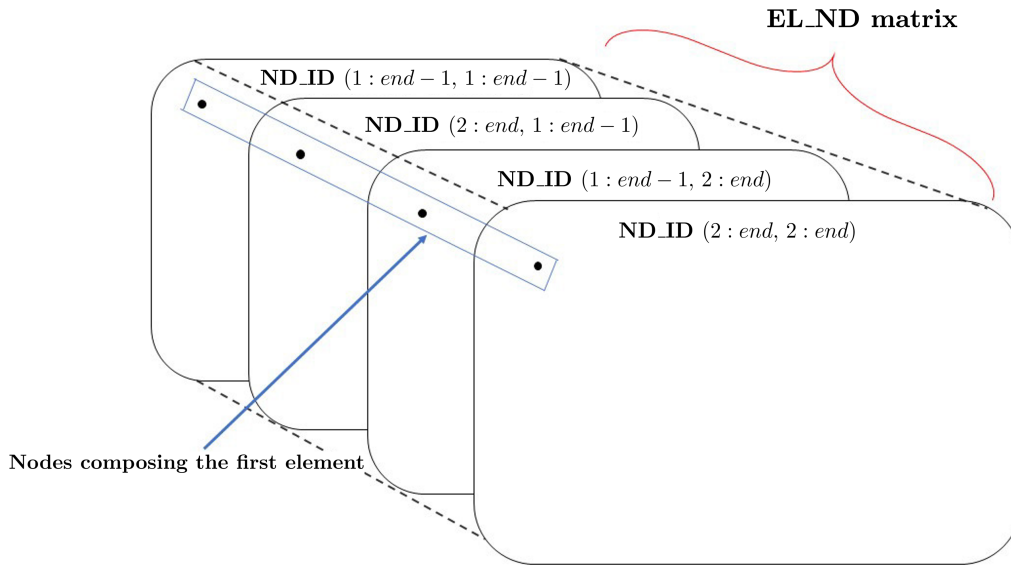


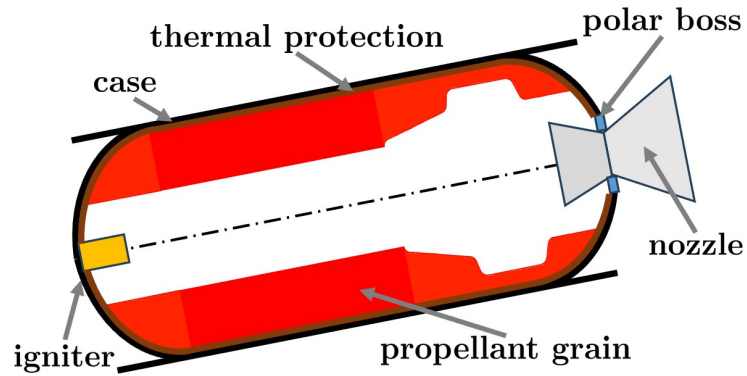
Figure 2.19: Structure of a plate element nodes matrix.

Solid rocket motor stage

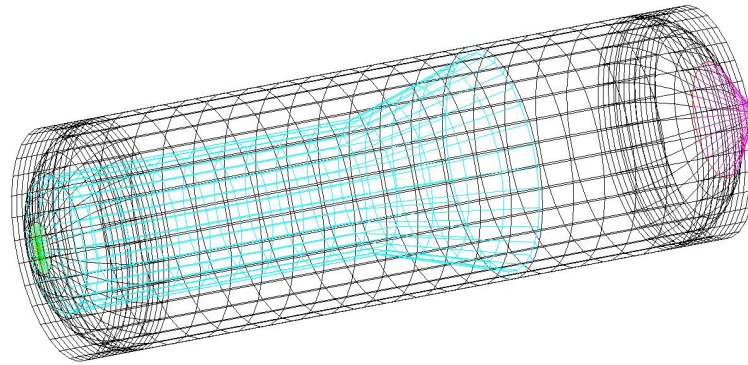
As discussed in Sec. 2.4, geometrically the solid rocket motor case is formed by a cylindrical part, two hemispherical domes and two cylindrical skirts. The mesh discretization is displayed in Fig. 2.20(b). All the external structure is made by *CQUAD4* (planar quadrilateral plate elements) except the closure of the upper dome, which is modeled with *CTRIA3* (planar triangular plate elements). Instead, the solid propellant grain is made by *CHEXA* (3D hexagonal elements), this modeling was chosen because the solid propellant contributes to structural stiffness. The shape of the propellant grain is simplified by a cylindrical zone and a truncated cone zone, due to the complexity of the real 3D star shape. The upper dome is closed, while the lower dome is open and it is reinforced by the polar boss, modeled as a ring torus made by *CBAR* (1D axial element). The igniter and the nozzle (along with TVC) are modeled as a concentrated masses; the igniter is placed on the central node of the upper dome, while the nozzle is placed on a dedicated node under the lower dome and it is linked to the polar boss through *RBE3* rigid connection.

Liquid rocket engine stage

Liquid rocket engines stage is composed by four main components: oxidizer and fuel tanks, intertank and combustion chamber. Liquid tanks present the same shape as the solid rocket case (a cylinder with two domes, which are both closed). There are two types of tanks configuration: separated or common bulckhead. As it can be seen in Fig. 2.21, the first configuration involves the presence of an intertank to ensure proper separation between the two. Instead, as displayed in Fig. 2.22 in the second configuration one dome is in common (the upper dome of the lower tank is also the lower dome of the upper tank). Unlike solid engine cases, liquid engine tanks have internal pressures an order of magnitude lower, so they are components more prone to buckling and require reinforcements to increase bending stiffness. For this reason, stringers have been modeled that can



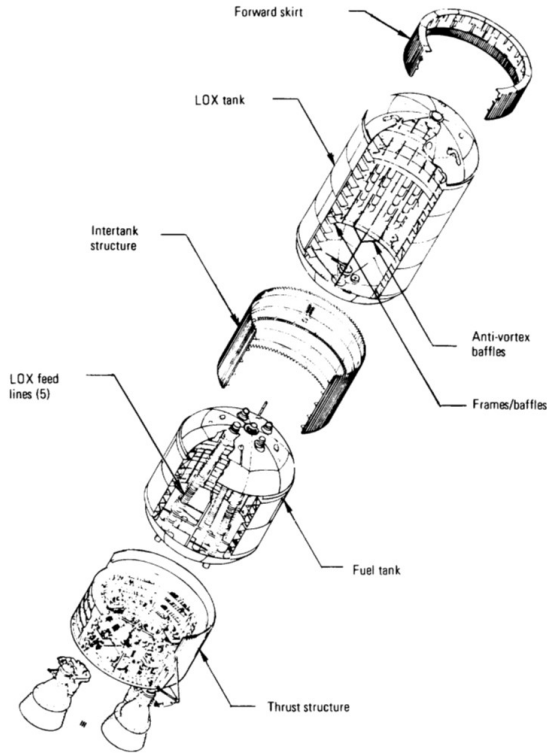
(a) SRM schematic



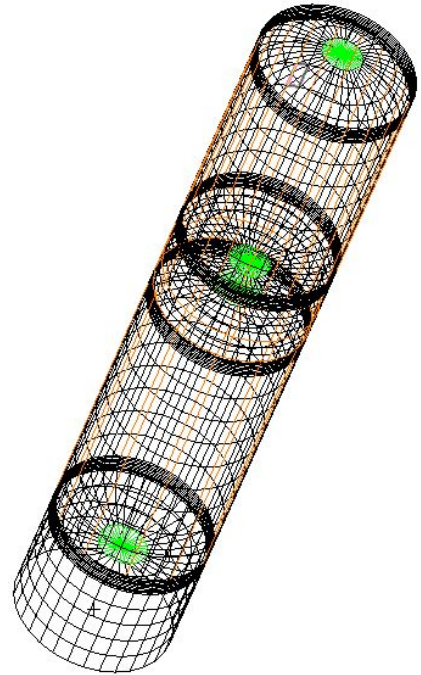
(b) SRM mesh

Figure 2.20: Comparison between SRM schematic and mesh.

vary in number, shape and size. As for the other components of LRE, the combustion chamber and nozzle are modeled as masses concentrated in a node connected to the lower skirt by rigid contacts. The liquid propellant inside the tanks is distributed along the axis of the tank with a number of points equal to its axial mesh discretization, as shown in Fig. 2.23. This choice allows for better modeling of both tank emptying depending on the phase of flight and propellant sloshing with equivalent mechanical models.

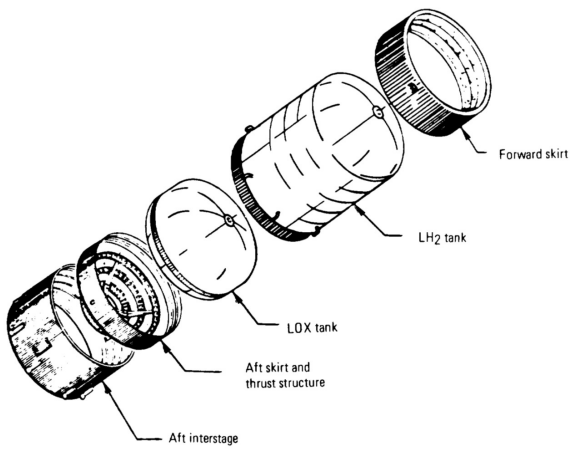


(a) Scheme of LRE separated tanks

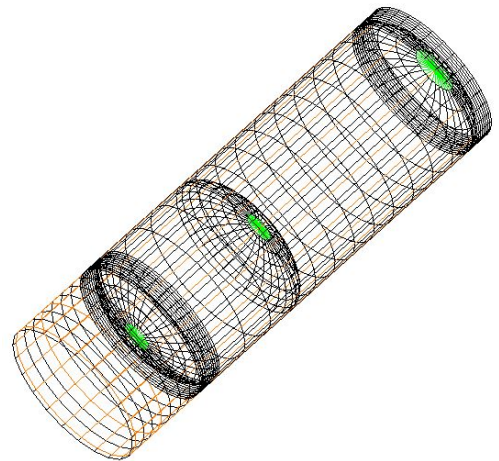


(b) LRE separated tanks mesh

Figure 2.21: Comparison between LRE separated tanks scheme (Ref. [96]) and mesh.



(a) Scheme of LRE common bulkhead tanks



(b) LRE common bulkhead tanks mesh

Figure 2.22: Comparison between LRE common bulkhead tanks scheme (Ref. [96]) and mesh.

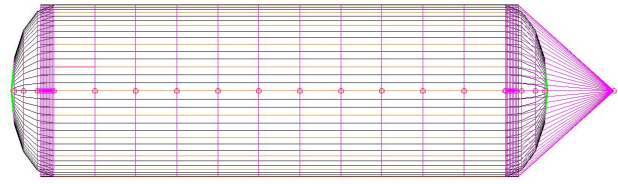


Figure 2.23: Liquid propellant modeling.

Interstage

The IS is characterized as a cylindrical or truncated conical shell (shown in Fig. 2.24(a)) respectively if the two consecutive stages present the same or a different diameter. The IS height depends on the length of the upper stage nozzle, and the avionics and the retro-rockets (if any) used for the first stage separation are contained inside. The main structure of the inter-stage is composed by shell elements, whereas, stringers and formers by beam elements. Avionics and possible retro-rockets are modeled as concentrated masses (see Fig. 2.24(b)). The number, size and thickness of stringers and formers are considered as design parameters and can be assigned by the user. More in detail, the shape can be circular, squared, “T” shaped and “H” shaped, as displayed in Fig. 2.25.

Upper composite module

The upper composite module which is divided in equipment bay, fairing, payload adapter and payload. The equipment bay is a cylindrical shell containing the on-board computer and, depending on the configuration, either the AOCS or a small liquid rocket engine. On the other hand, the fairing is the casing that protects the payload from aero-thermal loads. Its geometry (see Fig. 2.26(a)) is inspired by the VEGA fairing and is divided in four sections: truncated cone, cylinder, fillet and nose. The payload adapter is a conical structure with the payload on top modeled as a concentrated mass and connected through *RBE3* entries to the upper surface of the payload adapter which is reinforced with a circular former modeled through beam elements.

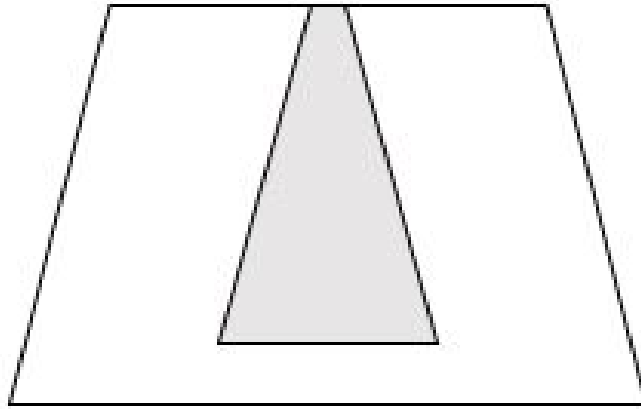
2.7.2 FE model loads and load-cases

The forces acting on the launch vehicle are divided in: internal pressure, thrust, gravity, aerodynamic and inertial forces. During the flight, especially in the atmospheric phase, these loads compress the structure and generate bending moment, thus every element can experience a failure due to maximum stress overcome or to buckling.

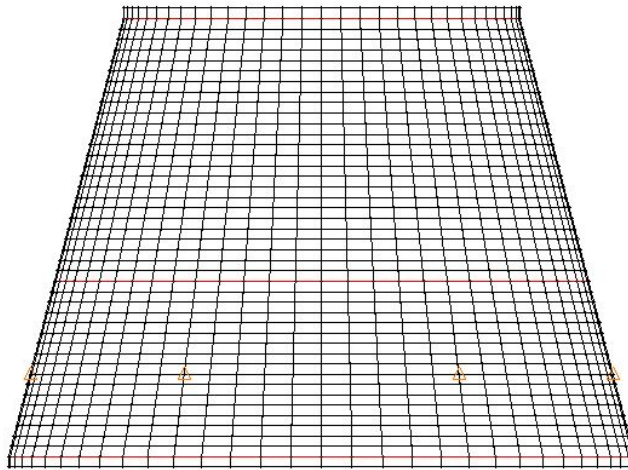
Pressure

The pressurized components of the LV are liquid propellant tanks and solid rocket motor case. Liquid propellant tanks are pressurized with an inert gas (normally helium) which acts on both the liquid free surface and the tank walls. Thus, the pressure is modeled as a load *PLOAD*: this NASTRAN© entry applies a pressure on every element of the tank (cylinder and domes). Due to the small size of the liquid tanks considered in Sec. 3.3 the effect of hydrostatic pressure in the tanks was neglected.

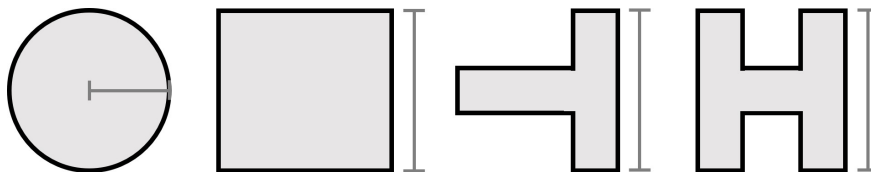
SRM case is is pressurized due to the combustion gasses that fill the empty part of the chamber and push on the grain surface (which is simplified as the combination of a cylindrical and a truncated



(a) Scheme of inter-stage



(b) Inter-stage mesh

Figure 2.24: Comparison between inter-stage scheme and mesh.**Figure 2.25:** Stringers types.

conical part), thus providing the influence of stress of the tank walls on the shape of the grain. Therefore, also for this component the chamber pressure p_c is modeled as a pressure load *PLoad*. However, since the lower dome of the tank is open, the overall pressure results in a force in the axial direction that must be compensated by subtracting it to the thrust. The amount of this resulting force is given by:

$$F_p = p_c A_{hole} \quad (2.114)$$

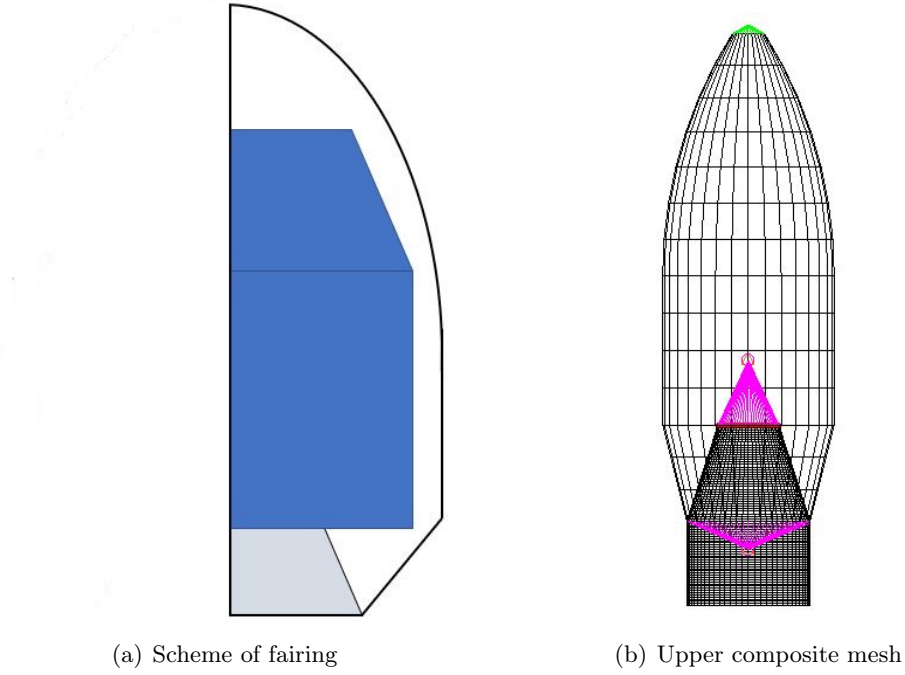


Figure 2.26: Comparison between upper composite scheme and mesh.

where A_{hole} is the effective area of the tank opening which is a polygon with a number of sides n_s equal to the number of circular nodes -1 :

$$A_{hole} = \cos^2\left(\frac{\pi}{n_s}\right) n_s \tan\left(\frac{\pi}{n_s}\right) \quad (2.115)$$

Thrust

The NASTRAN[®] command for defining the thrust is the *FORCE* command, which requires to identify a node in which the force is applied, a value for the force magnitude and a direction which is taken considering the nozzle deflection angle δ_{TVC} . The thrust is applied on the node where is concentrated the mass of the nozzle, this node is linked through rigid contacts to the polar boss of the SRM case or to the LRE thrust skirt. The thrust T expressed in the FE body reference frame is:

$$\begin{aligned} T_x &= -T \sin \delta_{TVC} \\ T_y &= 0 \\ T_z &= T \cos \delta_{TVC} \end{aligned} \quad (2.116)$$

The thrust angle δ_{TVC} is calculated by imposing the balance between the aerodynamic torque and the one generated by the side thrust, as described in the following equation:

$$T \sin \delta_{TVC} Z_{CoG} = F_{lat} (Z_{CoP} - Z_{CoG}) \quad (2.117)$$

where F_{lat} is the lateral aerodynamic force concentrated in the center of pressure placed in Z_{CoP} and Z_{CoG} is the position of the center of gravity.

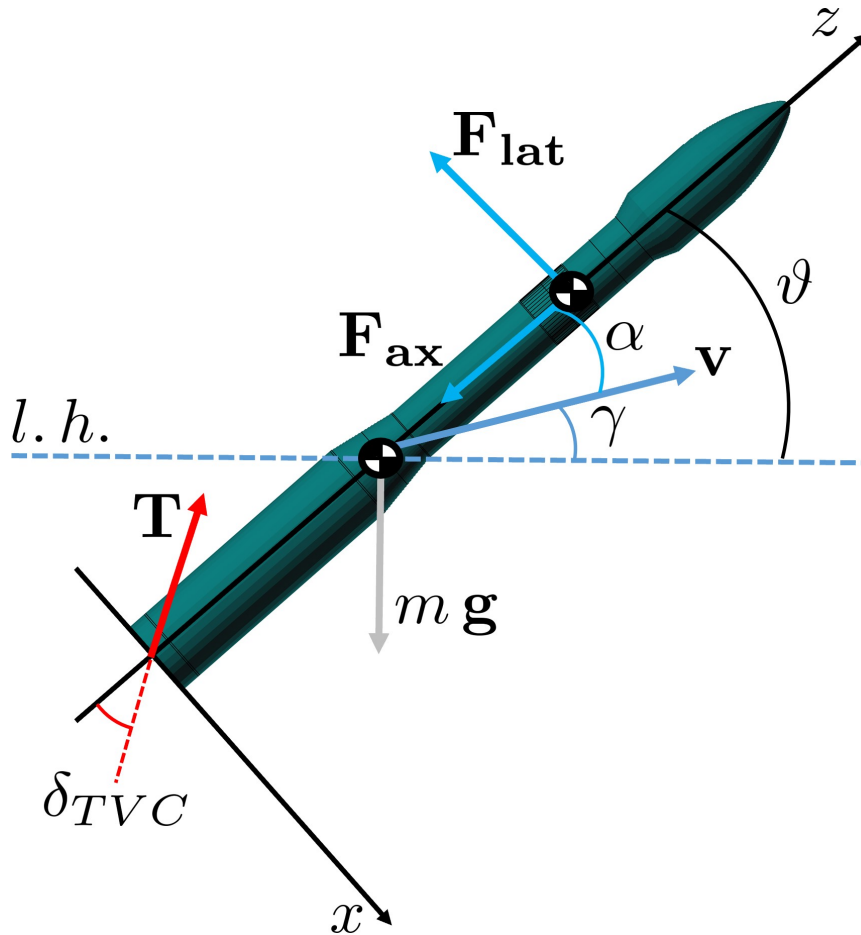


Figure 2.27: External forces acting on LV.

Gravity & inertial forces

With the 3DoF trajectory model, gravity is applied at the center of mass (see Fig. 2.27); in a FEM analysis however, it can be easily accounted for by the NASTRAN© entry *GRAV* which applies a pitch-angle-dependent gravitational acceleration to each element of the structure as it follows according to the body reference frame:

$$\begin{aligned} g_x &= g \cos \vartheta \\ g_y &= 0 \\ g_z &= g \sin \vartheta \end{aligned} \quad (2.118)$$

Inertial forces are loads generated by the acceleration, the component more subjected to them is the lower stage, as it is compressed by the mass above. These loads have been modeled through the NASTRAN© command *inertial relief*, which allow to perform a static analysis of a free structure. Indeed, normally, static analysis requires the body to be constrained, otherwise not solvable singularities would arise inside the stiffness matrix. Thank to the inertial relief, on every nodes of the structure a proper acceleration is applied to balance the external loads creating a static equilibrium. The inertial relief works by inserting the command *PARAM, INREL* in the NASTRAN© input file. Besides, it must be defined a *SUPPORT* node, that represents an ideal fixed point as reference to calculate the inertial forces.

Aerodynamic forces

The aerodynamic forces, lift and drag, can be projected in the axial and lateral direction, creating the loads distribution F_{ax} and F_{lat} described by Eqs. (2.89) and (2.90). Firstly, these continuous distribution are transformed in concentrated loads, then they are applied on the nodes of a central bar, which are rigidly connected to the nodes of the external surface. The implementation of the lateral force, along with the central bar is displayed in Fig. 2.28. The process of distributing the load per unit length on the nodes results in higher values on the nodes of the components with a poorer discretization, and lower values on the nodes of the parts with a richer discretization.

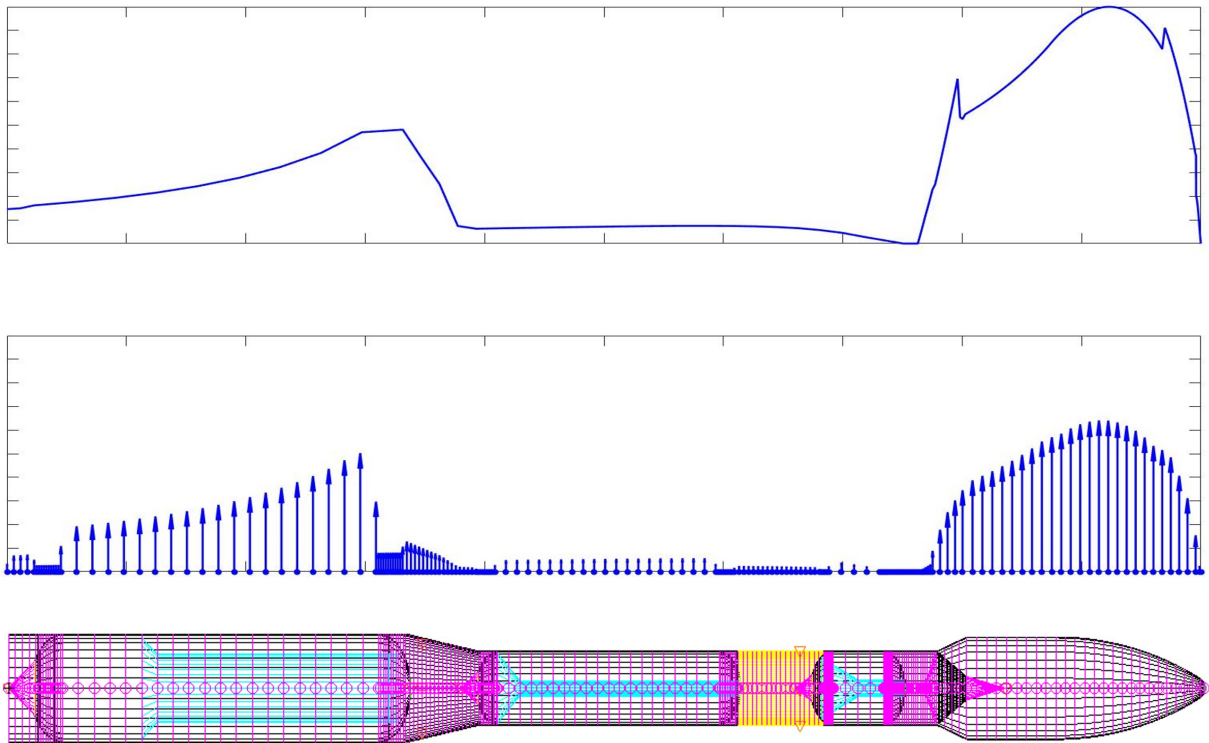


Figure 2.28: Lateral force distribution implementation.

Load cases

In the broader sense, during the mission of a LV the external loads as well as the vehicle attitude and its mass and structural configuration vary. Studying the structural behavior in each phase of the mission profile would result in an excessive computational cost. Hence, only a limited number of load cases are specified to encompass the most crucial flight conditions affecting the structural integrity. In greater detail, the structural arrangement of the rocket in the five load cases, which are taken into account for sizing the structure to withstand the entire mission, is depicted in Figure 2.29 and enumerated as follows:

[L1]: first stage maximum thrust F_{max} ;

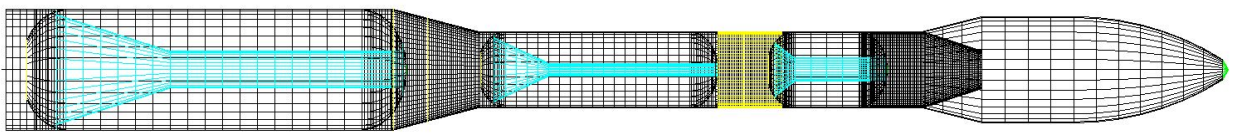
[L2]: first stage maximum dynamic pressure q_{max} (taking into account the effect of the wind in L2 is verified also $q \alpha_{max}$);

[L3]: first stage maximum acceleration ac_{max} ;

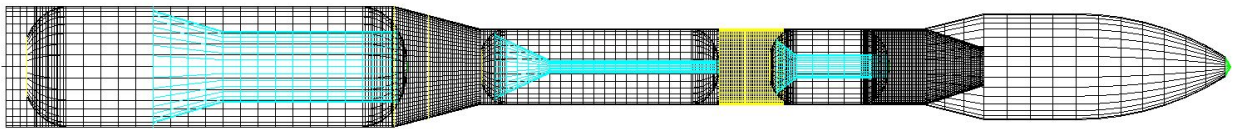
[L4]: second stage maximum acceleration;

[L5]: third stage maximum acceleration.

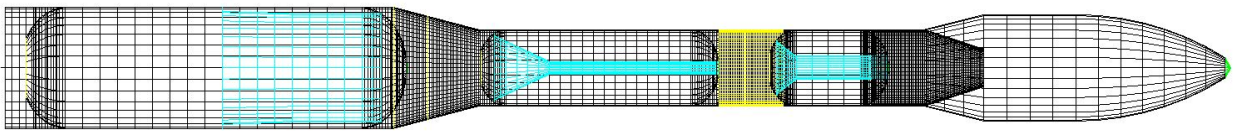
The significant benefit of being able to analyze the performance of the Launch Vehicle (LV) across various flight phases lies in the capability to conduct comprehensive sizing. This results in an overall structure, ensuring that individual components can withstand the loads encountered throughout the entire ascent mission. However, in this work, it is noticed that the size of all the LV components, except for the polar bosses of the 2nd and 3rd stages, are determined by the load case of q_{max} . Therefore, the optimization procedure as well as the results that are shown in Chpt. 3 are obtained considering only the load case L2.



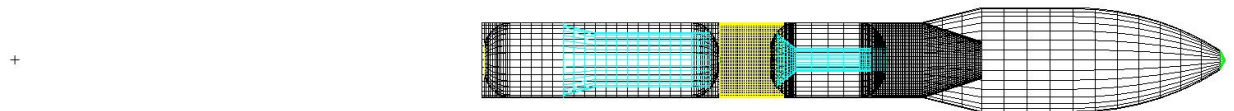
(a) L1 First stage maximum thrust



(b) L2 First stage maximum dynamic pressure



(c) L3 First stage maximum acceleration



(d) L4 Second stage maximum acceleration



(e) L5 Third stage maximum acceleration

Figure 2.29: Load cases.

2.7.3 Static analysis

The linear static analysis on the structure is performed by the solver *sol101*. Once a specific set of loads has been defined, the static analysis will assess the displacements and stresses on each element

of the structure caused by that load environment. These stress values are highly relevant because if any of them were to exceed the maximum allowable stress of the material, the element would be considered broken. Since plate elements are not subject to one-dimensional stresses, failure criteria must be used to consider an equivalent stress when studying material breakage. Thus for plate elements the adopted criterion is the Von Mises's one. Instead, for one dimensional elements it is considered the axial stress.

$$\frac{\sigma}{\sigma_{UTS}} \leq FoS \quad (2.119)$$

Eq. (2.119) states that the ratio between the stress and the ultimate tensile stress must be equal or less than the chosen Factor of Safety (FoS).

2.7.4 Buckling analysis

The linear buckling analysis is carried out by the solver *sol105*. The components more subjected to buckling failure are the not pressurized ones, such as interstage and low pressurized ones, as the LRE tanks. On the other hand SRM cases are less prone to buckling failure due to their high internal pressure. The output of the buckling analysis is a set of eigenvalues, which are the critical buckling multipliers. The product between these multipliers and the static load produces zero poles in the finite element dynamic equation. Each eigenvalue is associated the corresponding eigenvector that represents the buckling mode shape. These mode shapes are wavy, in fact the shell surface presents the typical folds caused by the buckling. The main issue of this kind of analysis is that the number of the folds depends by the mesh discretization, influencing the value of the buckling load multiplier. In particular a low mesh discretization implies a higher eigenvalue as if the structure is more rigid and resistant to buckling. On the other hand a high mesh discretization entails high computational time. Therefore, for every component has been performed a mesh sensitivity analysis in order to find the minimum number of nodes for which the buckling load multiplier remains unchanged.

2.8 Surrogate FE model

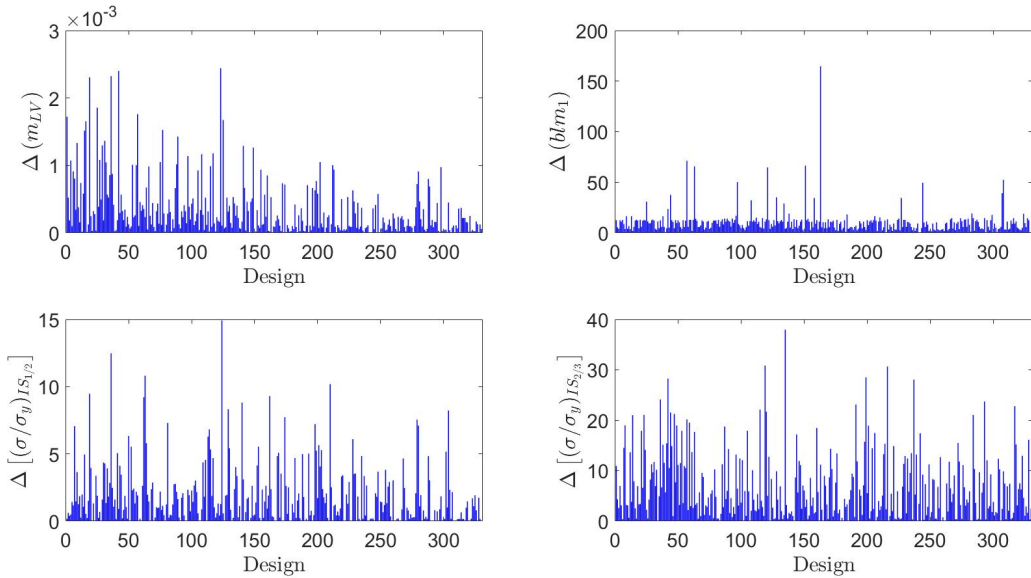
In order to reduce the computational time a surrogate FE model has been created using the Response Surface Models (RSM) or metamodels. The RSM exploited in this thesis are Radial Basis Functions (RBF) and Gradient Boosting Machine (GMB), which are described in App. B The steps are the following:

1. create a database of input-output generated by the real FE model with uniform Latin hypercube (ULH) sampling;
2. perform a sensitivity analysis to discover how much each output is influenced by the input design variables;
3. split the design in the database in 66 % for training and 33 % for validation;
4. train the RSM with an internal optimization process to find the best coefficients and polynomial types that fit the real values;
5. verify the residuals between real and virtual values trough the validation table.

Table 2.9: RBF residuals summary for q_{max} load case.

Output	Symbol	Function type	Mean Rel. err, %	Regression
Static/Ultimate stress PB SRM 1	$(\sigma/\sigma_U)_{PB_{SRM1}}$	MQ	$1.99 \cdot 10^{-3}$	1.0
Static/Ultimate stress IS 1/2	$(\sigma/\sigma_U)_{IS_{1/2}}$	PS	1.836	0.982
Static/Ultimate stress formers IS 1/2	$(\sigma/\sigma_U)_{FIS_{1/2}}$	MQ	3.19	0.972
Static/Ultimate stress IS 2/3	$(\sigma/\sigma_U)_{IS_{2/3}}$	PS	6.640	0.917
Static/Ultimate stress stringers IS 2/3	$(\sigma/\sigma_U)_{SIS_{2/3}}$	MQ	8.472	0.879
Static/Ultimate stress EQB	$(\sigma/\sigma_U)_{IS_{3/4}}$	MQ	4.780	0.966
Static/Ultimate stress PLA	$(\sigma/\sigma_U)_{PLA}$	MQ	3.376	0.961
1 st Buckling load multiplier	blm_1	MQ	2.631	0.989
LV mass	m_{LV}	G	$3.38 \cdot 10^{-4}$	1.0

Two metamodels have been created: one based on RBF and another based on GBM, depending on the number of design variables. For the application case of Sec. 3.1, it has been created a database input/output of 1000 samples, 667 for training and 333 for validation. So far, of the more than 90 FEM parameters featuring the LV finite element model generation, 11 are set as design variables (see Tab. 3.3). The outputs are the LV mass, the buckling load multiplier and the ratio between static and ultimate stress for each component. Although the interaction between input and output seems trivial, it is necessary to perform a sensitivity analysis; because, the static stress of each component is not determinate only by the its thickness, but also by the mass of the components above it. The comparison between real an surrogate model is shown through the Tab. 2.9, in which are reported the mean relative error and the regression values calculated on the designs of the validation table. The LV mass presents the best fitting with a mean relative error about of $5 \cdot 10^{-4}$ and a regression equal to 1. Instead, the static/ultimate stress of the stringers of the inter-stage 2/3 present the worst fitting, however with an error less than 10 %.

**Figure 2.30:** Main outputs residuals charts for RBF surrogate FEM.

For the application case of Sec. 3.2, the amount of design variables is higher (from 11 to 60), thus it has been necessary to switch the Response Surface model from RBF to GMB. The comparison between this metamodel and the real FEM are summarized in Tab. 2.10. The results are comparable with the ones obtained by the RBF metamodel. However, the values of regression of Tab. 2.10 are

less than those found in Tab. 2.9. This behavior is a consequence of increasing design variables and thus system complexity. In more detail, the major difference between the surrogate FE model on RBF and the one based on the GBM lies in the variability of external forces in the latter. In fact, in the RBF surrogate FE model, the design variables are purely geometric and the external forces are considered fixed.

Table 2.10: GMB residuals summary for q_{max} load case.

Output	Symbol	Mean Rel. err, %	Regression
Static/Ultimate stress PB SRM 1	$(\sigma/\sigma_U)_{PB_{SRM_1}}$	1.11	0.923
Static/Ultimate stress IS 1/2	$(\sigma/\sigma_U)_{IS_{1/2}}$	1.94	0.905
Static/Ultimate stress formers IS 1/2	$(\sigma/\sigma_U)_{FIS_{1/2}}$	8.33	0.649
Static/Ultimate stress IS 2/3	$(\sigma/\sigma_U)_{IS_{2/3}}$	1.99	0.956
Static/Ultimate stress stringers IS 2/3	$(\sigma/\sigma_U)_{SIS_{2/3}}$	2.82	0.898
Static/Ultimate stress EQB	$(\sigma/\sigma_U)_{EQB}$	1.23	0.879
Static/ULTimate stress PLA	$(\sigma/\sigma_U)_{PLA}$	1.70	0.824
1 st Buckling load multiplier	blm_1	2.32	0.936

Chapter 3

Application cases on different Launch Vehicle Configurations

This chapter presents the main studied test cases: a structural optimization of a VEGA inspired launch vehicle, a single and a multi-objective MDO of the VEGA inspired LV and a multi-objective MDO of a liquid based TSTO launch vehicle.

3.1 VEGA inspired structural optimization

The real VEGA launch vehicle has four stages: three based on solid rocket motor and one small LRE called Attitude and Vernier Upper Module (AVUM). The components of the this LV are: interstage 0/1, P80 SRM, interstage 1/2, Z23 SRM, interstage 2/3, Z9 SRM, interstage 3/4, AVUM, payload adapter and fairing. In order to validate both the real and surrogate FEM models, it has been performed a structural optimization on a VEGA inspired launch vehicle. It has been carried out on the platform ESTECO modeFRONTIER[®], utilizing the built in multi objective genetic algorithm MOGA-II. Considering the q_{max} load case, the cost function is the LV mass, and the constraints are the maximum static stress that each component can bear and the maximum allowable buckling load multiplier (blm).

$$J = m_0 \downarrow \quad (3.1)$$

Different Factors of Safety (FoS) can be considered for the analyses, in particular it has been taken $FoS = 1.5$. Thus the desired blm must be greater than 1.5 and the ratio between static and yield stress of each component must be lower than $1/1.5$. The values of the yield stress depends on the component materials (aluminum alloy for the inter-stages and equivalent isotropic carbon composite for the payload adapter and SRM cases). The flowchart of the optimization is displayed in Fig. 3.1: starting by a first guess of design variables, a Matlab[®] code generates the input file necessary to perform the structural analysis with NASTRAN[®]. The objective and constraints are extracted by the output file. The design variables are updated by modeFRONTIER[®] at each iteration in order to find the optimal design.

Both the objective function and the constraints can be evaluated using the real or the surrogate FE model. To compare the effects of adopting these two different models, three optimization cycles are performed varying the percentage of real and virtual design:

[C1]: 100 % Real FEM model

[C2]: 50 % Real 50 % Surrogate FEM model

[C3]: 100 % Surrogate FEM model

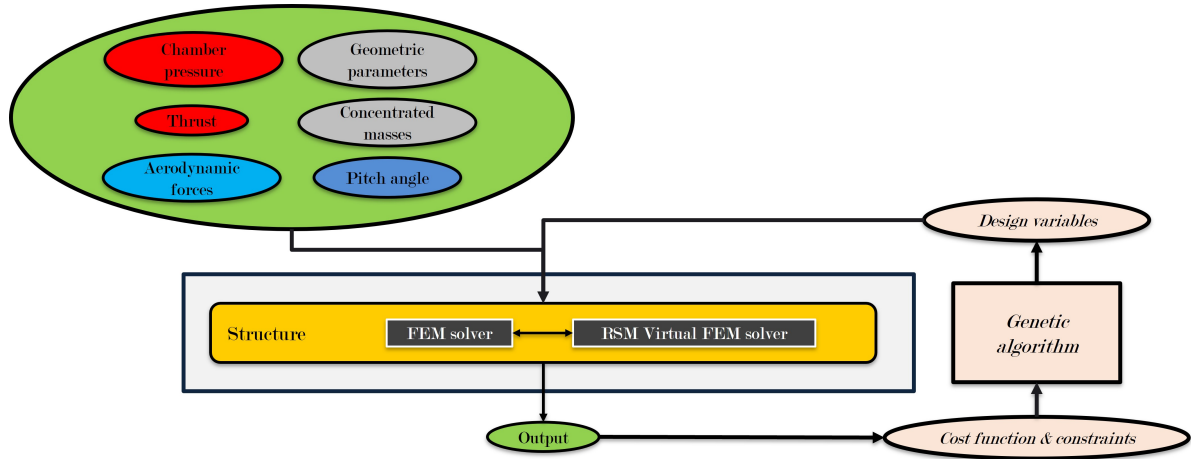


Figure 3.1: Structural optimization flowchart.

The results of the three optimization cycles are summarized in terms of design and output variables in Tabs. 3.1 and 3.2. In the first table is showed the comparison of the optimal design variables obtained at the end of each cycle. Some values, such as the thickness of inter-stage 1/2 remain unaltered, instead others change. For instance, for the cycle C2, the number of the stringers is lower, however their thickness is wider, in order to satisfy the constraints. In this analysis have been considered stringers with "H" shape and the design variable stringer thickness represents the length of the side of the "H". The SRM case thickness has not been taken as a design variable, since it depends only by the maximum expected operating pressure (MEOP) which has been assumed constant in this optimization. In the second table are displayed the outputs. C1 is the reference

Table 3.1: Comparison of optimal design variables for the three optimization cycles.

Design variables	Unit	C1	C2	C3
Polar boss 1 SRM 1 thickness	<i>mm</i>	55	55	55
Inter-stage 1/2 thickness	<i>mm</i>	5	5	5
Formers inter-stage 1/2 thickness	<i>mm</i>	1	5.1	7.2
Formers inter-stage 1/2 position w.r.t. h	/	0.4	0.5	0.6
Inter-stage 2/3 thickness	<i>mm</i>	3	3	3
Formers inter-stage 2/3 thickness	<i>mm</i>	11.4	5.1	5.1
Stringers inter-stage 2/3 number	/	35	23	33
Stringers inter-stage 2/3 thickness	<i>mm</i>	11.4	17.6	11.4
Inter-stage 3/4 thickness	<i>mm</i>	3	3	3
PLA thickness	<i>mm</i>	1	1	1
Former PLA thickness	<i>mm</i>	50	35	55

solution, because it is obtained using 100 % the NASTRAN© solvers. As the solutions C2 and C3 are evaluated utilizing the virtual finite element modeling, the outputs are verified through the real FEM (C2 ver. and C3 ver.). It emerged that the difference between real and virtual output is of

the same order predicted by the residuals analysis, except for IS 2/3 static stress of solution C3. As concerns the static analysis, it can be noticed that the diagram of the stress tensor is identical in the three cases (see Figs. 3.2(a), 3.2(c) and 3.2(e)). While, as regards the buckling analysis, it can be observed a difference between the first buckling modes of solution C1 and C3 (Figs. 3.2(b), 3.2(f)) solution C2 (Fig. 3.2(d)). All the cases present the buckling failure of inter-stage 2/3, more in detail, in C1 and C3 regards the external shell, whereas for solution C2 concerns the stringers. This could be explained by the lower number of stringers of solution C2.

Table 3.2: Comparison of optimal results of the three optimization cycles.

Objective & constraints	C1	C2			C3		
		C2 sur.	C2 ver.	$\Delta C2, \%$	C3 sur.	C3 ver.	$\Delta C3, \%$
m_{LV} at q_{max} , kg	90917	90915	90923	-0.0089	90915	90917	-0.0022
blm_1	1.5	1.5	1.49	0.671	1.52	1.45	4.83
$(\sigma/\sigma_y)_{PB_{SRM_1}}$	0.631	0.631	0.631	0	0.631	0.631	0
$(\sigma/\sigma_y)_{IS_{1/2}}$	0.614	0.606	0.606	0	0.594	0.594	0
$(\sigma/\sigma_y)_{FIS_{1/2}}$	0.372	0.366	0.367	-0.28	0.364	0.361	0.83
$(\sigma/\sigma_y)_{IS_{2/3}}$	0.327	0.252	0.280	-10.0	0.260	0.337	-22.8
$(\sigma/\sigma_y)_{SIS_{2/3}}$	0.256	0.247	0.250	1.2	0.258	0.258	0
$(\sigma/\sigma_y)_{EQB}$	0.347	0.340	0.347	-2.02	0.340	0.347	-2.02
$(\sigma/\sigma_y)_{PLA}$	0.102	0.087	0.079	10.12	0.087	0.080	8.75

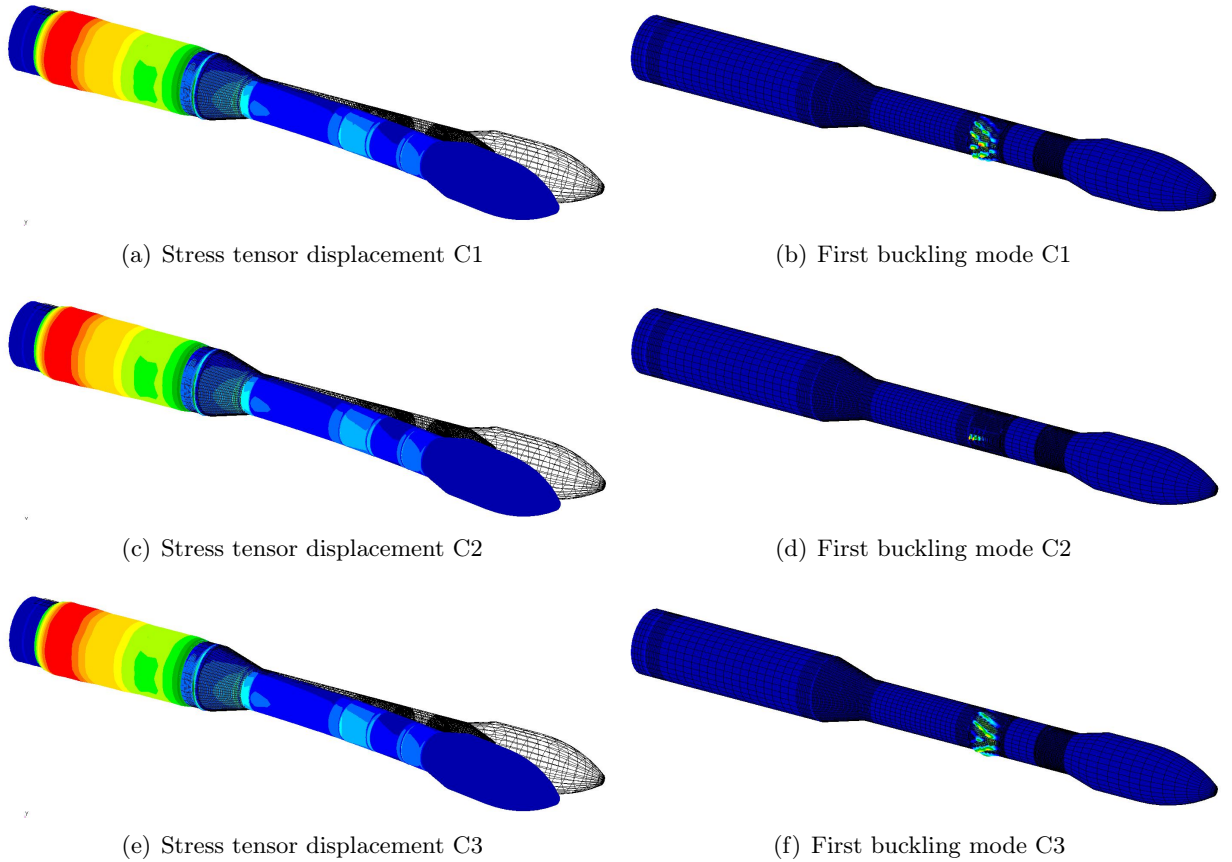
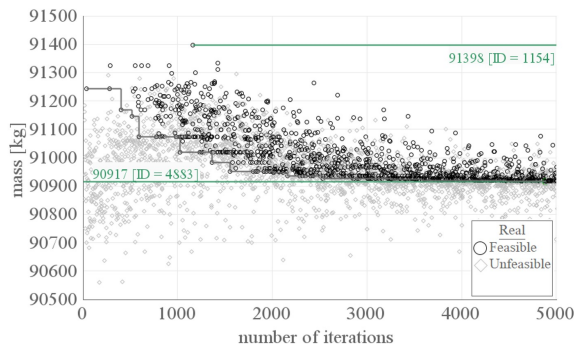


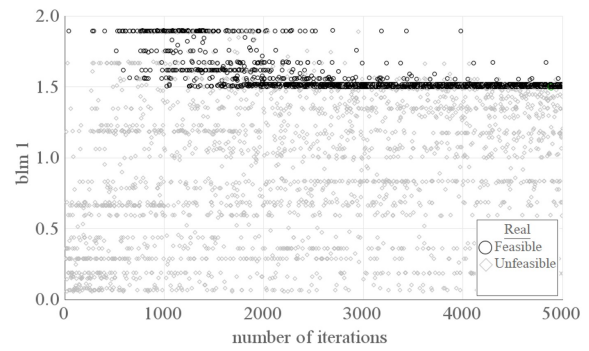
Figure 3.2: Static and buckling analysis after the three optimization cycles.

Instead, as the regards the convergence towards the optimum, that is displayed in Figs. 3.3(a),

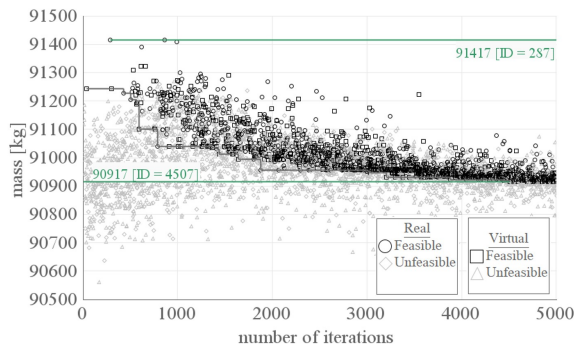
3.3(c), 3.3(e), the trend of the objective function along the iterations is very similar for all the three cycles. The black points are the feasible solutions, for which all the constraints are respected, while the gray ones the unfeasible solutions for which at least one constraint is not satisfied. The gray line represents the optimal feasible design along the iterations. The oscillations of the objective functions up and down this line is due to the action of genetic operators (cross over and mutation). Close to the final solution, the range of these oscillations is less thick and the gradient of the gray line is lower. In Figs. 3.3(b), 3.3(d), 3.3(f) is displayed the main constraint trend along the iterations and for every cycles can be notice a densification of the critical buckling load multiplier along its limit value.



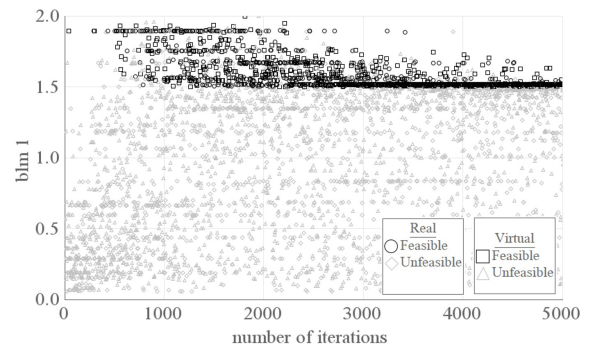
(a) LV mass at q_{max} C1



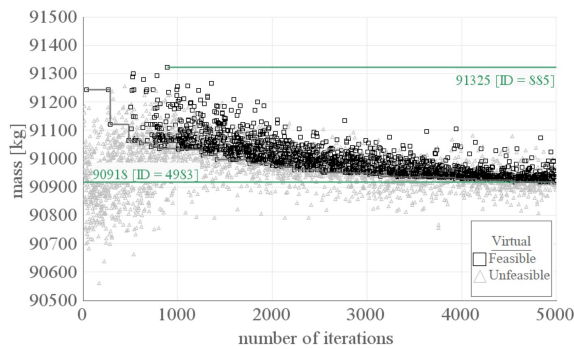
(b) blm_1 C1



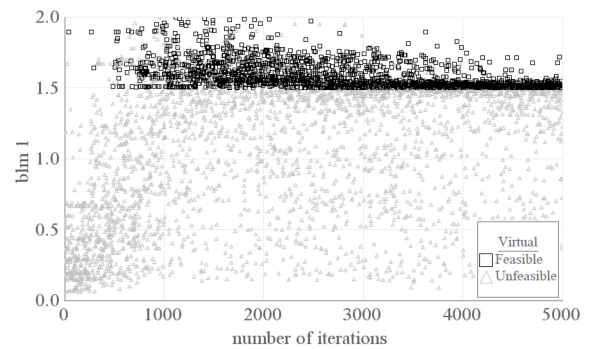
(c) LV mass at q_{max} C2



(d) blm_1 C2



(e) LV mass at q_{max} C3



(f) blm_1 C3

Figure 3.3: Objective function and main constraints trend for the three optimization cycles.

In Fig. 3.4 is shown the solution C1 for the other critical load cases. It can be noticed that

the most sizing load case is the one relative to q_{max} , as anticipated in Sec. 2.7. In fact, for all the other load cases the first blm is higher than the desired threshold of 1.5. For L1 and L3, the component more subjected to buckling is the inter-stage 1/2, while for L4 and L5 is the payload adapter. Moreover, it can be seen that, once the LV overcomes the denser layers of the atmosphere, there is no more lateral force and the buckling mode is axisymmetric. As regards the modal analysis, in Fig. 3.5 it is shown the first bending mode, both the shape and the frequency are a sign of the goodness of the model.

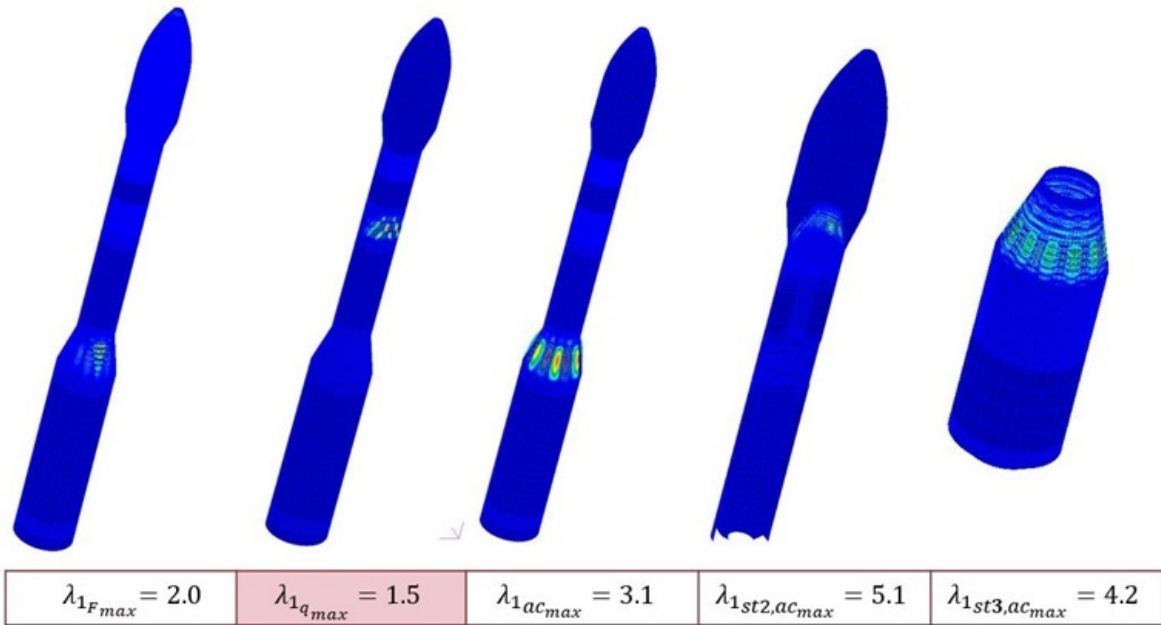


Figure 3.4: Buckling analysis in the five critical load cases at the end of C1.

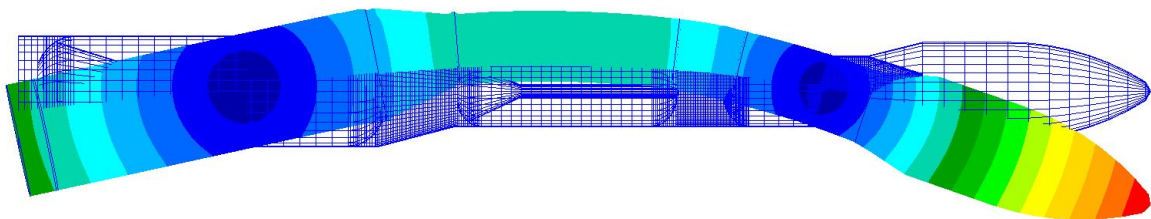


Figure 3.5: First bending mode at the end of C1.

3.2 VEGA inspired MDO

This section is dedicated to the multi-disciplinary design optimization of the VEGA inspired launch vehicle, analyzing in particular the analogies and the difference between single- and multi-objective MDO. For both these MDO cycles, the structural analysis has been performed by 50% by the real FEM solver and the other 50% by its surrogate.

3.2.1 Single-objective MDO

In order to test the MDO logic and architecture, the design of a VEGA inspired launch vehicle has been analyzed. Thus, once given the target orbit of the reference VEGA mission (700 km PEO as indicated in Ref. [97]), the optimizer finds the launch vehicle configuration with the maximum payload mass respecting all the mission constraints listed in Tab. 3.4. Some constraints, such as, maximum dynamic pressure and target orbital parameters are typical of every launch vehicle MDO; while the constraints on maximum GLOM and minimum payload mass are specific of this problem. In fact, to validate the procedure, the optimal design must have a GLOM less than or equal to the one of VEGA launch vehicle. The constraints of apogee and perigee altitude have a different threshold between global (genetic) and local (gradient based) refinement. The total number of input is 330 of which about 60 are design variables (see Tab. 3.3). The cost function J is expressed by Eq. (3.2), where m_{up} is the amount of mass of the last stage and m_{pAVUM} is the AVUM propellant including circularization, scattering, de-orbiting and unused).

$$J = m_{pl} \uparrow = (m_{up} - m_{pAVUM}) \uparrow \quad (3.2)$$

The algorithms utilized for the optimization are *MOGA-II* (Multi-objective Genetic Algorithm) for a first global search and then MIPSQP (Mixed Integer Programming Sequential Quadratic Programming) of ESTECO modeFRONTIER© (see Ref. [98]). The initial population (Design of Experiments) is composed by 1000 designs sampled with Uniform Latin Hypercube (ULH) scheme. Indeed, starting from a wide span of values, the cost function reached a maximum within 30 generations, as it can be observed in Fig. 3.6, which displays the history of the cost function along the iterations. Fig. 3.7, instead shows the relationship between the cost function and the main constraint (maximum GLOM). As expected, these two quantities are directly proportional and the feasible designs are under the threshold of 100, that represents the lift-off mass of the VEGA launch vehicle. As concerns the computation cost, the most expensive analysis is the structural one, thus to reduce the running time (which has been around 36 hours on 8 processors AMD© Ryzen 9 7950X CPU at 4.5 GHz), the FEM analysis is carried out only for the design that satisfied the main constraint and has a semi-major axis greater than 700 km. Practically, in this work, it is not useful to perform a FEM analysis for design that not respect basic requirements of the mission. Particularly, the FEM solver is not used when nozzle sizes exceed that of SRMs case diameters, when SRM L/D ratios are less than 1, and when the semi-axis of the target orbit is less than 700 km. In fact, in these cases there are errors on the geometry or flight loads.

Table 3.3: Design variables VEGA inspired SO.

Variable	Symbol	Range	Unit	Type	Class
Upper mass	m_{up}	[2350; 2450]	<i>kg</i>	continuous	mass
Percentage of velocity losses of SRMs	$\eta_{\Delta V}$	[15.5; 17.5]	%	continuous	energy
1 st stage diameter	D_{s1}	[2.5; 3.5]	<i>m</i>	continuous	structure
Upper stages diameter	D_{sup}	[1.5; 2.5]	<i>m</i>	continuous	structure
Tank flattening coeff.	$h_{d1,2,3}$	[0.55; 0.75]	/	continuous	structure
Interstage 1/2 thickness	t_{is12}	[2; 5]	<i>mm</i>	continuous	structure
Interstage 2/3 thickness	t_{is23}	[1; 5]	<i>mm</i>	continuous	structure
Interstage 2/3 stringers number	N_{str23}	[3; 71]	/	discrete	structure
Interstage 2/3 stringers dimension	r_{str23}	[1; 20]	<i>mm</i>	continuous	structure
Interstage 3/4 thickness	t_{is34}	[1; 5]	<i>mm</i>	continuous	structure
1 st stage throat diameter	D_{t1}	[470; 520]	<i>mm</i>	continuous	propulsion
2 nd stage throat diameter	D_{t2}	[260; 300]	<i>mm</i>	continuous	propulsion
3 rd stage throat diameter	D_{t3}	[140; 160]	<i>mm</i>	continuous	propulsion
1 st stage nozzle expansion ratio	$(Ae/At)_1$	[15; 25]	/	continuous	propulsion
2 nd stage nozzle expansion ratio	$(Ae/At)_2$	[20; 40]	/	continuous	propulsion
3 rd stage nozzle expansion ratio	$(Ae/At)_3$	[70; 110]	/	continuous	propulsion
SRMs web fraction	$wf_{1,2,3}$	[0.7; 0.8]	/	continuous	propulsion
1 st stage adimensional web points	Xw_{1n}	[/; /]	/	continuous	propulsion
1 st stage adimensional S_b points	YS_{b1n}	[/; /]	/	continuous	propulsion
4 th stage 1 st burning vs max t_b ratio	τ_{b41}/τ_{b4}	[0.45; 0.75]	/	continuous	propulsion
4 th stage 2 nd burning vs max t_b ratio	τ_{b42}/τ_{b4}	[0.05; 0.25]	/	continuous	propulsion
Azimuth	A_z	[-4; 0]	<i>deg</i>	continuous	trajectory
Pitch over angle	ϑ_{po}	[70; 80]	<i>deg</i>	continuous	trajectory
Pitch over time vs combustion t ratio	τ_{po}/τ_{b1}	[0.05; 0.2]	/	continuous	trajectory
Coasting time 1/2 vs ref. mission t ratio	τ_{c12}/τ_{ref}	[$\simeq 10^{-4}$; 10^{-3}]	/	continuous	trajectory
Coasting time 2/3 vs ref. mission t ratio	τ_{c23}/τ_{ref}	[$\simeq 10^{-4}$; 0.09]	/	continuous	trajectory
Coasting time 3/4 vs ref. mission t ratio	τ_{c34}/τ_{ref}	[$\simeq 10^{-3}$; 0.02]	/	continuous	trajectory
Coasting time 4/5 vs ref. mission t ratio	τ_{c45}/τ_{ref}	[0.3; 0.9]	/	continuous	trajectory
2 nd stage initial cmd angle	ϑ_{cmd2i}	[0; 40]	<i>deg</i>	continuous	trajectory
2 nd stage final cmd angle	ϑ_{cmd2f}	[0; 20]	<i>deg</i>	continuous	trajectory
2 nd stage bts coeff.	ξ_{bts2}	[-1; 0]	/	discrete	trajectory
3 rd stage initial cmd angle	ϑ_{cmd3i}	[-10; 10]	<i>deg</i>	continuous	trajectory
3 rd stage final cmd angle	ϑ_{cmd3f}	[-10; 10]	<i>deg</i>	continuous	trajectory
3 rd stage bts coeff.	ξ_{bts3}	[-1; 0]	/	discrete	trajectory
4 th stage 1 st burn initial cmd angle	ϑ_{cmd41i}	[-25; 25]	<i>deg</i>	continuous	trajectory
4 th stage 1 st burn final cmd angle	ϑ_{cmd41f}	[-25; 25]	<i>deg</i>	continuous	trajectory
4 th stage 1 st burn bts coeff.	ξ_{bts41}	[-1; 0]	/	discrete	trajectory
4 th stage 2 nd burn initial cmd angle	ϑ_{cmd42i}	[-5; 5]	<i>deg</i>	continuous	trajectory
4 th stage 2 nd burn final cmd angle	ϑ_{cmd42f}	[-5; 5]	<i>deg</i>	continuous	trajectory
4 th stage 2 nd burn bts coeff.	ξ_{bts42}	[-1; 0]	/	discrete	trajectory

Table 3.4: Constraints VEGA inspired.

Output parameter	Symbol	Limit	Unit	Type	Class
GLOM	m_0	$< m_{0_{VEGA}}$	kg	inequality	mass
Payload mass	m_{pl}	$> m_{pl_{VEGA}}$	kg	inequality	mass
Stage length vs diameter ratio	L/D	> 1	/	inequality	propulsion
Nozzle exit vs stage diameter ratio	D_e/D_s	< 0.95	/	inequality	propulsion
Nozzle exit vs separation p ratio	p_e/p_{sep}	> 1	/	inequality	propulsion
AVUM burning total time	$\tau_{b_{AVUM}}$	< 650	s	inequality	propulsion
Maximum dynamic pressure	q_{max}	< 60	kPa	inequality	trajectory
Angle of attack SRM endo-atm	$AoA_{endo_{max}}$	< 5	deg	inequality	trajectory
Angle of attack SRM exo-atm	$AoA_{exo_{max}}$	< 15	deg	inequality	trajectory
Product between q & AoA	$(q \cdot AoA)_{max}$	< 60	$kPa \cdot deg$	inequality	trajectory
q at 1 st stage separation	q_{sep}	< 1500	Pa	inequality	trajectory
Aero-thermal heat flux after F/S	\dot{q}_{max}	< 1135	W/m^2	inequality	trajectory
Pitch over angular rate	$\dot{\vartheta}_{po}$	< 2.5	deg/s	inequality	trajectory
Transfer orbit perigee	h_{ptr}	> 150	km	inequality	trajectory
3 rd stage falling point latitude	lat_{f_3}	$> 80 \ \& \ < 90$	deg	inequality	trajectory
Δ target orbit perigee	Δh_p	$< 7 \ \rightarrow \ < 0.7$	km	inequality	trajectory
Δ target orbit apogee	Δh_a	$< 70 \ \rightarrow \ < 0.7$	km	inequality	trajectory
Δ target orbit inclination	Δi_t	< 0.1	deg	inequality	trajectory
Acceleration induced to payload	a_c	< 50	m/s^2	inequality	structure
Buckling load multiplier at max $q \cdot \alpha$	blm	> 1.5	/	inequality	structure
Static stress vs ultimate static stress	σ/σ_{UTS}	< 0.8	/	inequality	structure

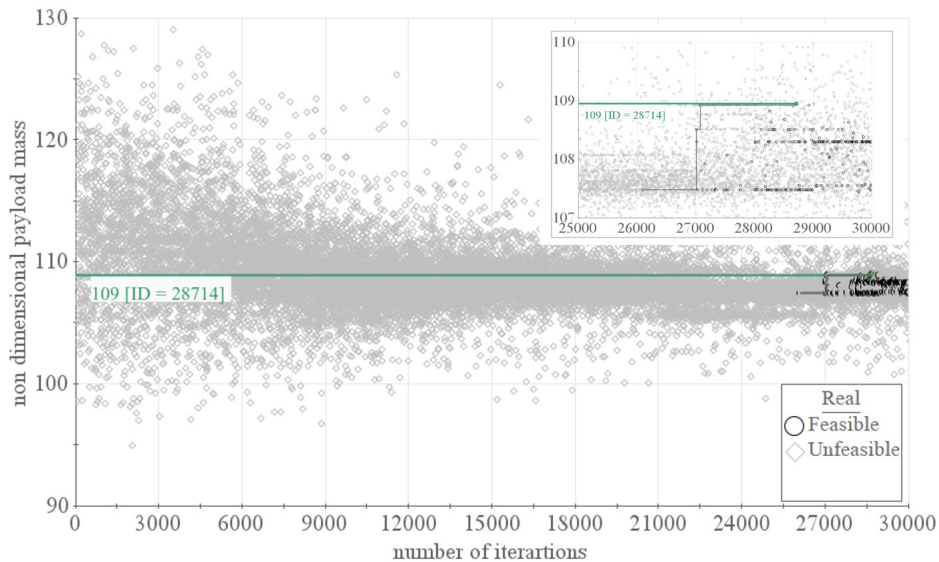


Figure 3.6: Cost function VEGA inspired SO.

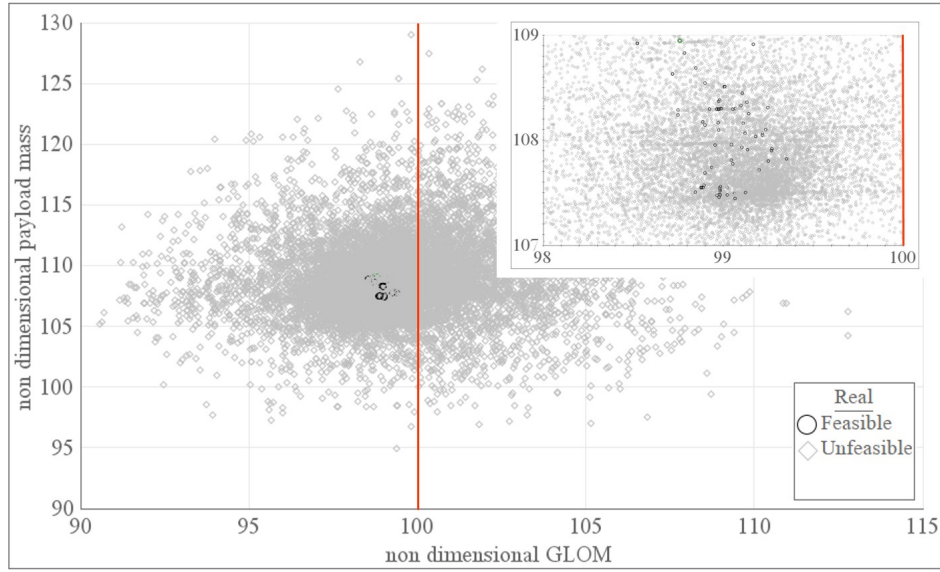


Figure 3.7: Main constraint VEGA inspired SO.

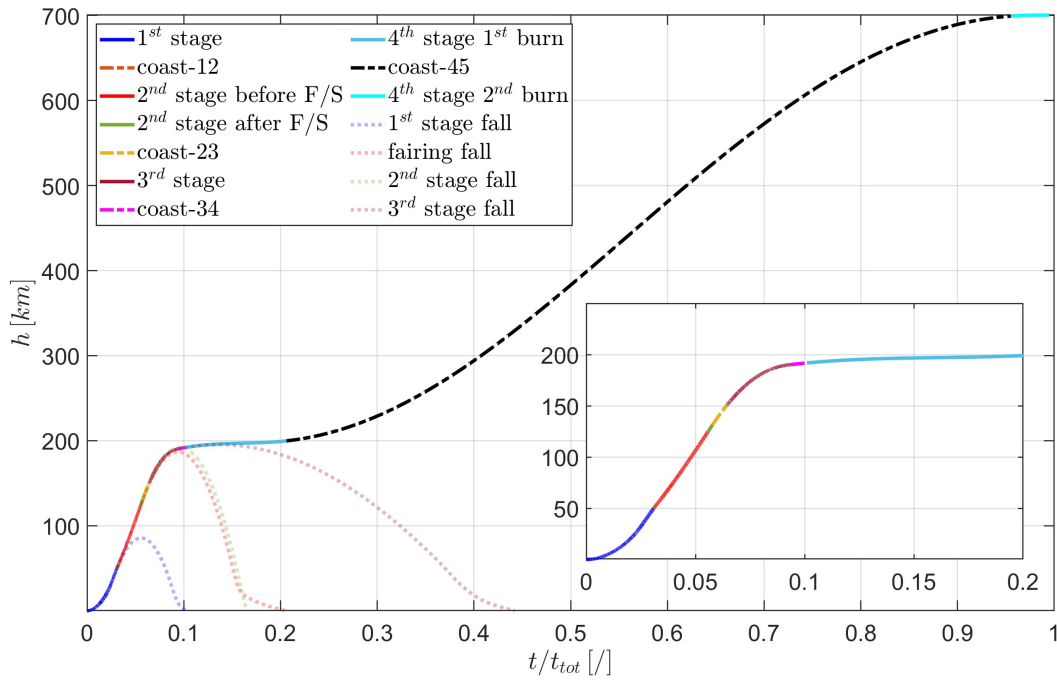


Figure 3.8: Altitude history VEGA inspired SO.

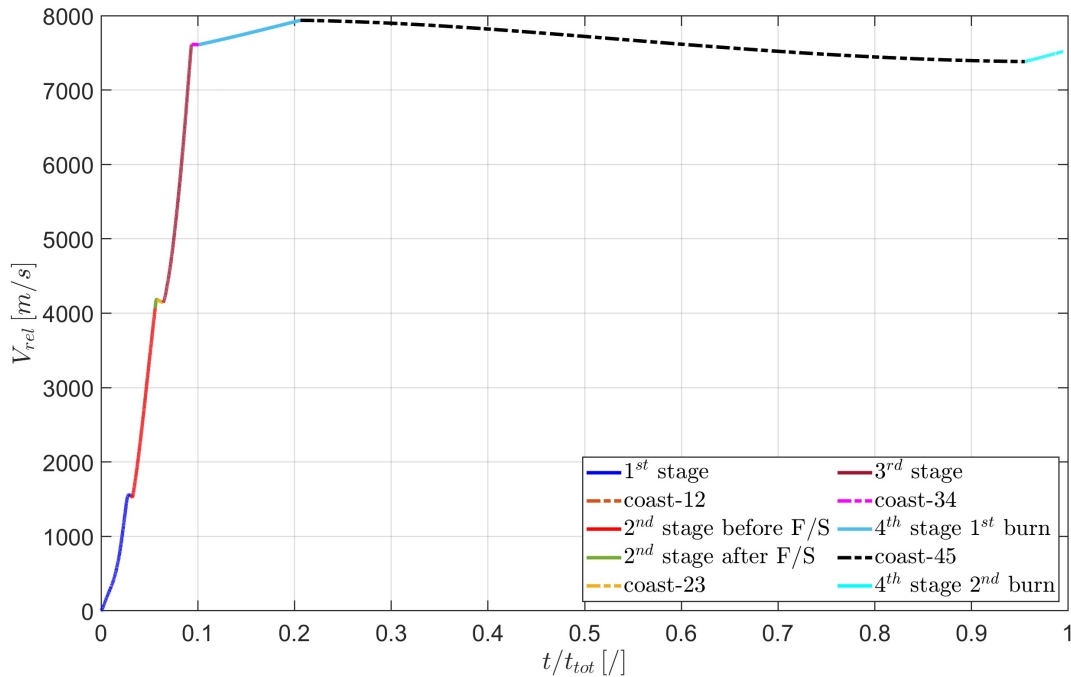


Figure 3.9: Relative speed history VEGA inspired SO.

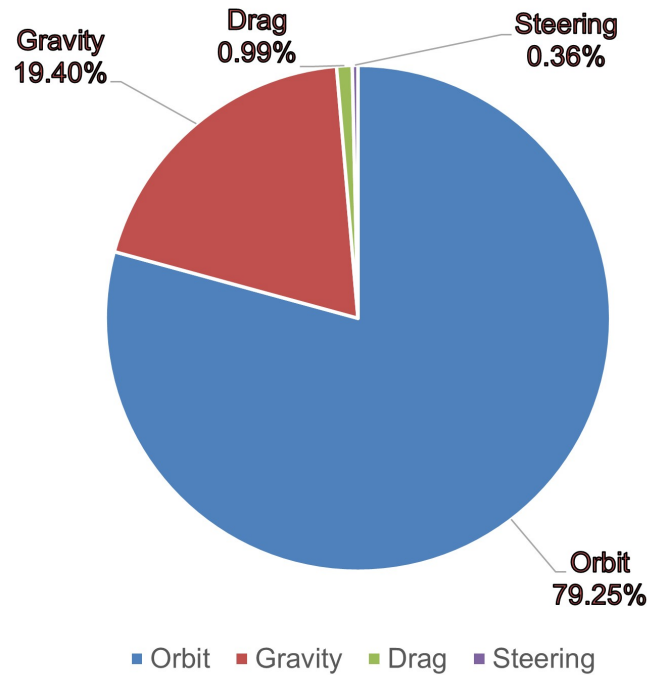


Figure 3.10: Mission velocity partition VEGA inspired SO.

Fig. 3.8 shows the altitude history. The first stage separation occurs at 50 km , the second at 130 km and the third one at 195 km . The fairing jettisoning occurs at 125 km during the second stage flight, meanwhile in the real VEGA LV mission this event happens just after the ignition of the third stage. The first AVUM burn puts the launch vehicle into its transfer orbit around 200 km , then, after a long coasting phase, the second AVUM burn occurs at 700 km in order to circularize

the orbit. The transfer orbit perigee is 200 km , safely above the limit of 150 km . The flight phases of the launch vehicle are well distinguished in Fig. 3.9 representing the trend of relative speed. Propelled phases imply an increase in speed, while coasting phases a decrease of it. During the longest coasting phase of the transfer orbit occurs a significant transformation between kinetic and potential energy indeed, the relative speed decreases from 8000 m/s to 7300 m/s , while the altitude increases by 500 km . From the energy point of view, the mission is summarized in Fig. 3.10, where the breakdown of the total velocity to enter orbit is shown. In Fig. 3.11 are displayed the flight maneuvers of the SRMs stages: the pitch over maneuver for first stage (Fig. 3.11(a)), and the steering strategy for second (Fig. 3.11(b)) and third stage (Fig. 3.11(c)). In Fig. 3.12 are shown the flight maneuvers of AVUM, the first burst is performed with a slightly positive flight path angle (see Fig. 3.12(a)), instead the second burst ends completely parallel to the local horizon. The maneuvers are determined by the constraint on maximum AoA , which is maintained under 5 deg until the fairing separation and under 15 deg after it, as displayed in Fig. 3.13. The jettison of the fairing occurs when the aero-thermal heat flux is below the threshold of 1135 W/m^2 , as displayed in Fig. 3.14. The first stage aero-thermal heat flux is largely overestimated because the Eq.(2.112) is not valid in the continuous regime. Besides, the small discontinuity visible in the plot during the 2^{nd} stage is due to the change of air density evaluation (from US standard atmosphere table interpolation to analytical estimation). The lower threshold value of the angle of attack before the fairing separation is due to the presence of the atmosphere, that is critical during the first stage flight, indeed, in Fig. 3.15 can be observed the trends of dynamic pressure and angle of attack divided for each phase of first stage flight. The dynamic pressure reaches its maximum of 50 kPa during the gravity turn (see Fig. 3.15(a)). In this phase the angle of attack is equal to zero, thus both the maximum AoA and the product between q and AoA occurs at the end of pitch over, as shown in Fig. 3.15(b). The acceleration (see Fig. 3.16), presents its maximum during third stage flight and it is close to the limit of 50 m/s^2 ; the discontinuity on the second stage acceleration trend is due to the fairing separation. The ground track of the mission is shown in Fig. 3.17. Launching from Kourou, first and second stage and the fairing fall in the Atlantic Ocean, while the third stage in the uninhabited areas of Greenland, because of its high kinetic energy; indeed, the constraint of the falling point of the third stage is very dimensioning for the trajectory. Fig. 3.18(a) exhibits the first stage thrust and chamber pressure, the shape is similar to the original P80, confirming that this thrust vs time trend is optimized for this type of launch vehicle. Meanwhile Fig. 3.18(b) and Fig. 3.18(c) display the second and third stage thrust and pressure trends which are regressive. As concerns the structural analysis, the FEM geometry is shown in Fig. 3.20. As described in Sec. 2.7, the launch vehicle is modeled using 1D elements for reinforcements, 2D ones for SRM and interstages and 3D elements for propellant grain, which presents a simplified shape to match the loaded propellant mass. The considered loadcase is maximum $q \cdot AoA$, assuming a lateral wind gust corresponding to an angle of attack 6 deg at maximum q . This hypothesis is necessary because the ideal 3 DoF trajectory presents zero AoA at maximum q due to the gravity turn maneuver. The corresponding aerodynamic force distribution is shown in Fig. 3.19. The axial force is concentrated in all the profile zones of the LV where there is a change of section: front and bottom of the fairing and interstage 1/2 (see Fig.3.19(a)). Also the lateral force distribution (see Fig. 3.19(b)) presents its peaks on the fairing and the interstage 1/2 and is not null along all the LV axis. Moreover, the reverse-tapered truncated cone should produce a stabilizing force, in the opposite direction of

the nose cone, as shown in Fig. 2.14(b). However, this trend does not appear in Fig. 3.19(b) due to a different truncated cone angle and Mach number. The resulting center of pressure is located around 35 % from the nose tip. The distance between the center of pressure and the center of gravity is a very important parameter for the controllability of the launch vehicle. With this lateral aerodynamic force distribution, the static controllability margin is $SC = 1.76$. This value is correctly above the minimum threshold of 1.5, suggested by Ref. [99]. Although not explicitly present as a constraint, static controllability occurs because of the limits imposed on maximum dynamic pressure. Fig. 3.21 and Fig. 3.22 display respectively the static stress tensor and the first buckling mode for the aforementioned load-case. The maximum stress occurs at the polar boss of first stage because in that point is attached the concentrated mass of the nozzle, in which acts the thrust of the SRM. The maximum displacement is of 9.47 *cm* and happens at the tip of the fairing (this is the result of the lateral aerodynamic force). As regard the buckling, by the first mode can be seen that the component more subjected to buckling failure is the interstage 1/2, which has a thickness of 4.3 *mm*, while the interstage 2/3 has a thickness of 4.6 *mm* and it is reinforced by 47 "H" shaped stringers with a dimension of 8.9 *mm*. The buckling load multiplier is equal to 1.79, safely above its threshold of 1.5. The lack of symmetry of the first buckling mode is due to the combined action of the aerodynamic force torque and the side thrust, which flex the launch vehicle, creating a compression zone and a diametrically opposite tension zone.

The optimal configuration is resumed in Tab. 3.5. The propellant distribution is similar to VEGA, however there is an increase of 22.7% of second stage propellant mass and a decrease respectively of 5.5% and 16.9% for first and third stage. The AVUM propellant decreased of 10.6%. Moreover, even the diameter decreased of 6.7% for the first stage and increased of 5.2% for the upper stages. Thus, the difference between stages diameters is decreased of 36% with a beneficial effect on the aerodynamic drag, which is proportional to this difference between stages diameter (a wide difference means stronger shock waves in supersonic regime). The payload mass increased of 8.95% with respect to the real VEGA and the lift-off mass is 98.77% the original one. Thanks to the genetic optimizer the velocity losses have been reduced and the Lagrangian optimizer found a correct distribution of propellant mass in order to increase the payload ratio.

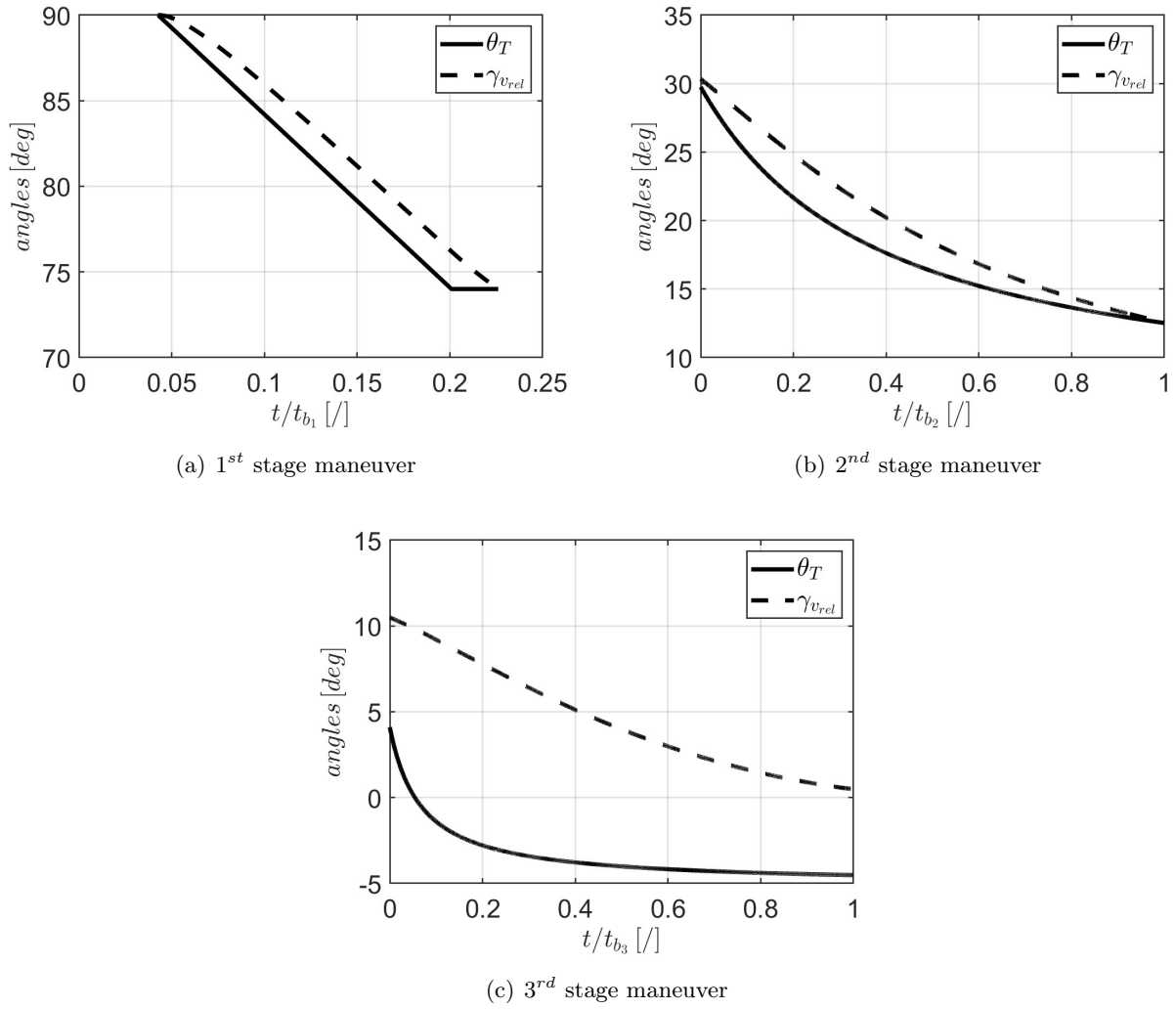


Figure 3.11: SRMs maneuvers VEGA inspired SO.

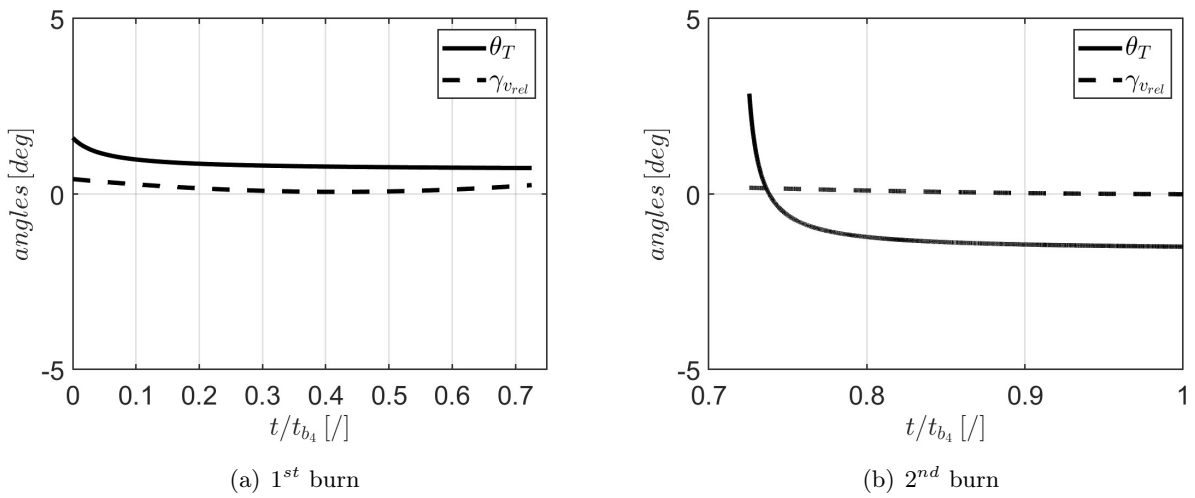


Figure 3.12: AVUM maneuvers VEGA inspired SO.

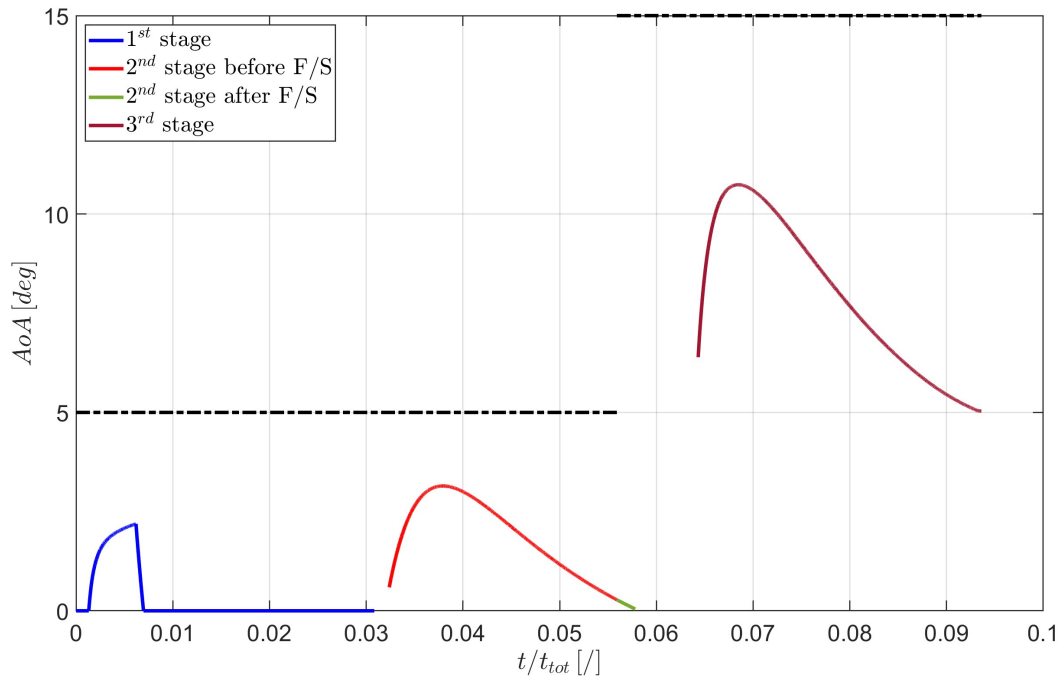


Figure 3.13: Angle of attack VEGA inspired SO.

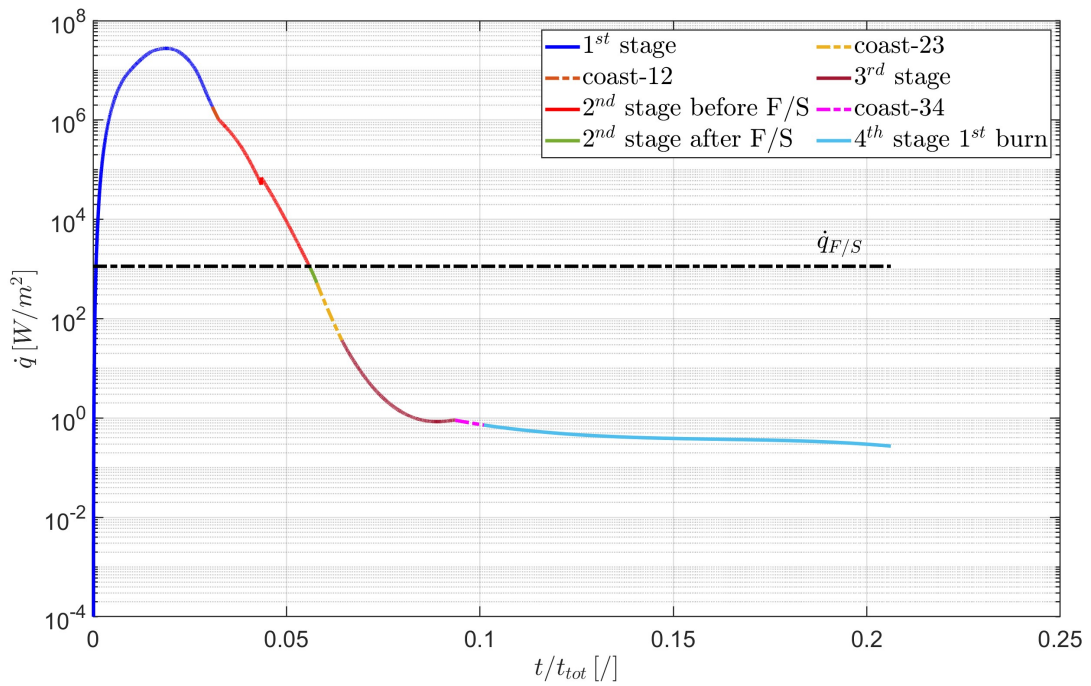


Figure 3.14: Aero-thermal heat flux VEGA inspired SO.

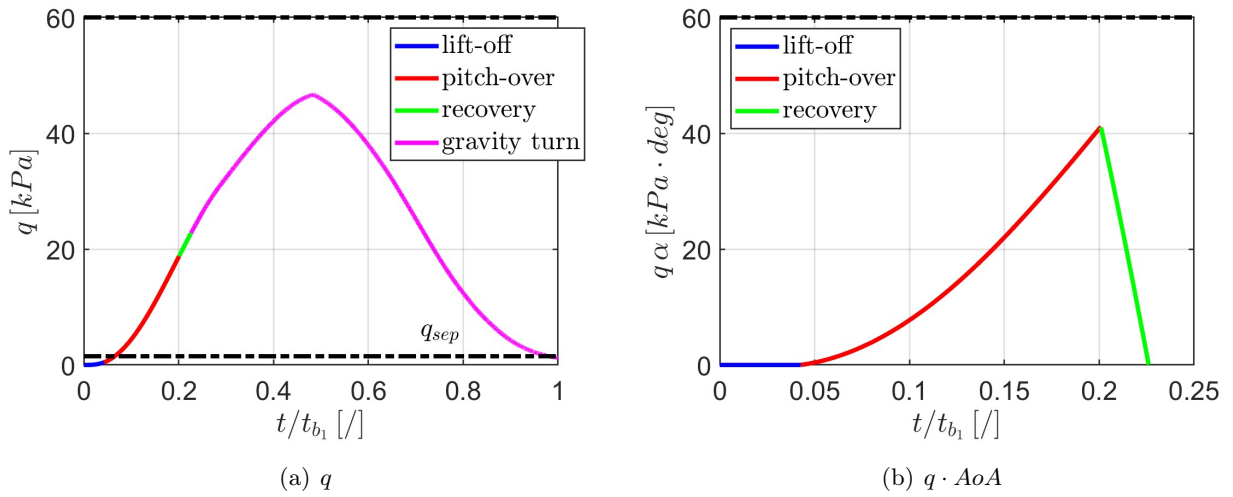


Figure 3.15: Dynamic pressure and $q \cdot AoA$ VEGA inspired SO.

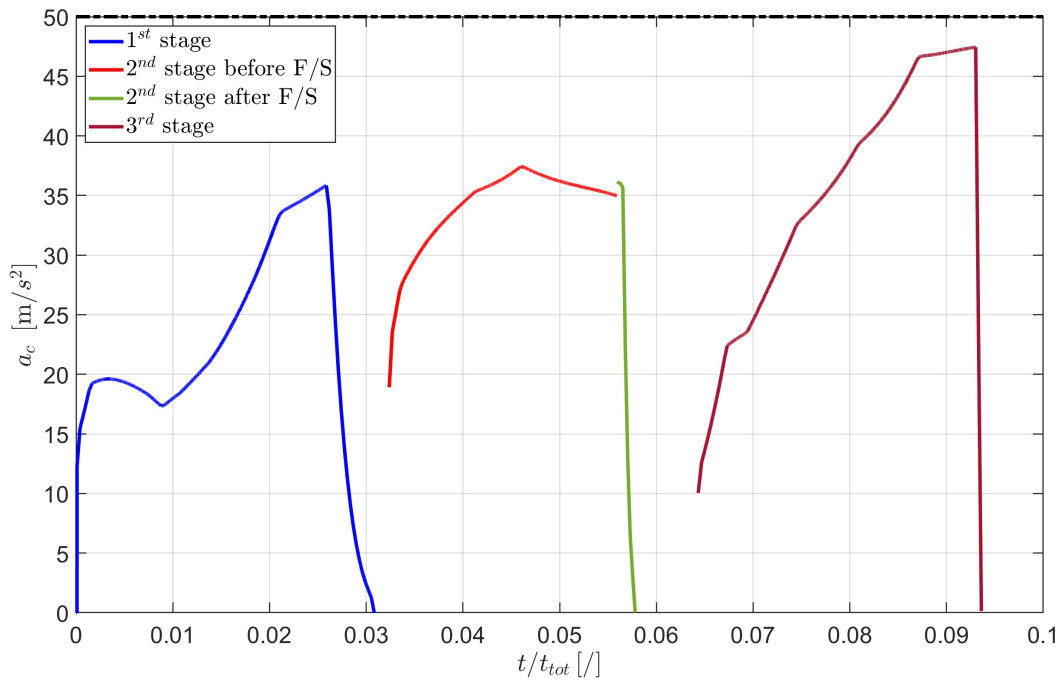
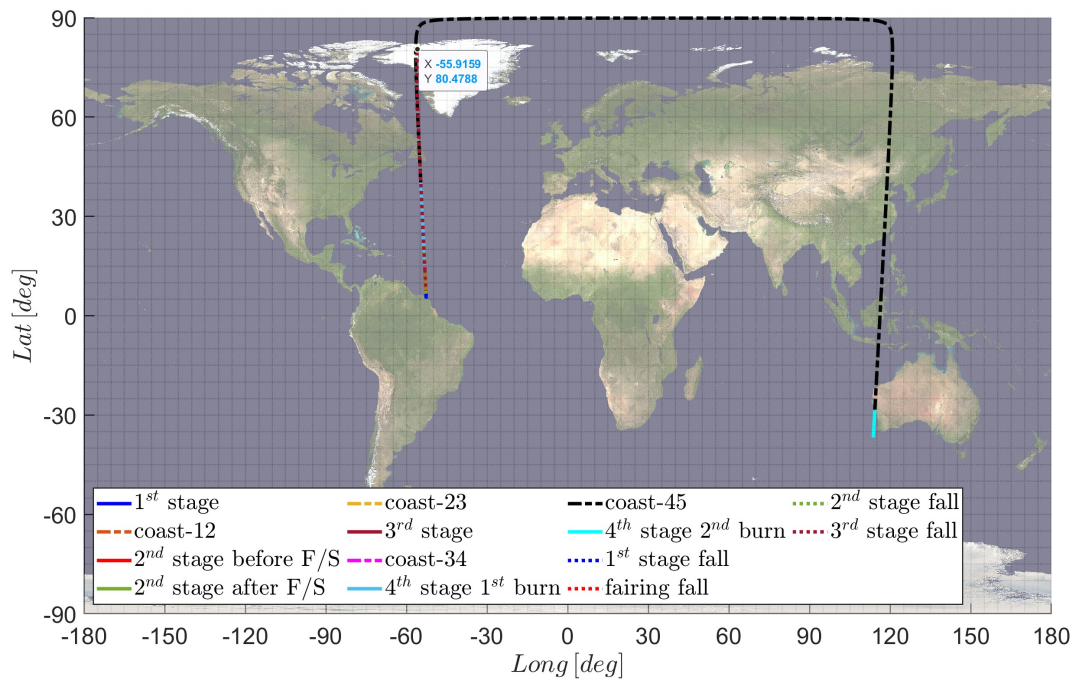


Figure 3.16: Acceleration VEGA inspired SO.

Table 3.5: Comparison between VEGA LV (taken from Ref. [97]) and VEGA inspired SO configuration.

Parameter	Unit	VEGA	VEGA inspired SO	note
1 st stage diameter	<i>m</i>	3	2.8	
2 nd , 3 rd & 4 th stage diameter	<i>m</i>	1.9	2	
Total length	<i>m</i>	29.9	28.7	
1 st stage propellant mass	<i>kg</i>	87710	82889	
2 nd stage propellant mass	<i>kg</i>	23814	29223	
3 rd stage propellant mass	<i>kg</i>	10567	8785	
4 th stage propellant mass	<i>kg</i>	577	516	
1 st stage inert mass	<i>kg</i>	8533	7801	
2 nd stage inert mass	<i>kg</i>	2486	3356	
3 rd stage inert mass	<i>kg</i>	1433	817	
4 th stage inter mass	<i>kg</i>	688	688	*imposed value
1 st stage vacuum specific impulse	<i>s</i>	280	285.06	
2 nd stage vacuum specific impulse	<i>s</i>	287.5	293.86	
3 rd stage vacuum specific impulse	<i>s</i>	295.9	296.35	
4 th stage vacuum specific impulse	<i>s</i>	314.6	314.6	*imposed value
1 st stage nozzle expansion ratio	/	/	21	
2 nd stage nozzle expansion ratio	/	/	39.8	
3 rd stage nozzle expansion ratio	/	/	80.7	
Fairing mass	<i>kg</i>	540	536	
Payload adapter mass	<i>kg</i>	77	77	*imposed value
Payload mass	<i>kg</i>	1430	1558	
Total mass	<i>kg</i>	137855	136162	

**Figure 3.17:** Ground track VEGA inspired SO.

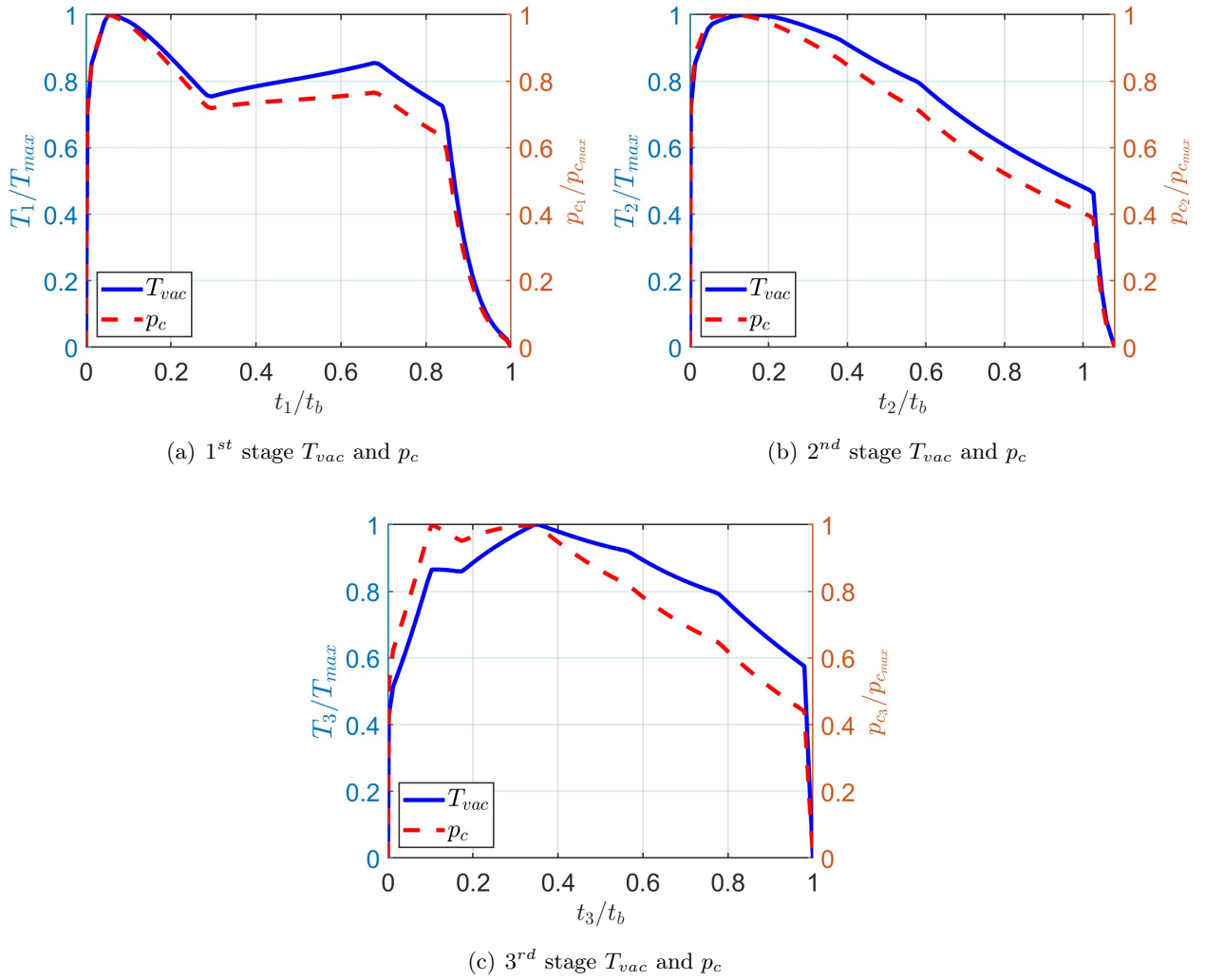


Figure 3.18: SRMs thrust and pressure VEGA inspired SO.

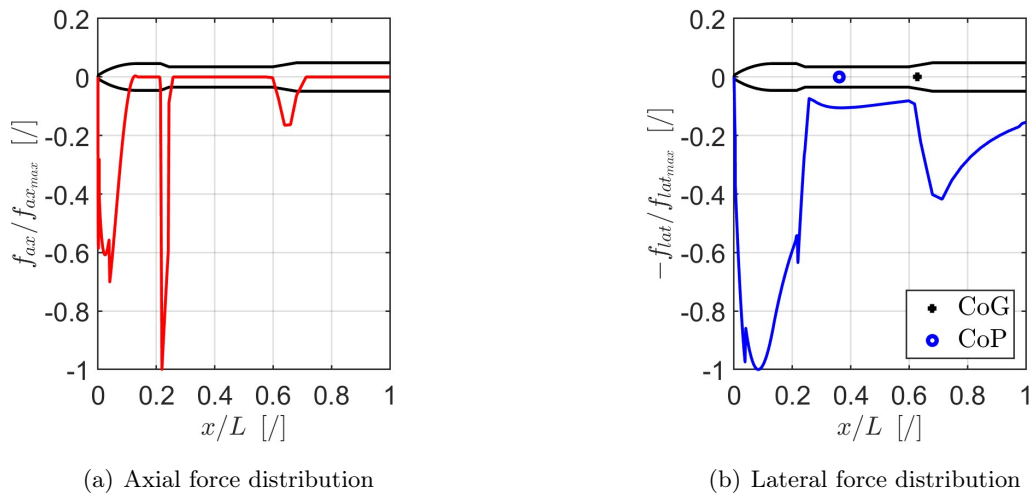


Figure 3.19: Aerodynamic forces distribution at q_{max} ($Mach = 1.89$) VEGA inspired SO.

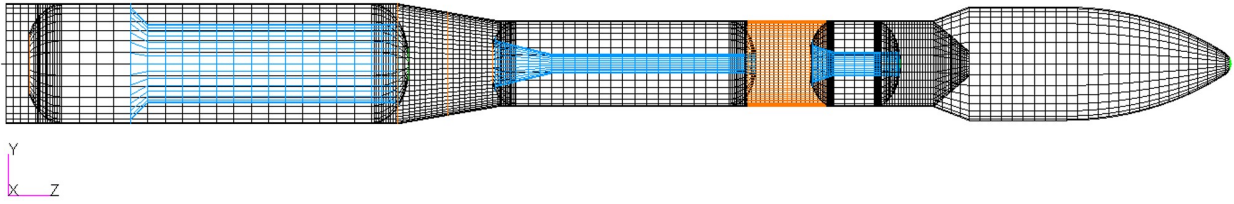


Figure 3.20: FEM geometry at q_{max} VEGA inspired SO.

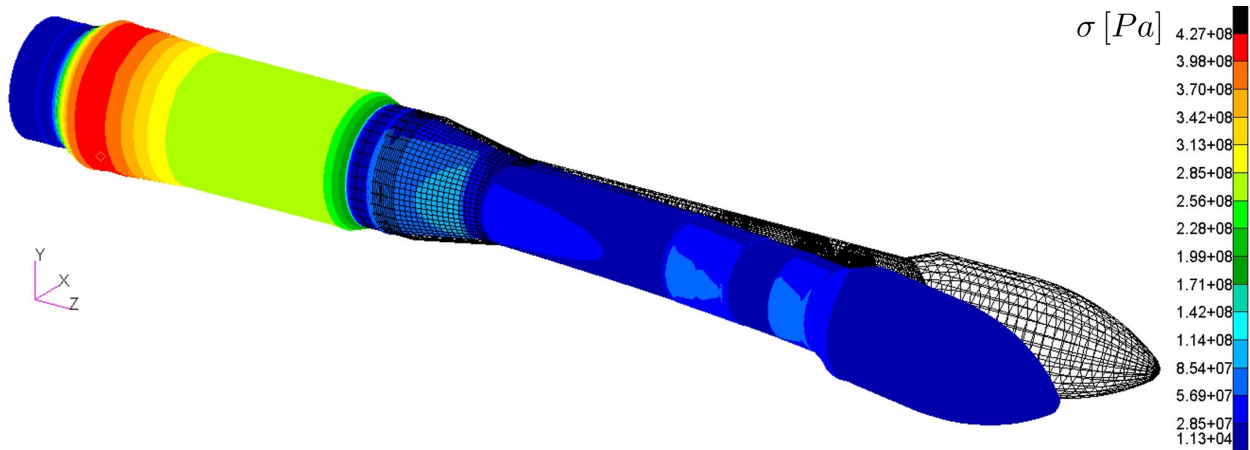


Figure 3.21: Static stress tensor at q_{max} VEGA inspired SO.

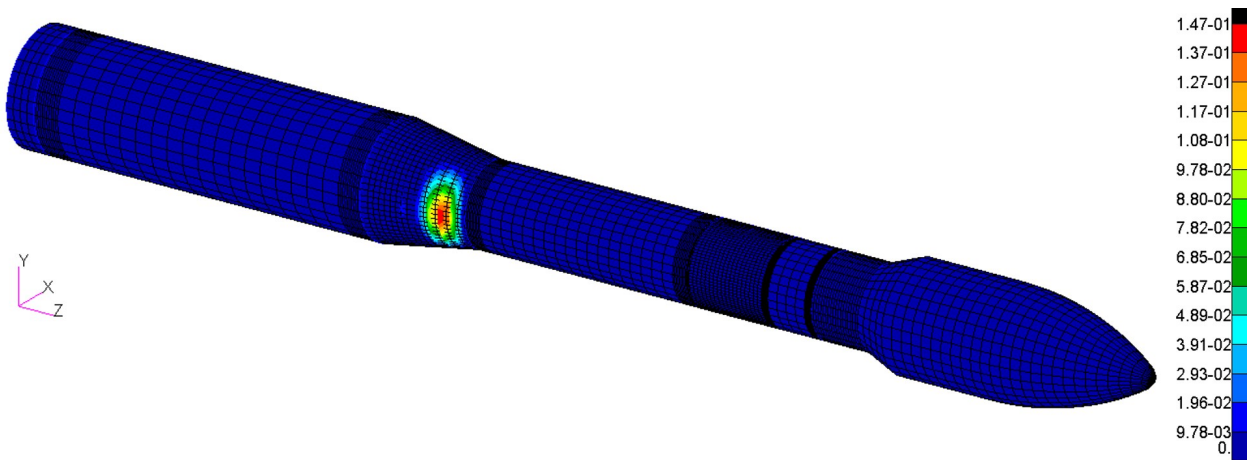


Figure 3.22: First buckling mode at q_{max} VEGA inspired SO.

3.2.2 Multi-objective MDO

Switching from one to multiple objectives allows to glean more information about the design of a launch vehicle, so the results of an optimization with two contrasting objectives (payload mass and lift-off mass) are discussed below. Considering the same starting DOE, a multi-objective multidisciplinary design optimization has been carried out on the VEGA inspired LV. The constraints are the same displayed in Tab. 3.4 with the exception of the ones on minimum payload and maximum lift-off mass, which have been removed, as these two quantities represents the objective to be

respectively maximize and minimize.

$$\begin{aligned} J_1 &= m_{pl} \uparrow \\ J_2 &= m_0 \downarrow \end{aligned} \quad (3.3)$$

Fig. 3.23 displays the pareto frontier at the end of the optimization cycle composed by 60 generation of *MOGA-II* algorithm. The space of solution is very large, spanning from 90 to 115 in non dimensional GLOM and from 90 to 135 in non dimensional payload. However, the feasible solutions have been found just in region between 97 and 98.5 in dimensionless GLOM and 107 to 110.5 in dimensionless payload. In particular the frontier is represented by the upper boundaries of the feasible solutions. As expected, the two goals are in a directly proportional relationship: as the GLOM increases, there is a corresponding increment in payload. The extreme points A and B are respectively the solution with minimum GLOM and maximum payload.

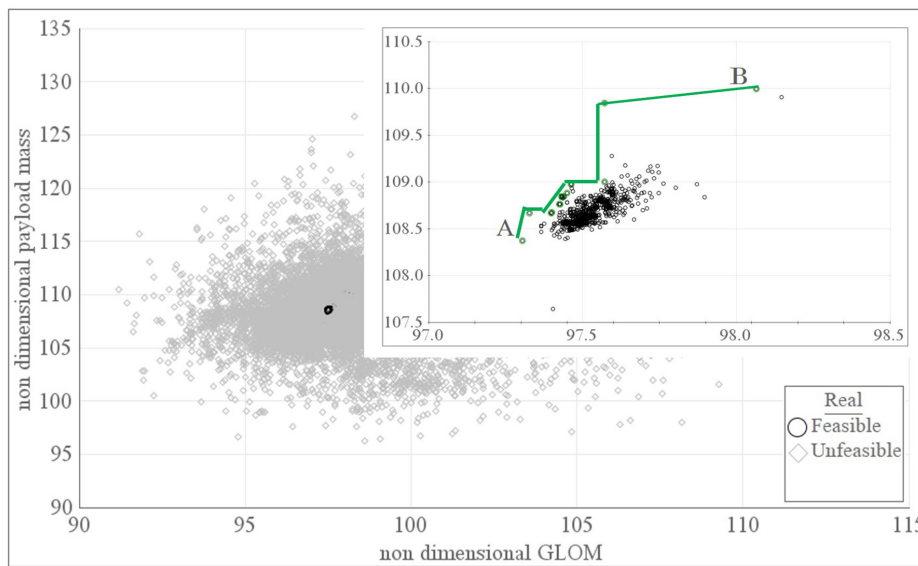


Figure 3.23: Pareto plot VEGA inspired MO.

The following charts are related just to the solution B, as the solution A presents similar values of design variables and therefore similar charts. This is an indication of the goodness of the solution, because this evolutionary convergence indicates the possible presence of a global optimum. The altitude history of Fig. 3.24 indicates that the first stage separation occurs at 50 km , the second at 130 km and the third one at 195 km . From the relative speed graph in Fig. 3.25, it can be seen that the third stage provides most of the Δv . On the other hand, with regard to the overall velocity required for orbital entry, a detailed breakdown is presented in Fig. 3.26. The maneuvers shown in Figs. 3.27 and 3.28 produce the variation of the angle of attack displayed in Fig. 3.29. In particular, the intersection of the pitch angle trend and the flight path angle of Fig. 3.27(b) determines the double peak of AoA during second stage flight. In this phase occurs also the jettisoning of the fairing as shown in Fig. 3.30; after this event the threshold of maximum allowed AoA rises at 15 deg . The dynamic pressure reaches its maximum of 55 kPa during the gravity turn (see Fig.3.31(a)). Instead the product between q and AoA (see Fig. 3.31(b)) presents a maximum of $20 \text{ kPa} \cdot \text{deg}$, which is safely under the limit of $60 \text{ kPa} \cdot \text{deg}$. This low value is due to the short duration of the pitch over, as it can be seen in Fig. 3.27(a). The acceleration (see Fig. 3.32), presents its maximum during third

stage flight and it is close to the limit of 50 m/s^2 . The ground track of the mission is displayed in Fig. 3.33. Launching from Kourou, even for this mission, first and second stage and the fairing fall in the Atlantic Ocean, while the third stage in In the uninhabited areas of Greenland, above 80 deg of latitude. Fig. 3.34(a) exhibits the first stage thrust and chamber pressure, the shape is similar to one of the previous optimization case, even if the maximum thrust is maintained for more time. This characteristic justify the higher dynamic pressure with respect to the SO solution. Meanwhile Fig. 3.34(b) and Fig. 3.34(c) display the second and third stage thrust and pressure trends which are identical to the one of the SO analysis, because the control points of the combustion surface of these SRMs are not part of the design variables. The aerodynamic force distribution is shown in Fig. 3.35. The trends are analogous to the ones of the SO case, due to the similar LV profile. Specifically, as of Fig. 3.19(b), even for this flight condition there is not a stabilizing force on the reverse-tapered truncated cone; this force appears at lower Mach number. The position of the CoP is 36.3% from the tip of the LV and the static controllability margin is equal to 1.54. This value is lower with respect to the one obtained for the SO configuration due to the higher maximum dynamic pressure.

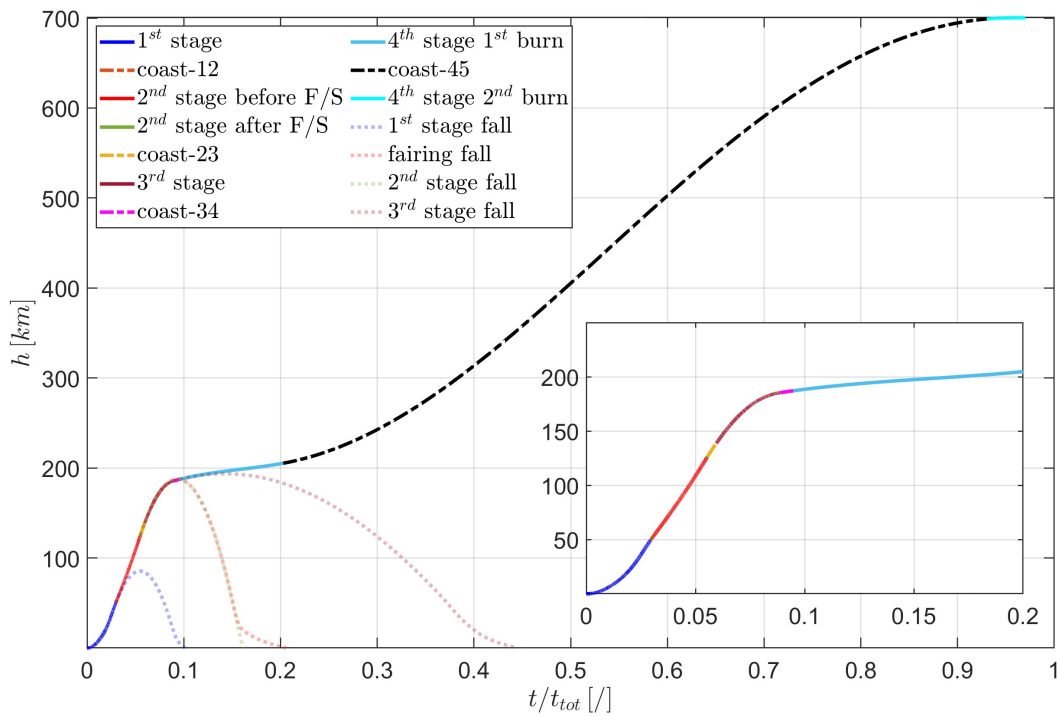


Figure 3.24: Altitude history VEGA inspired MO.

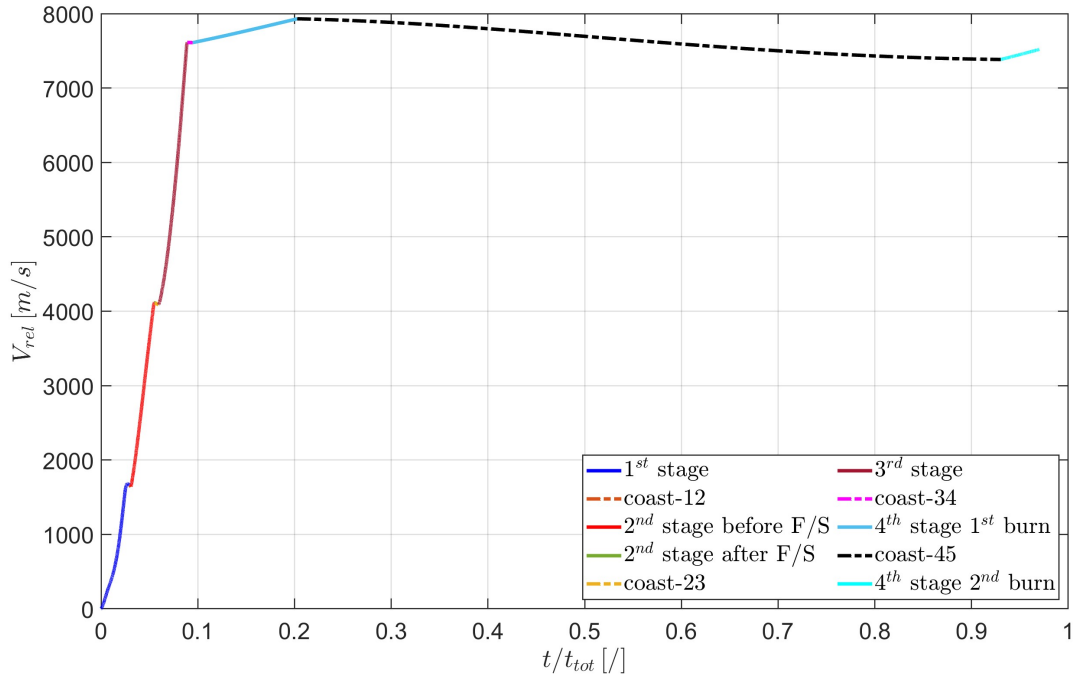


Figure 3.25: Relative speed history VEGA inspired MO.

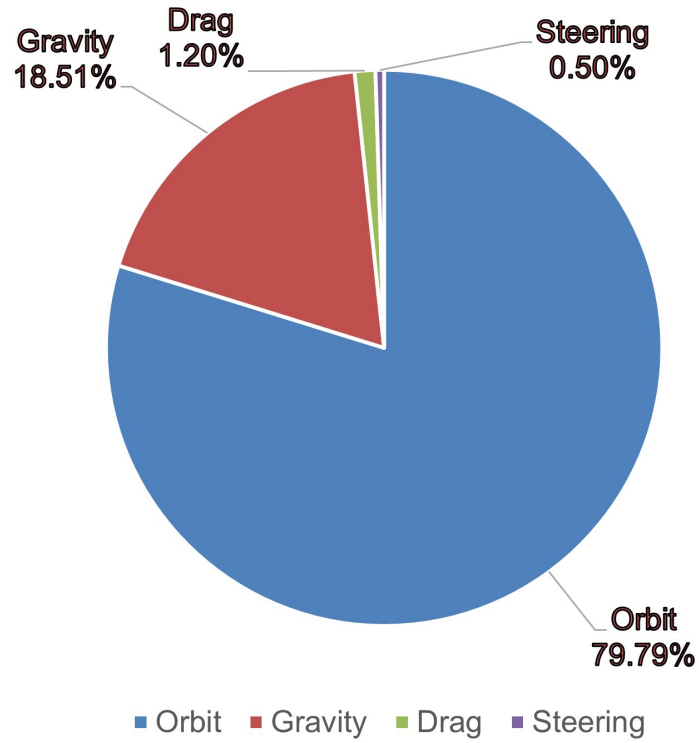


Figure 3.26: Mission velocity partition VEGA inspired MO.

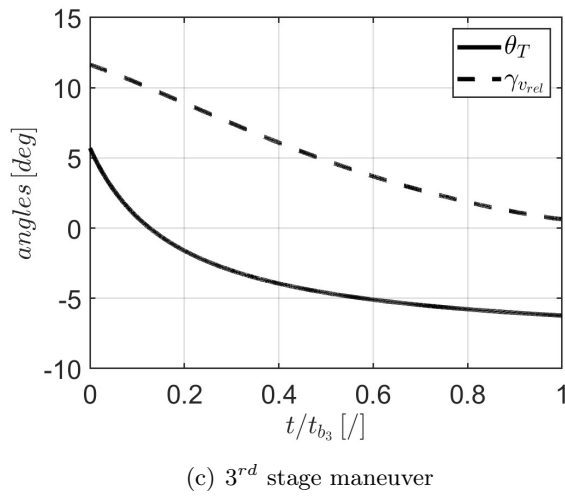
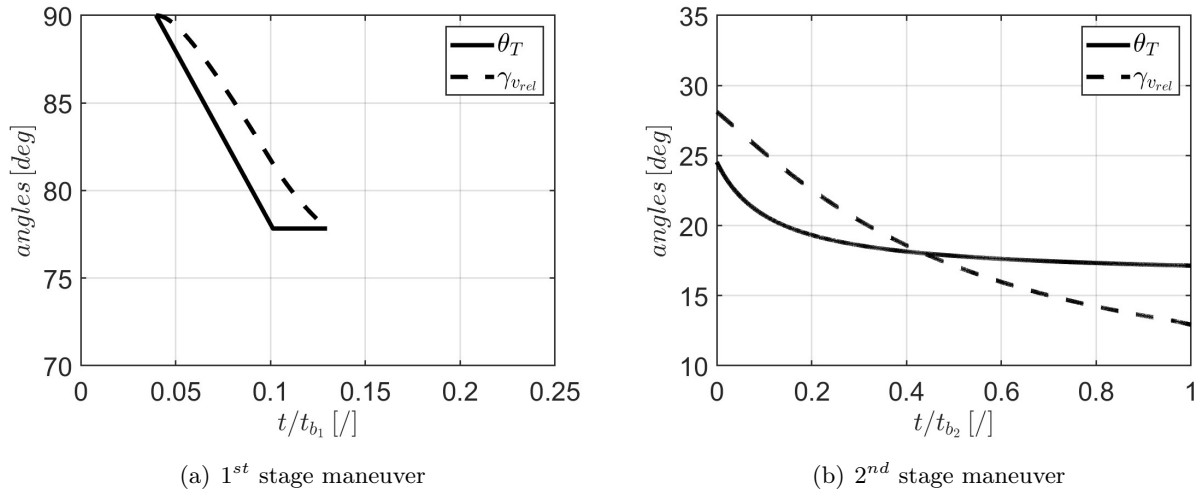


Figure 3.27: SRMs maneuvers VEGA inspired MO.

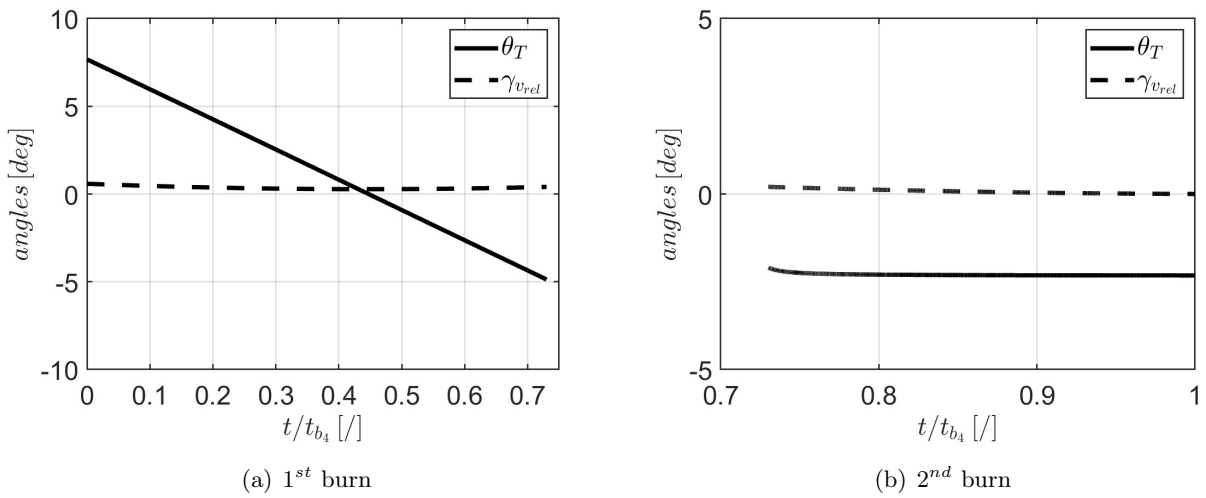


Figure 3.28: AVUM maneuvers VEGA inspired MO.

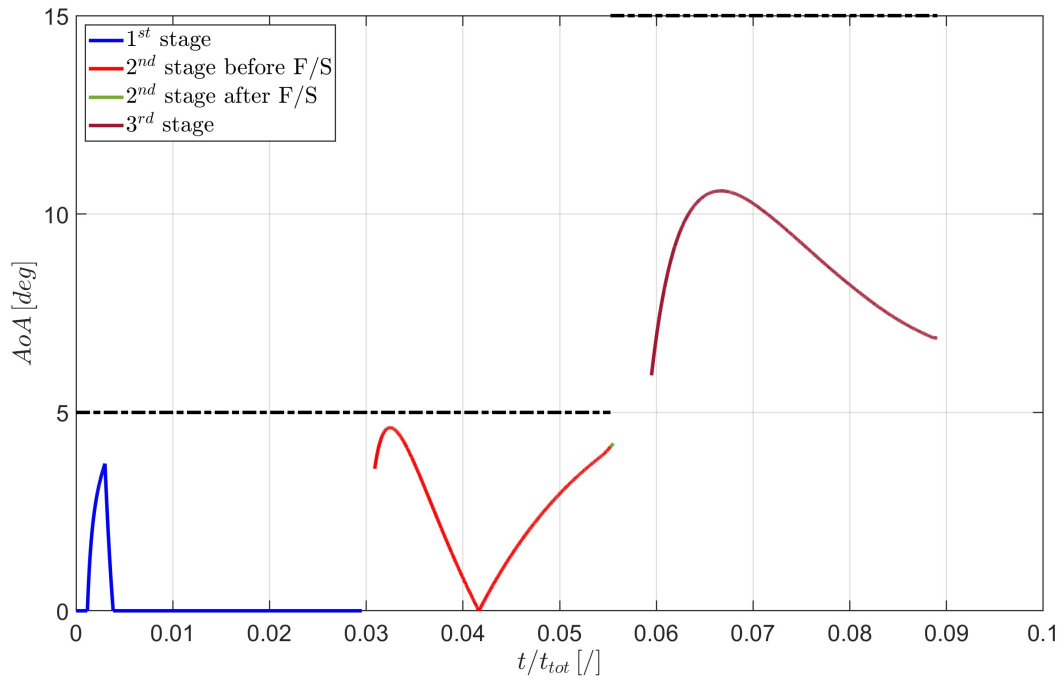


Figure 3.29: Angle of attack VEGA inspired MO.

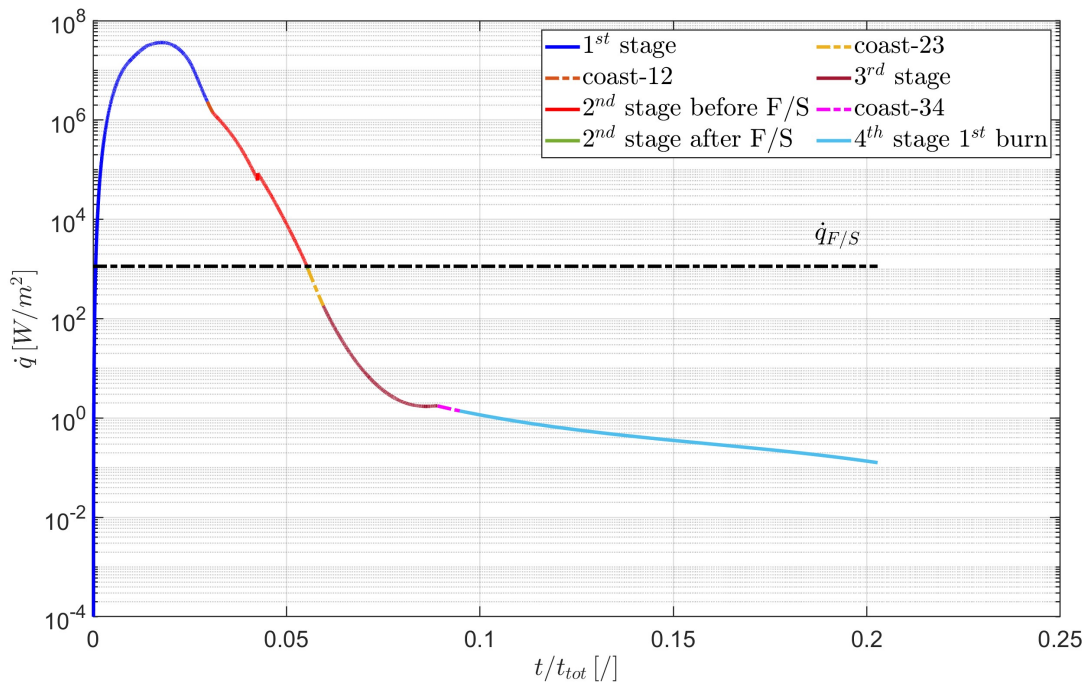


Figure 3.30: Aero-thermal heat flux VEGA inspired MO.

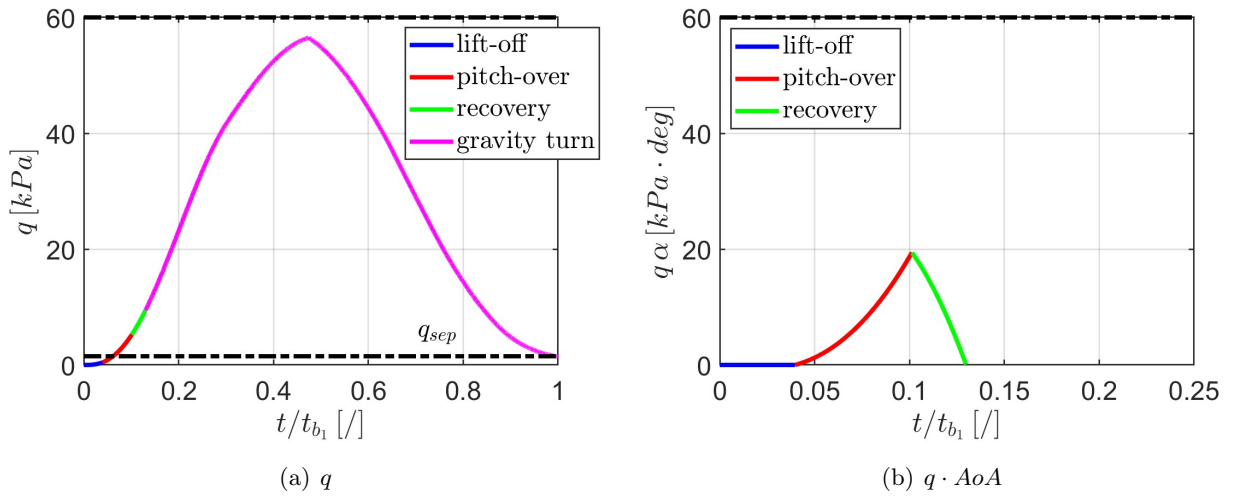


Figure 3.31: Dynamic pressure and $q \cdot AoA$ VEGA inspired MO.

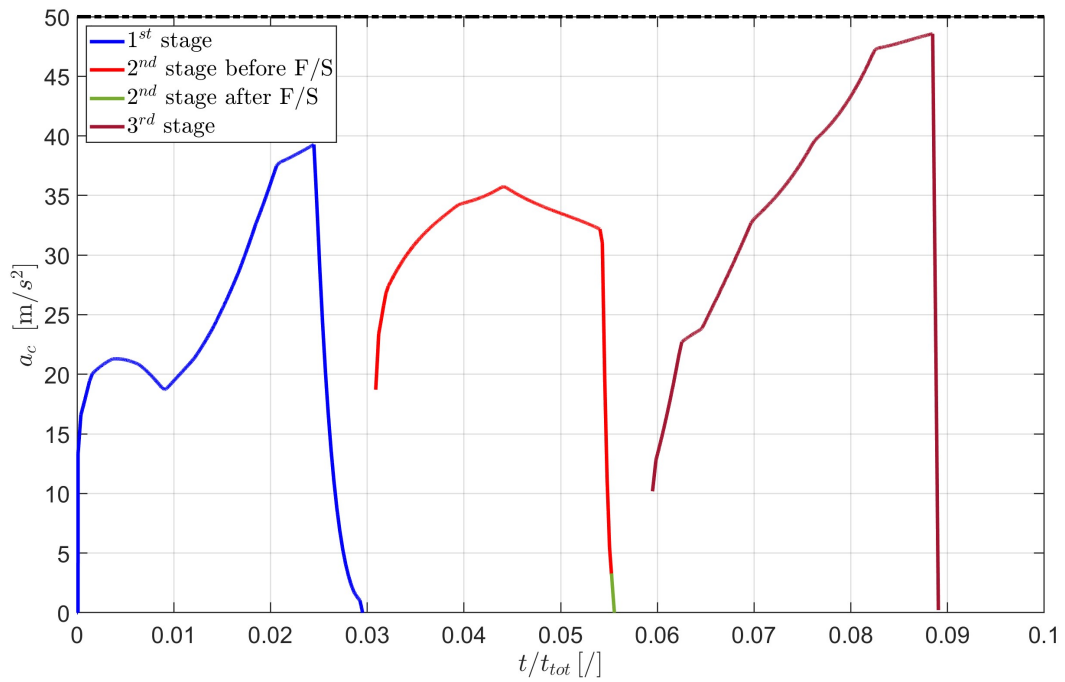
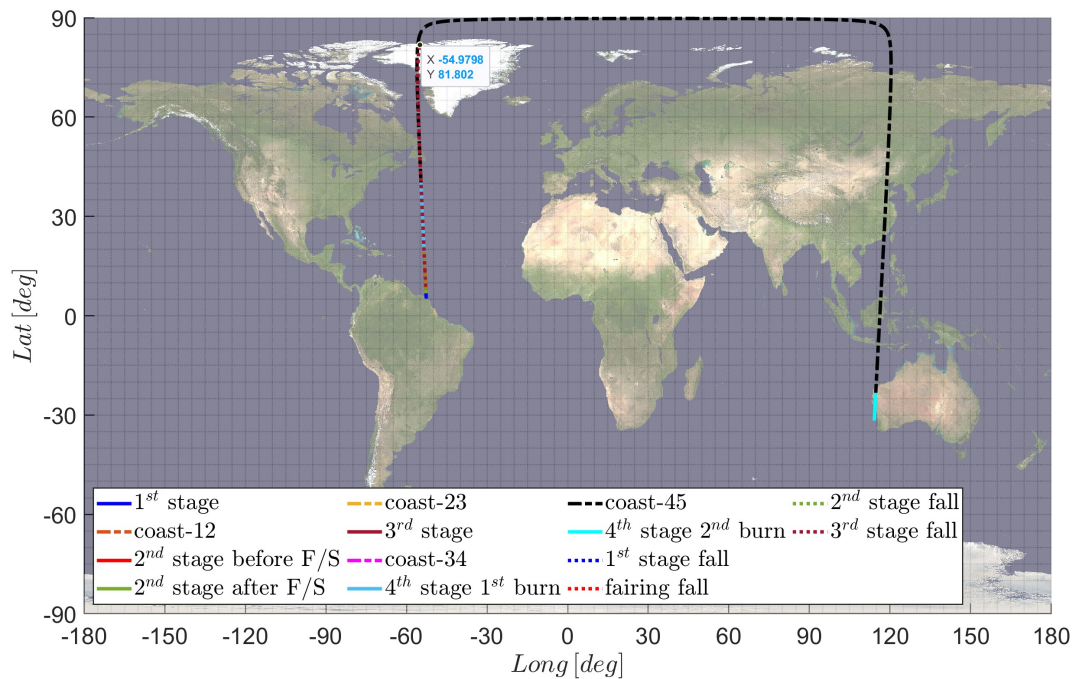


Figure 3.32: Acceleration VEGA inspired MO.

Table 3.6: Comparison between VEGA LV (taken from Ref. [97]) and VEGA inspired MO configuration.

Parameter	Unit	VEGA	VEGA inspired MO	note
1 st stage diameter	<i>m</i>	3	2.8	
2 nd , 3 rd & 4 th stage diameter	<i>m</i>	1.9	2	
Total length	<i>m</i>	29.9	28.07	
1 st stage propellant mass	<i>kg</i>	87710	83513	
2 nd stage propellant mass	<i>kg</i>	23814	27319	
3 rd stage propellant mass	<i>kg</i>	10567	9172	
4 th stage propellant mass	<i>kg</i>	577	524	
1 st stage inert mass	<i>kg</i>	8533	7811	
2 nd stage inert mass	<i>kg</i>	2486	3194	
3 rd stage inert mass	<i>kg</i>	1433	874	
4 th stage inter mass	<i>kg</i>	688	688	*imposed value
1 st stage vacuum specific impulse	<i>s</i>	280	284.12	
2 nd stage vacuum specific impulse	<i>s</i>	287.5	288.22	
3 rd stage vacuum specific impulse	<i>s</i>	295.9	299.75	
4 th stage specific impulse	<i>s</i>	314.6	314.6	*imposed value
1 st stage nozzle expansion ratio	/	/	20	
2 nd stage nozzle expansion ratio	/	/	29.3	
3 rd stage nozzle expansion ratio	/	/	102.9	
Fairing mass	<i>kg</i>	540	539	
Payload adapter mass	<i>kg</i>	77	77	*imposed value
Payload mass	<i>kg</i>	1430	1578	
Total mass	<i>kg</i>	137855	135289	

**Figure 3.33:** Ground track VEGA inspired MO.

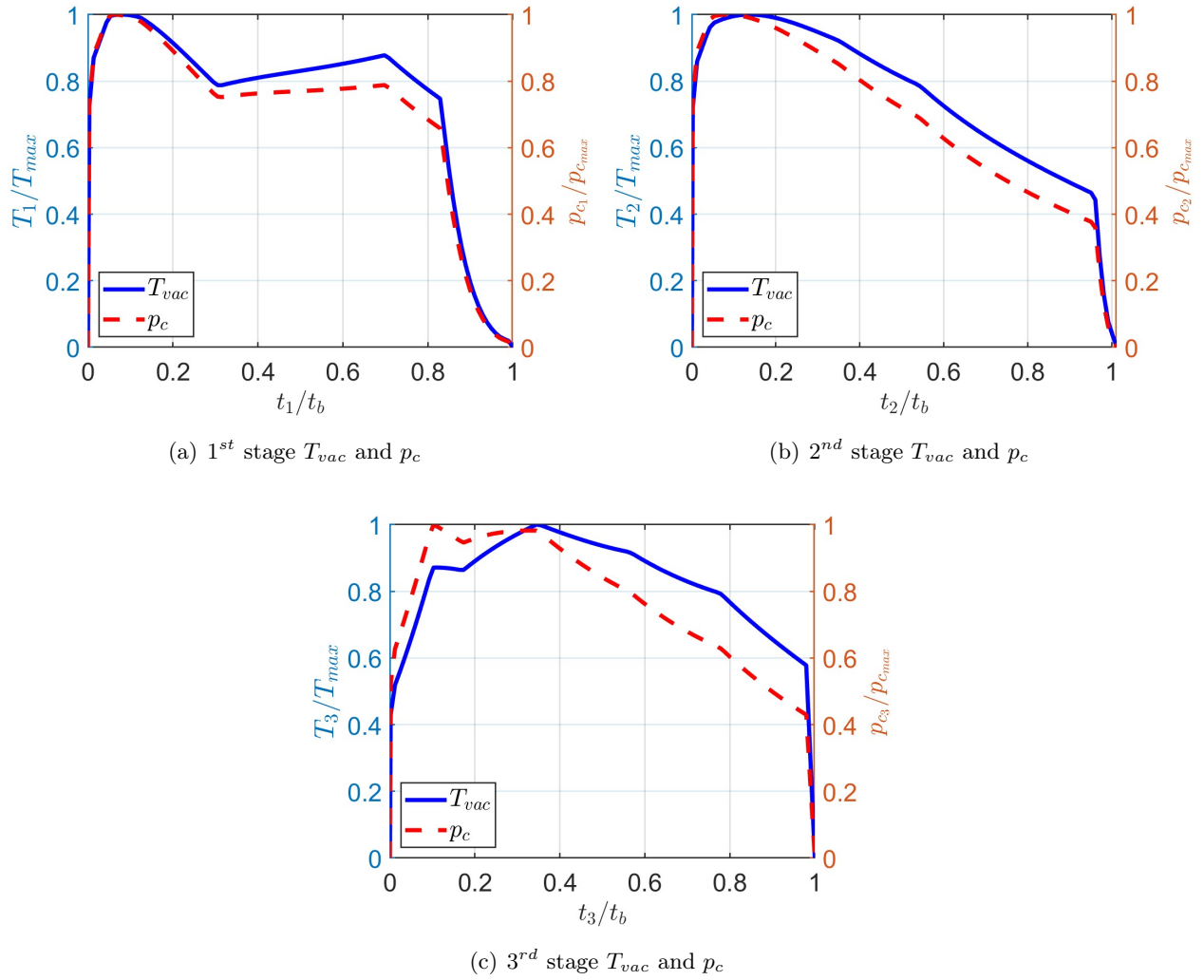


Figure 3.34: SRMs thrust and pressure MO.

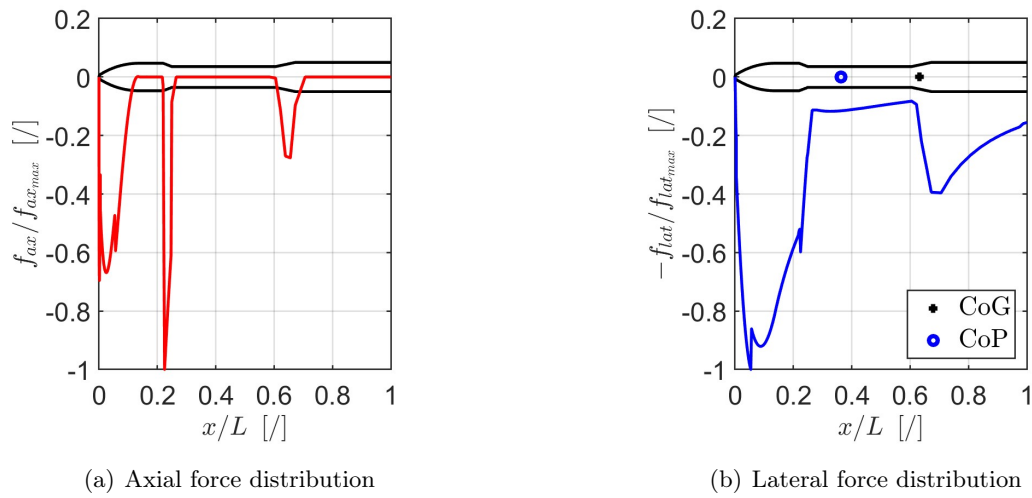


Figure 3.35: Aerodynamic forces distribution at q_{max} ($Mach = 1.89$) VEGA inspired MO.

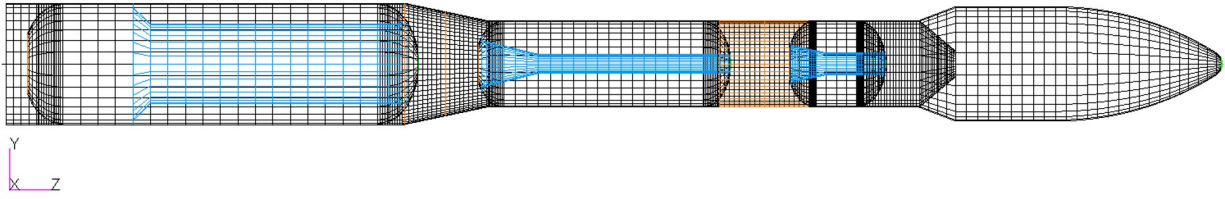


Figure 3.36: FEM geometry at q_{max} ($Mach = 1.72$) VEGA inspired MO.

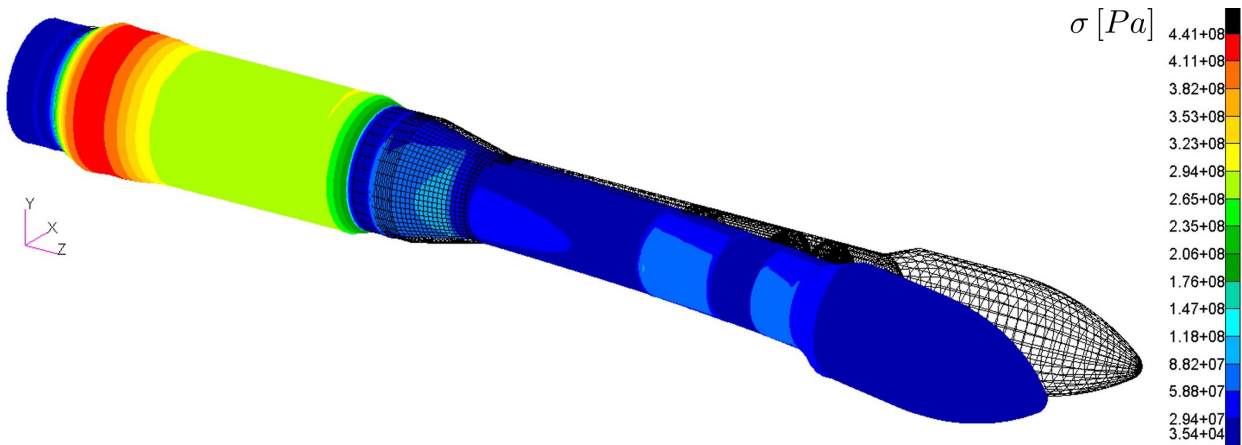


Figure 3.37: Static stress tensor at q_{max} VEGA inspired MO.

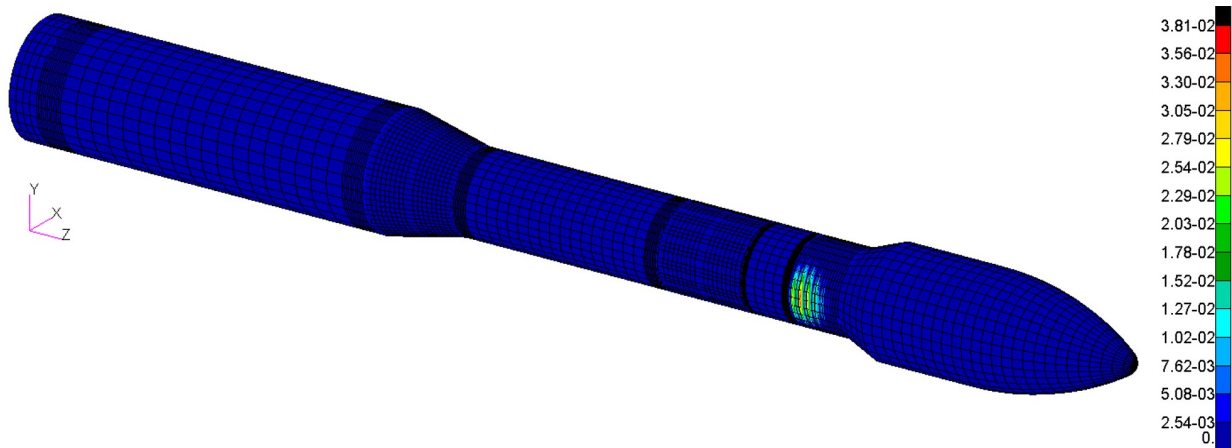


Figure 3.38: First buckling mode at q_{max} VEGA inspired MO.

As concerns the structural analysis, the FEM geometry is shown in Fig. 3.36. Even for this case, the considered loadcase is maximum $q \cdot AoA$, assuming a lateral wind gust corresponding to an angle of attack $6\ deg$ at maximum q . Fig. 3.21 and Fig. 3.22 display respectively the static stress tensor and the first buckling mode. The maximum stress occurs at the polar boss of first stage because in that point is attached the concentrated mass of the nozzle, in which acts the thrust of the SRM. The maximum displacement is of $10\ cm$ and happens at the tip of the fairing. As regard the buckling, by the first mode can be seen that the component more subjected to buckling failure is the interstage 3/4, which has a thickness of $2.8\ mm$, while the interstage 2/3 has a thickness of $3.9\ mm$ reinforced with 17 "H" shaped stringers having a dimension of $17.5\ mm$. The blm is equal to 1.63 which is higher than the imposed limit of 1.5.

The optimal configuration is resumed in Tab. 3.6. Also for this configuration, the propellant distribution is similar to VEGA, however there is an increase of 14.7% of second stage propellant mass and a decrease respectively of 4.8% and 13.2% for first and third stage. The AVUM propellant decreased of 9.2%. The diameters are the same of the ones obtained by the single-objective MDO, confirming the goodness of these values. The payload mass increased of 10.35% with respect to the real VEGA and the lift-off mass is 98.14% the original one. Thanks to the genetic optimizer the velocity losses have been reduced and the Lagrangian optimizer found a correct distribution of propellant mass in order to increase the payload ratio, that is higher with respect to the solution obtained by the SO MDO.

3.3 TSTO LRE based MDO

In this section the results of the multi-objective optimization on a two stage liquid rocket engine based launch vehicle are presented. As in Sec. 3.2.2 the two objectives are the payload mass and the lift-off mass which have to be respectively maximize and minimize.

$$\begin{aligned} J_1 &= m_{pl} \uparrow \\ J_2 &= m_0 \downarrow \end{aligned} \tag{3.4}$$

For this LV configuration the design steps are the same described in Fig. 2.4, however the Lagrangian optimizer has been not adopted. This choice is justified by the fact that this LV configuration is designed to use engines that have propulsion characteristics already defined (specific impulse and nominal mass flow rate). Therefore, the design variables are also different from previous configurations. The reference mission is the same of the LV configurations discussed in the previous sections: 700 km PEO from Kourou. The design variables are listed in Tab. 3.7. The main difference from the VEGA inspired case is the appearance of propellant mass among the design variables. In fact, due to the absence of the Lagrangian optimizer for the staging, it is necessary to directly estimate the propellant mass. Besides, LRE tanks are reinforced with stringers, which have to vary in number and size, thus the amount of structural design variables is substantial. Another difference from the VEGA inspired configuration is that 100% real FEM solver was used. Further studies need to be done to create the virtual FE model with these design variables. The constraints are reported in Tab. 3.8. For this LV configuration the diameter is constant and presents the same value between 1st and 2nd stage. This implies a concentration of the aerodynamic force distribution on the fairing, with a consequent displacement of the CoP towards the tip of the LV. Moreover, in this case, there is not a reference value that guarantees the static controllability. Therefore it is necessary to add the constraint on static controllability according to which the maximum torque that the TVC system can generate must be 150% of the maximum aerodynamic one.

Fig. 3.39 displays the Pareto plot of the obtained solutions. It can be observed that in the explored space, the non dimensional lift-off mass spans between 53 and 57, while the resulting adimensional payload varies widely between 10 and 190. The feasible solutions are concentrated in a small portion of the space (between 54.7 and 54.9 of non dimensional GLOM and between 90 and 93 of non dimensional payload). Therefore also the resulting Pareto frontier is small in size. This effect is due to the fact that pre-determination of propellant type and specific impulse is actually imposing a well-determined optimal propellant mass and consequently an initial LV mass.

Table 3.7: Design variables TSTO.

Variable	Symbol	Range	Unit	Type	Class
Upper mass	m_{up}	[1300; 1400]	<i>kg</i>	continuous	mass
Tank flattening coeff.	$h_{d,2}$	[0.45; 0.65]	/	continuous	structure
Tanks thickness	$t_{t_{1,2,3,4}}$	[1; 5]	<i>mm</i>	continuous	structure
Tanks stringers number	$N_{str_{t_{1,2,3,4}}}$	[3; 71]	/	discrete	structure
Tanks stringers dimension	$r_{str_{t_{1,2,3,4}}}$	[1; 20]	<i>mm</i>	continuous	structure
Tanks skirts thickness	$t_{sk_{1,2,3,4}}$	[1; 5]	<i>mm</i>	continuous	structure
Interstage 0/1 thickness	$t_{is_{01}}$	[1; 5]	<i>mm</i>	continuous	structure
Intertank 1/2 thickness	$t_{it_{12}}$	[1; 5]	<i>mm</i>	continuous	structure
Intertank 1/2 stringers dimension	$r_{str_{it_{12}}}$	[1; 20]	<i>mm</i>	continuous	structure
Interstage 1/2 thickness	$t_{is_{12}}$	[1; 5]	<i>mm</i>	continuous	structure
Interstage 1/2 stringers number	$N_{str_{is_{12}}}$	[3; 71]	/	discrete	structure
Interstage 1/2 stringers dimension	$r_{str_{is_{12}}}$	[1; 20]	<i>mm</i>	continuous	structure
Equipment bay thickness	t_{eb}	[1; 5]	<i>mm</i>	continuous	structure
1 st stage propellant mass	m_{p_1}	[55000; 57000]	<i>kg</i>	continuous	propulsion
2 nd stage propellant mass	m_{p_2}	[11000; 13000]	<i>kg</i>	continuous	propulsion
1 st stage adimensional mfr control times	τ_{ctrl}	[/; /]	/	continuous	propulsion
1 st stage adimensional mfr controls	\dot{m}_{ctrl}	[/; /]	/	continuous	propulsion
2 nd stage 1 st burning vs max t_b ratio	τ_{b21}/τ_{b2}	[0.9; 0.99]	/	continuous	propulsion
2 nd stage 2 nd burning vs max t_b ratio	τ_{b21}/τ_{b2}	[0.002; 0.012]	/	continuous	propulsion
Azimuth	A_z	[-4; 0]	<i>deg</i>	continuous	trajectory
Pitch over angle	ϑ_{po}	[70; 85]	<i>deg</i>	continuous	trajectory
Pitch over time vs combustion t ratio	τ_{po}/τ_{b_1}	[0.05; 0.2]	/	continuous	trajectory
Coasting time 1/2 vs ref mission t ratio	τ_{c12}/τ_{ref}	[$\simeq 10^{-4}$; 10^{-3}]	/	continuous	trajectory
Transfer orbit time vs ref mission t ratio	τ_{c23}/τ_{ref}	[$\simeq 10^{-4}$; 0.09]	/	continuous	trajectory
2 nd stage 1 st burn initial cmd angle	$\vartheta_{cmd_{21i}}$	[0; 40]	<i>deg</i>	continuous	trajectory
2 nd stage 1 st burn final cmd angle	$\vartheta_{cmd_{21f}}$	[0; 20]	<i>deg</i>	continuous	trajectory
2 nd stage 1 st burn bts coeff.	$\xi_{bts_{21}}$	[-1; 0]	/	discrete	trajectory
2 nd stage 2 nd burn initial cmd angle	$\vartheta_{cmd_{22i}}$	[-5; 5]	<i>deg</i>	continuous	trajectory
2 nd stage 2 nd burn final cmd angle	$\vartheta_{cmd_{22f}}$	[-5; 5]	<i>deg</i>	continuous	trajectory
3 rd stage 2 nd burn bts coeff.	$\xi_{bts_{22}}$	[-1; 0]	/	discrete	trajectory

Table 3.8: Constraints of TSTO.

Output parameter	Symbol	Limit	Unit	Type	Class
2 nd stage burning total time	τ_{bAVUM}	< 650	<i>s</i>	inequality	propulsion
Maximum dynamic pressure	q_{max}	< 35	<i>kPa</i>	inequality	trajectory
Angle of attack SRM endo-atm	$AoA_{endo_{max}}$	< 5	<i>deg</i>	inequality	trajectory
Angle of attack SRM exo-atm	$AoA_{exo_{max}}$	< 15	<i>deg</i>	inequality	trajectory
Product between q & AoA	$(q \cdot AoA)_{max}$	< 35	<i>kPa \cdot deg</i>	inequality	trajectory
Static controllability at q_{max}	SC	> 1.5	/	inequality	trajectory
q at 1 st stage separation	q_{sep}	< 1500	<i>Pa</i>	inequality	trajectory
Aero-thermal heat flux after F/S	\dot{q}_{max}	< 1135	<i>W/m²</i>	inequality	trajectory
Pitch over angular rate	$\dot{\nu}_{po}$	< 2.5	<i>deg/s</i>	inequality	trajectory
Transfer orbit perigee	h_{ptr}	> 150	<i>km</i>	inequality	trajectory
Δ target orbit perigee	Δh_p	< 7 \rightarrow < 0.7	<i>km</i>	inequality	trajectory
Δ target orbit apogee	Δh_a	< 70 \rightarrow < 0.7	<i>km</i>	inequality	trajectory
Δ target orbit inclination	Δi_t	< 0.1	<i>deg</i>	inequality	trajectory
Acceleration induced to payload	a_c	< 50	<i>m/s²</i>	inequality	structure
Buckling load multiplier at max $q \cdot \alpha$	blm	> 1.5	/	inequality	structure
Static stress vs ultimate static stress	σ/σ_{UTS}	< 0.8	/	inequality	structure

The following charts are related just to the solution B. Fig. 3.40 shows the altitude history of the mission. The first stage flights until 73 km. After a very short coasting phase occurs second stage ignition. At 118 km occurs fairing separation and at 173 km the LV starts the transfer orbit. An interesting feature of the obtained altitude profile is that this transfer orbit is a theoretical Homann, since the perigee of the reference orbit coincides exactly with the altitude at the end of the first burn of the second stage. The Homann transfer can also be seen in Fig. 3.41, where there is the decrease in relative speed during coasting, an index of transformation between kinetic and potential energy. Another theoretical behavior can be seen by Fig. 3.44: during the first burn of the upper engine, the second stage flies with a positive angle of attack in a condition called "lofting", which is well explained in Ref. [85]. Indeed, lofting generally happens when an upper stage is underpowered with respect to the others. In order to compensate the low thrust level, a high burning time is needed. When this occurs, it is necessary to loft the LV to a higher altitude, otherwise the LV will start to fall horizontally towards the surface of the planet. The lofted part of the trajectory is justified also by the fact that the rising the altitude permits a quicker fairing jettisoning. The lofting can be observed also looking at the Fig. 3.43(b), indeed the trend of the pitch angle is above the flight path angle for the entire first burn of second stage flight. Instead, as regards the first stage maneuver (see Fig. 3.43(a)), it is noticed that the pitch over angle is higher with respect to the first stage powered by SRM (see Fig. 3.27(a)). This is due to the different thrust shape between SRM and LRE: a constant vacuum thrust level must be compensated by a steeper vertical ascent in order to quickly overcome the denser layers of atmosphere. This steeper vertical ascent causes an increment of gravity losses, which represent about the 20% of the total mission velocity (see Fig. 3.42). However, this steeper vertical ascent helps also to the anticipation of the aforementioned fairing jettisoning as shown in Fig. 3.45. After the fairing separation the aerothermal heat flux remains below its threshold, however there is a slightly increase during to the lofting part of the trajectory due to the local decrease of altitude at perigee. As concern the dynamic pressure, its trend is displayed in Fig. 3.46(a), the maximum value is around 28 kPa, while the final one is correctly under the limit to have a safe stage separation. The low value of pitch over

angle produces an effect also on the product between q and AoA which has a maximum around $25 \text{ kPa} \cdot \text{deg}$.

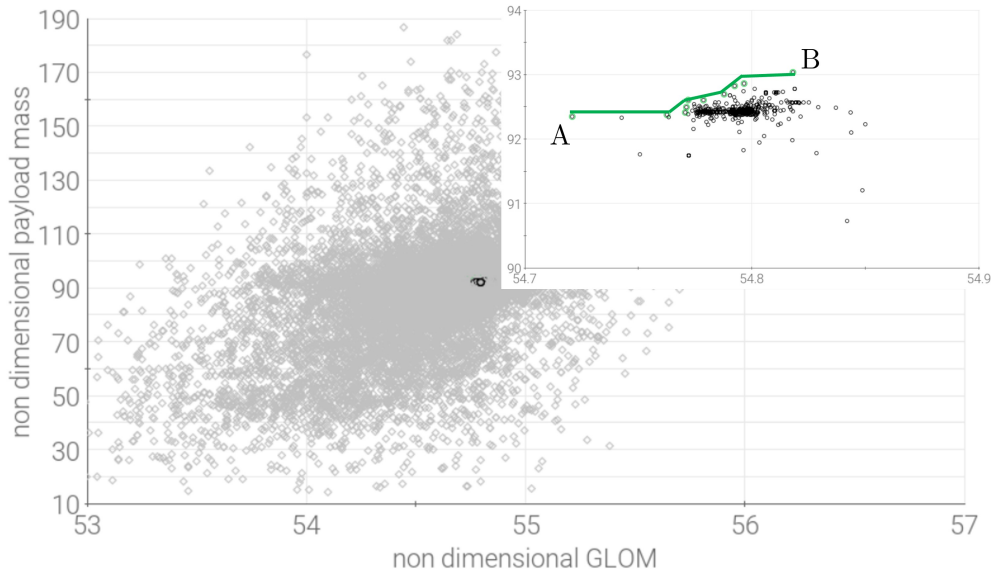


Figure 3.39: Pareto plot TSTO.

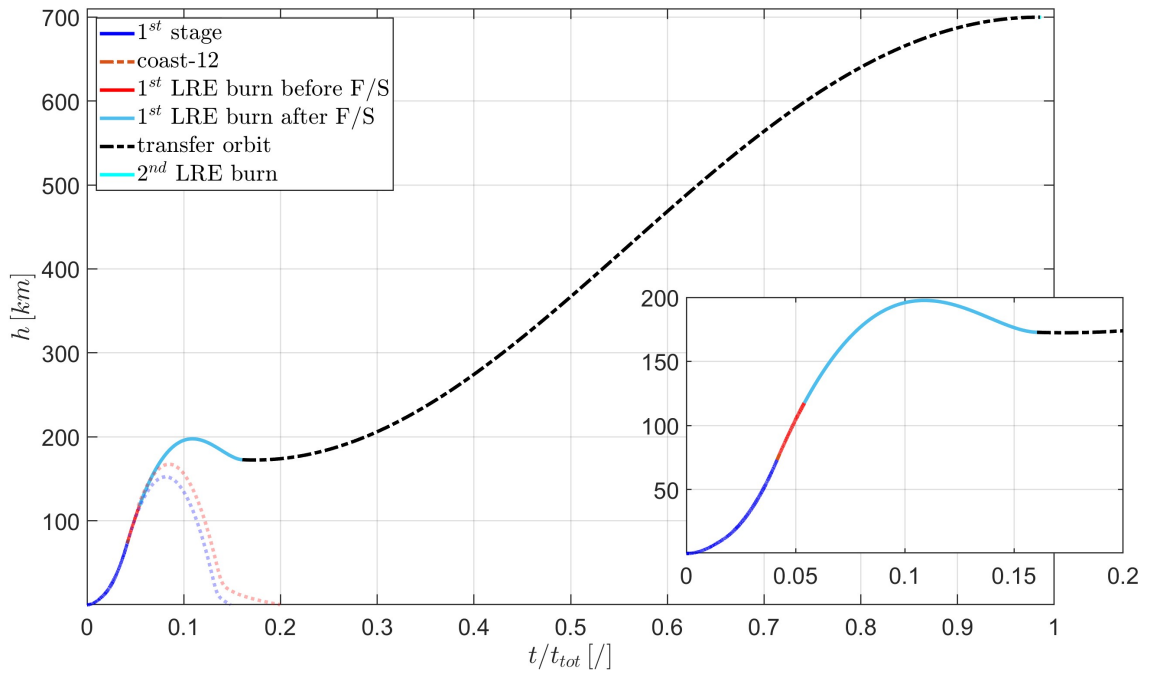


Figure 3.40: Altitude history TSTO.

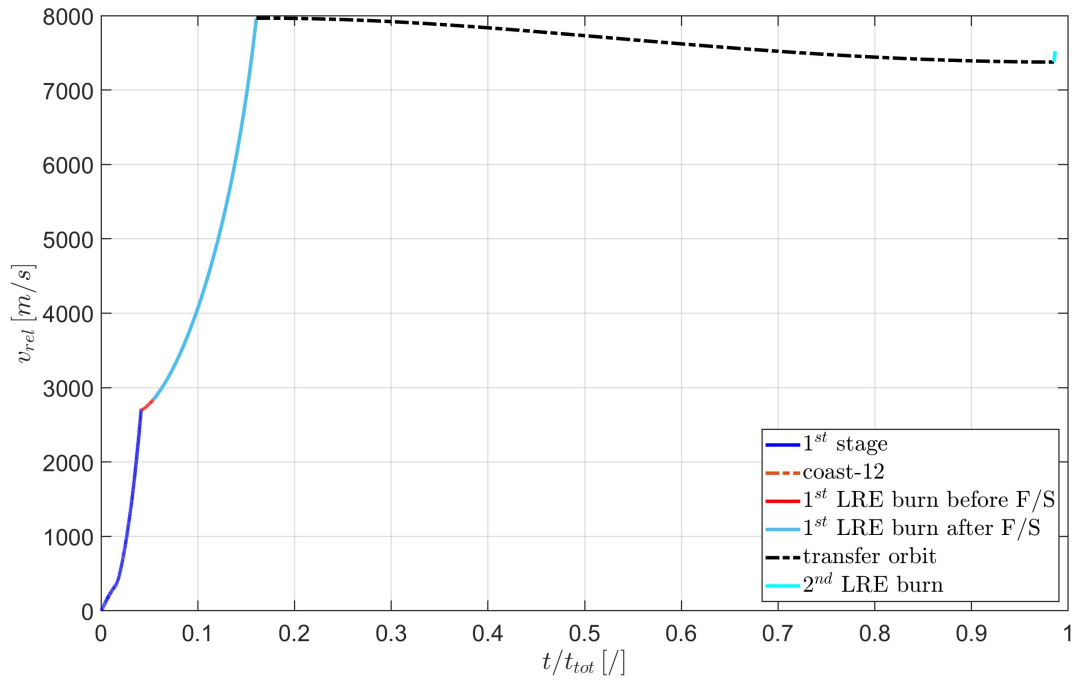


Figure 3.41: Relative speed TSTO.

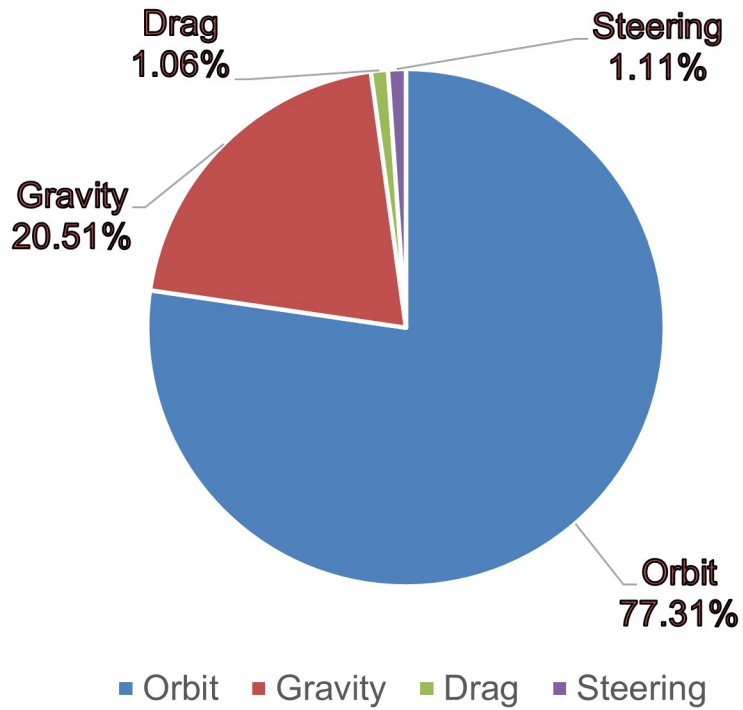
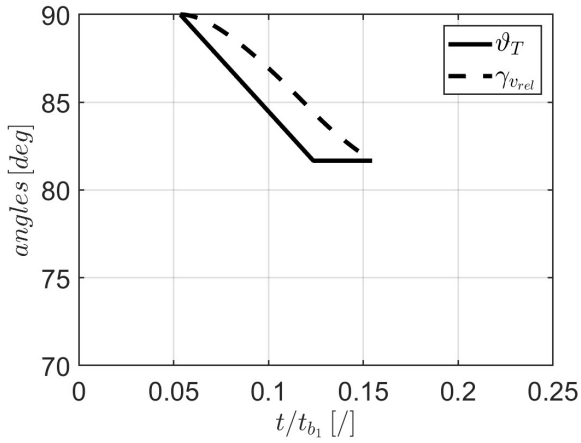
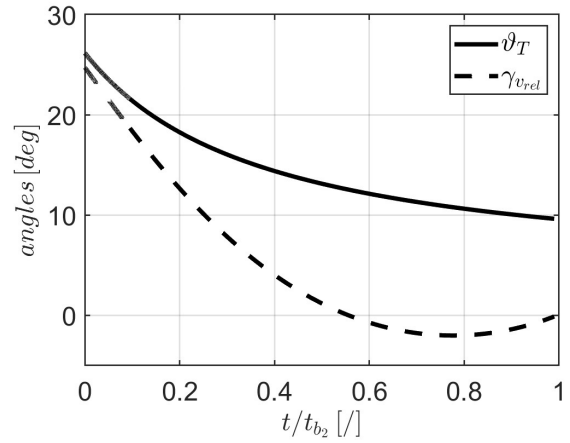
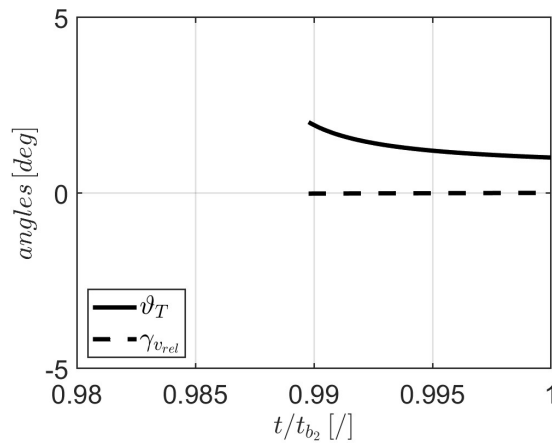


Figure 3.42: Mission velocity partition TSTO.

Table 3.9: Optimal TSTO configuration.

Parameter	Unit	Value
1 st stage diameter	<i>m</i>	2.6
1 st stage propellant	<i>kg</i>	56155
1 st stage inert	<i>kg</i>	4645
2 nd stage diameter	<i>m</i>	2.6
2 nd stage propellant	<i>kg</i>	11798
2 nd stage inert	<i>kg</i>	1112
Fairing diameter	<i>m</i>	2.6
Fairing mass	<i>kg</i>	600
Payload mass	<i>kg</i>	1331
Total mass	<i>kg</i>	75641
Total length	<i>m</i>	27.3

(a) 1st stage maneuver(b) 2nd stage 1st burn maneuver(c) 3rd stage maneuver**Figure 3.43:** LREs maneuver TSTO.

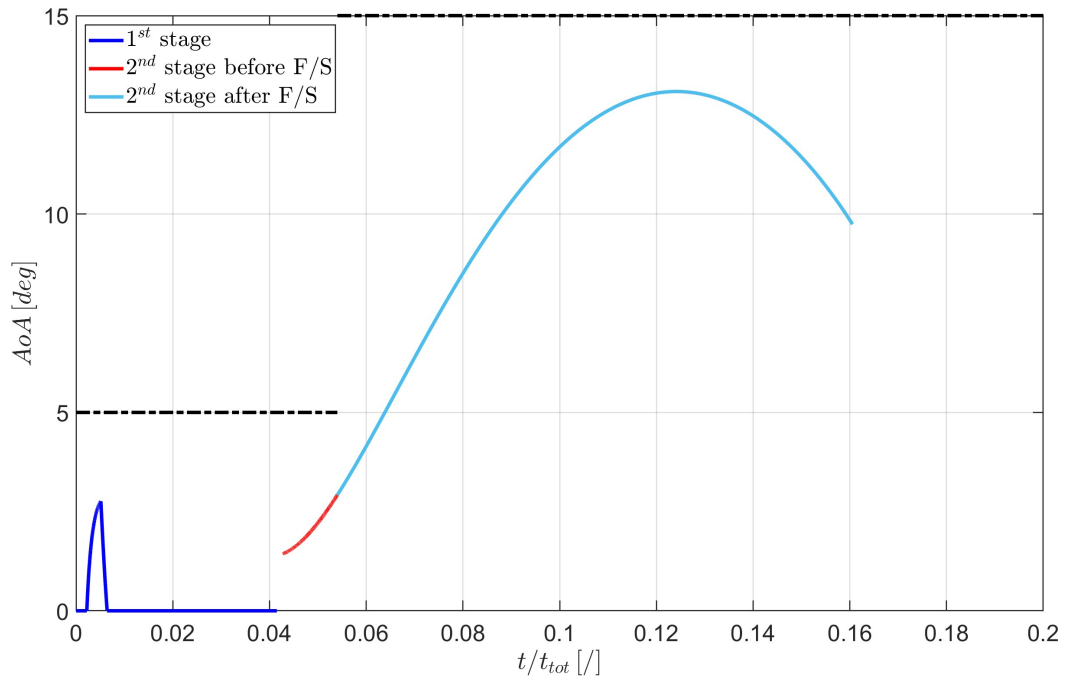


Figure 3.44: Angle of attack TSTO.

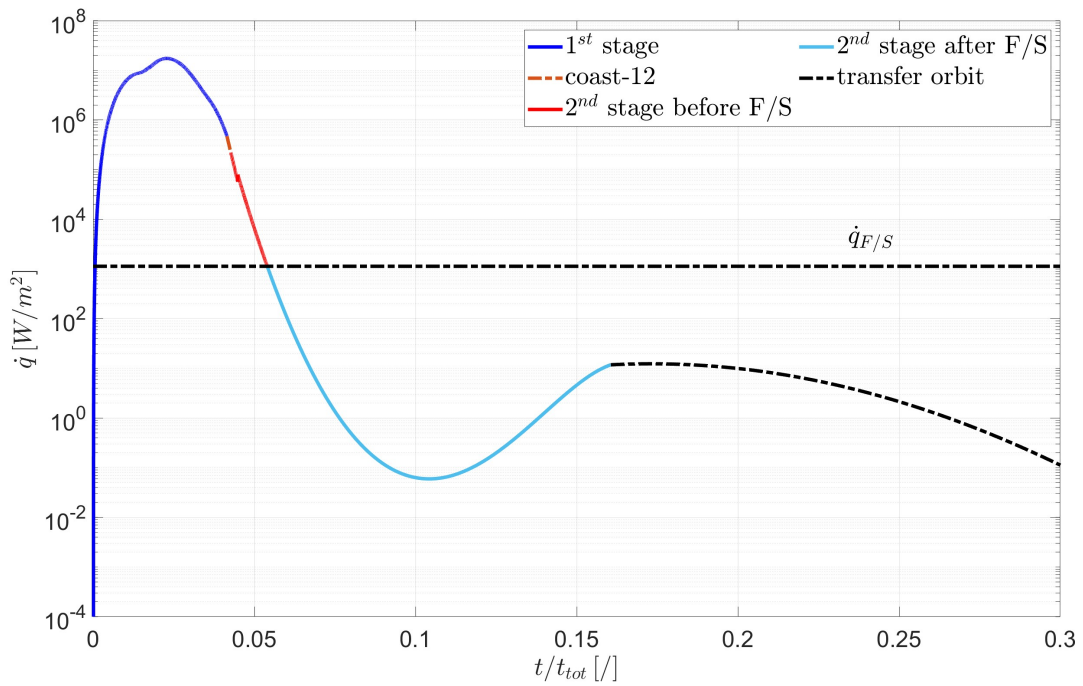


Figure 3.45: Aero-thermal heat flux TSTO.

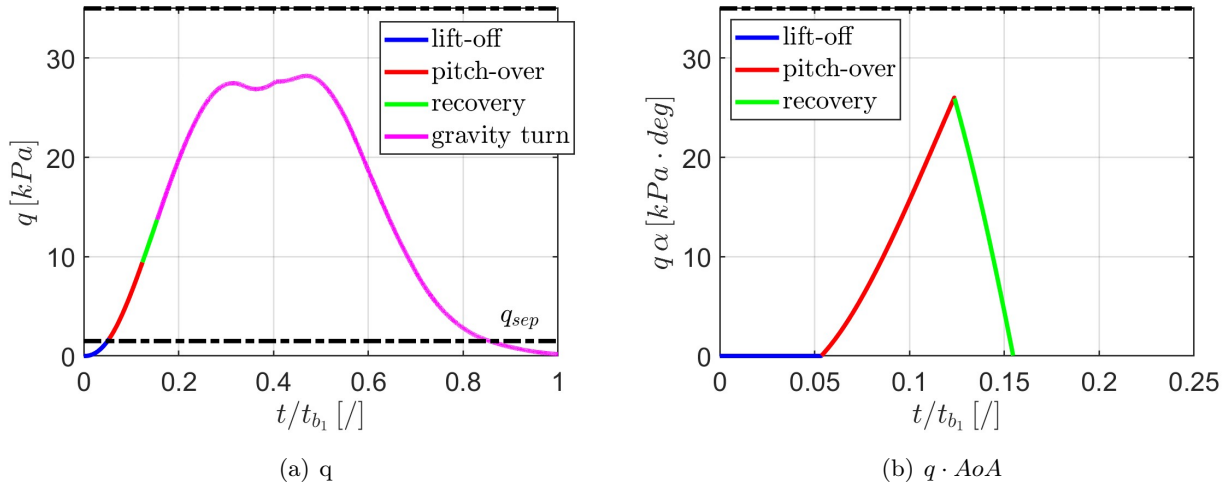


Figure 3.46: Dynamic pressure and $q \cdot AoA$ TSTO.

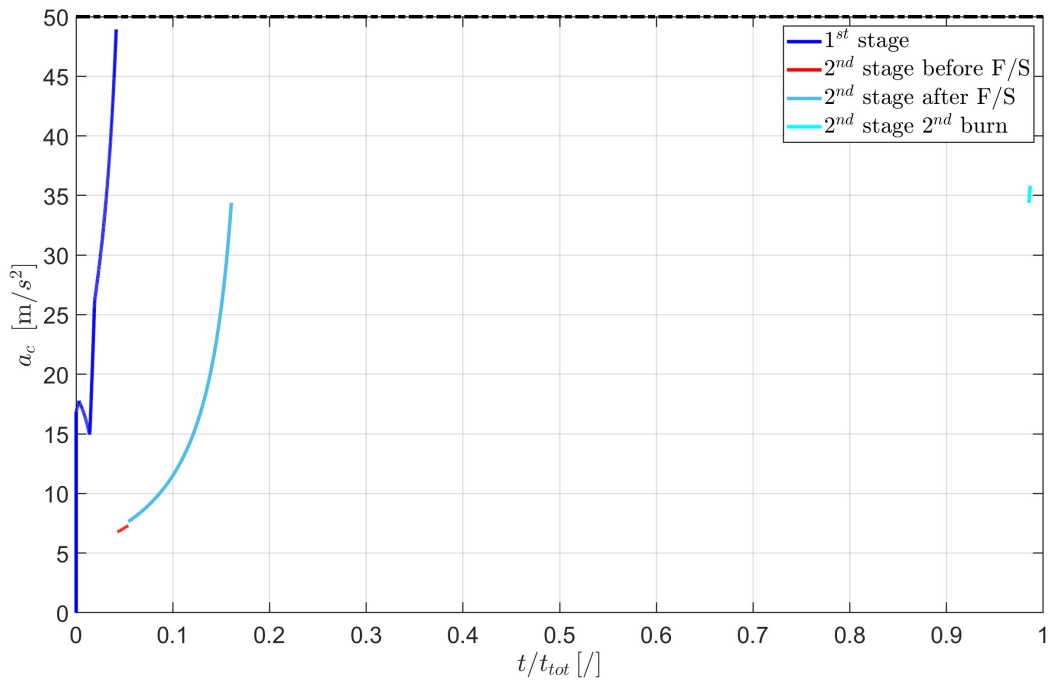


Figure 3.47: Acceleration TSTO.

The acceleration induced to payload presents a maximum just below the threshold of 50 m/s^2 at the end of first stage flight. Instead for the second stage the maximum is 35 m/s^2 . As it can be seen in Fig. 3.47 the acceleration trend of stage 2 is monotonically increasing due to the constant thrust level of LRE. The ground track of the mission is displayed in Fig. 3.48: the first stage and the fairing fall in the Atlantic ocean, the circularization burn of the second stage occurs close to the south coast of Australia. After the payload releasing a re-entry maneuver must be performed to de-orbit the second stage.

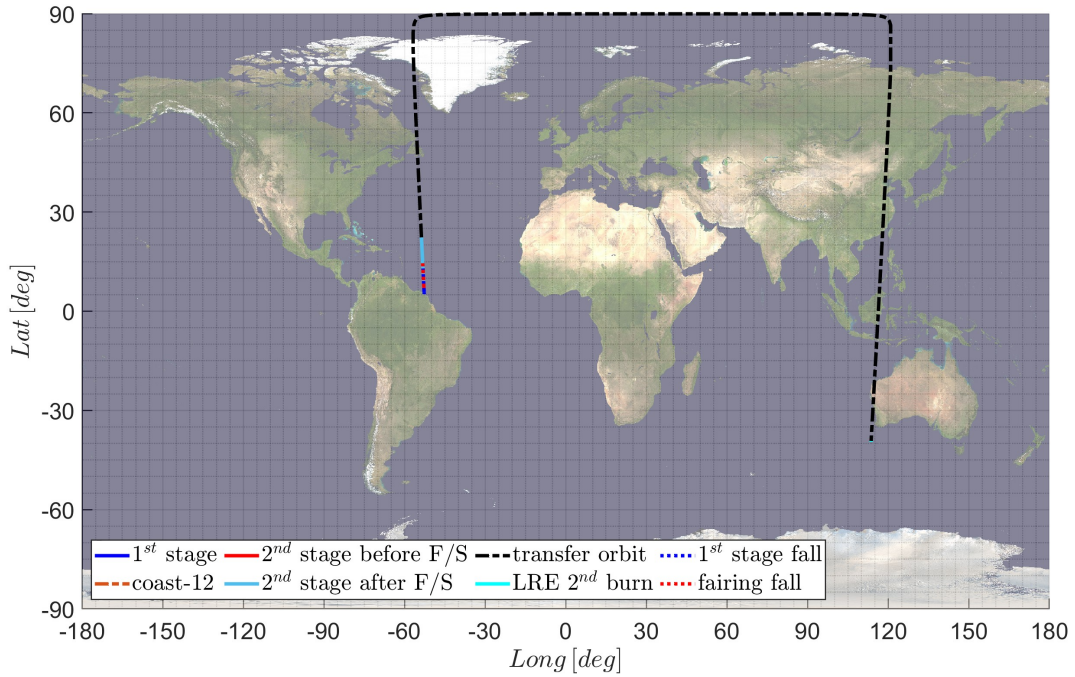


Figure 3.48: Ground track TSTO.

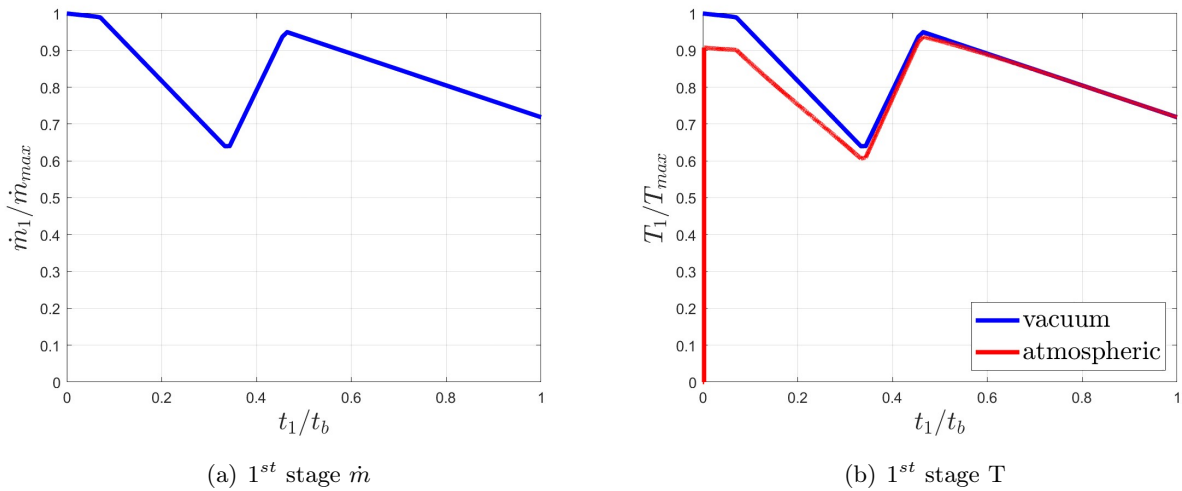


Figure 3.49: 1st stage mass flow rate and thrust TSTO.

The thrust of the second stage is constant, while the one of the first stage presents the shape displayed in Fig. 3.49. This shape resembles that of a solid rocket motor and the main purpose is to meet the constraints of maximum dynamic pressure and static controllability. In Fig. 3.49(b) can be noticed that the atmospheric thrust at lift-off is 10% less than the vacuum one.

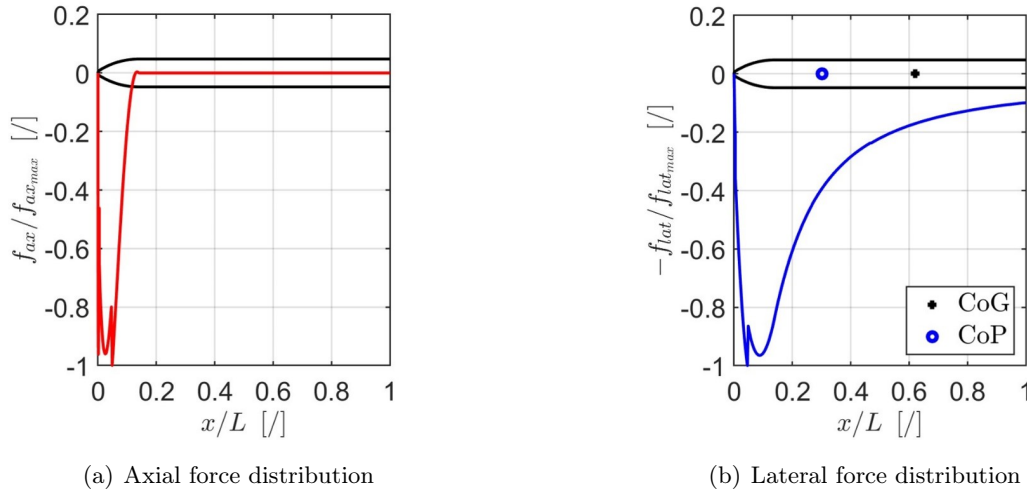


Figure 3.50: Aerodynamic forces distribution at q_{max} ($Mach = 1.80$) TSTO.

The considered load case is maximum dynamic pressure with an $AoA = 6\ deg$. The corresponding aerodynamic force distribution is shown in Fig. 3.50. The axial force is concentrated just in the front of the fairing, as the LV is isodiametric (see Fig.3.50(a)).¹ Also the lateral force distribution (see Fig. 3.50(b)) presents its peak just on the fairing; the resulting center of pressure is located around 30% from the nose tip.

The structural model of the LV is exhibited in Fig. 3.51. The model is composed by both one and two dimensional elements. The first stage is made of two tanks separated by an intertank, while the second stage presents a common bulckhead configuration. The tanks, the intertank and the interstage have a different number of reinforcement to increase the their stiffness. In particular the tanks of the first stage have respectively 17 and 43 stringers with a thickness of 13.1 mm and 8.3 mm, while the tanks of the second stage have both 63 reinforcements with a thickness of 9.8 mm and 17.2 mm. As regards the static analysis (see Fig. 3.52), maximum stress occurs at the first stage thrust skirt, due to the side thrust. Besides, the deformed configuration is influenced by the pressure inside the tanks. Instead, as concern the buckling analysis (see Fig. 3.53), the component more subjected to buckling failure is the upper skirt of the first stage first tank. The buckling load multiplier is equal to 2.53. This value is safely above the limit of 1.5, however it suggest that the found solution is most likely a local optimum from a structural point of view. Therefore further genetic algorithm generations are necessary to improve the found solution.

The optimal configuration is resumed in Tab. 3.9. The payload mass and the lift-off mass are respectively 7.02% and 45.13% less than the VEGA ones.

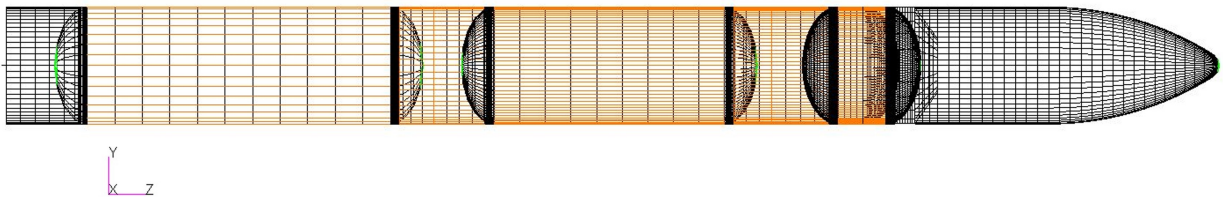


Figure 3.51: FEM geometry at q_{max} TSTO.

¹Examining Fig. 3.50(a), it is evident that skin friction drag is excluded from the axial force distribution in the supersonic regime. However, it is considered in the determination of C_D in subsonic regime as explained in Sec. 2.5.

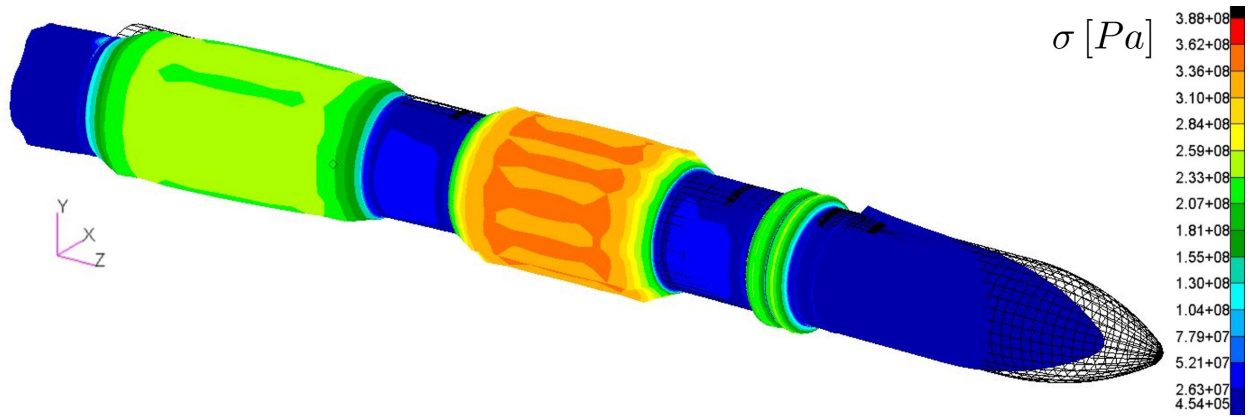


Figure 3.52: Static stress tensor at q_{max} TSTO.

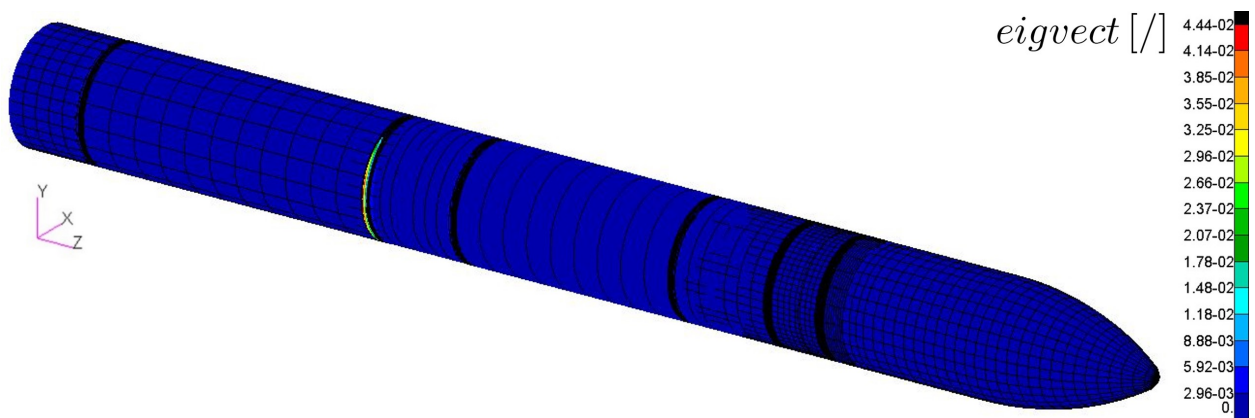


Figure 3.53: First buckling mode at q_{max} TSTO.

3.4 MDO computational aspects

Detailed computational information of all optimization cycles performed in this thesis is shown in Tab. 3.10. For every cycles are reported: the number of iterations, the computational time, the

Table 3.10: MDO computational cost.

Opt. cycle	Iter	Time	CPU	f	N	File	Surrogate
Structural opt. C1	5000	80 h	©Intel i7-4790K	4 GHz	1	.f06	0 %
Structural opt. C2	5000	40 h	©Intel i7-4790K	4 GHz	1	.f06	50 %
Structural opt. C3	5000	18 s	©Intel i7-4790K	4 GHz	1	.f06	100 %
VEGA inspired SO	30000	36 h	©AMD Ryzen 9 7950X	4.5 GHz	8	.h5	50 %
VEGA inspired MO	60000	72 h	©AMD Ryzen 9 7950X	4.5 GHz	8	.h5	50 %
TSTO MO	60000	120 h	©AMD Ryzen 9 7950X	4.5 GHz	8	.h5	0 %

CPU type, its frequency, the number of processors, the output file extension and the percentage of surrogate model. The computational time is influenced by all the other factors. Specifically, reading output from an .h5 file is faster than from an .f06 file, because in the .h5 file the data is organized as a structure, whereas the .f06 file is a text file. Undoubtedly, a reduction in computation time is achieved with an increase in both CPU frequency and the number of processors. the introduction of 50 % of functional evaluations through a surrogate FEM model allows for a halving of computation times. In conclusion, optimization of any one LV configuration takes a maximum of 5 days.

Conclusion and future remarks

In this PhD thesis is described and implemented a methodology to perform multidisciplinary design optimization of launch vehicle utilizing a high fidelity structural model and its surrogate. The disciplines considered for launch vehicle design are: orbital energy, propulsion, geometry & mass, aerodynamics, trajectory, and structure. The goal was to find the best launch vehicle configuration that maximizes payload mass and minimizes initial mass for a given target orbit. The design process begins by estimating the velocity losses needed to calculate the total mission velocity and thus the energy required to put the payload into orbit. Then the propulsion system is chosen, which can be solid- or liquid- based, and propellant, thrust and specific impulse are evaluated. By knowing the propulsion system and especially the propellant, the geometry and mass budget (and so the structural coefficients) of the launch vehicle are determined. At this point the layout of the launch vehicle is known, and with its profile, aerodynamic coefficients and dimensionless distributions of axial and lateral aerodynamic forces can be estimated. Knowing thrust, mass and aerodynamic characteristics, the trajectory is evaluated from lift-off to target orbit using a 3 DoF material point model. Of the whole mission, the dimensioning loadcase from the structural point of view is that of maximum dynamic pressure. Taking all the characteristics of the LV at this time instant, the FE model is created and the static and buckling analyses are performed. The optimization was performed using an external optimizer that changes the design variables to maximize and/or minimize the objective functions while respecting all the mission constraints. Thanks to the recent advance in computer science it was possible to perform FEM analysis since phase A of design, with a consequent increase of accuracy. Besides, the adoption of surrogate model permitted to reduce the computational time. Therefore, the introduction of high fidelity models inside a multi-disciplinary design optimization environment allows to drastically reduce the design time of new launch vehicles increasing the accuracy of the solution.

As regards the MDO architecture, between the ones found in literature, Asymmetrical Subspace Optimization (ASO) is the best choice, considering the introduction of the high fidelity structural model. Indeed, since the FEM solver requires a computational time that is one order of magnitude higher than the other disciplines; the introduction of the internal Lagrangian optimizer allows to exploit the higher computational speed of the propulsion and mass budget disciplines. Inside 1 iteration of the external optimizer the internal one performs around 30. In this way, the trajectory and the structural analysis can be performed on configuration that already presents an optimal staging, optimizing further the running time. Besides, the union of the disciplines of geometry and mass allows to have a structural mass which is equal to the FE model mass, avoiding a further internal loop between trajectory and structural analysis.


Commenting on the results, the increment of around 10% of payload mass with respect to the

real VEGA launch vehicle is due to a combination of effects: the visibility constraints have been not considered inside the trajectory analysis (the introduction of these constraints implies a higher perigee of the transfer orbit with a consequent increase of gravity losses and so decrement of payload mass); the lack of the GNC model and its discipline's constraints inside the optimization loop (for instance, the static controllability is verified just at maximum dynamic pressure time instant, instead it should be verified for the entire first stage flight). Another effect is the stage separation, it was supposed that all the interstage mass remains attached to the lower stage, in reality a part of the interstage stay attached to the upper stage. The last motivation of the higher payload mass is the power of the MDO: the coupling of all the disciplines is such as to find satisfying design variables which represents the best overall trade off. A proof of this are the values of the diameters respectively 2.8 m for first stage and 2 m for the upper stages. These values determines a reduction of 27% of restriction factor with a consequent benefit in terms of lower aerodynamic loads. Besides, the selected nozzle expansion ratios rely inside their range and are not set on their maximum value (as should be the ideal optimal from a propulsion point of view). Thus, the interstage dimension is lower and consequently their structural mass. Another aspect is the thrust shape that is linked directly with the trajectory optimization, bonding the first stage maneuver with the maximum thrust, that is linked with the maximum pressure, which determines the thickness of the SRM case impacting of the LV mass. In the MDO environment everything is connected. Only the solution of the genetic is left to chance, which can be a local optimum and not a global optimum given the finite number of generations of the algorithm and the vastness of the solution space. As for the liquid propulsion-based LV, the solution obtained indicates the possibility of using the input engine data to carry the 93% of the payload of the VEGA LV into orbit. With an opportune control law for the mass flow rate of the first stage, this constant diameter configuration can be made controllable even without the use of aerodynamic fins. Thus, multi disciplinary design optimization should be used a support for the single discipline specialist in order to start by a first attempt configurations that respect all the constraints of the other disciplines. Moreover, the idea that a complex system as a launch vehicle can be designed just *pressing the enter button* of a computer program is not true. The LV design is made neither by the machine, neither by the artificial intelligence. The design of a launch vehicle using the MDO is made by the human system engineer that creates the MDO architecture, sets the correct lower and upper bounds for every design variable, chooses the Design of Experiments, chooses the constraints of every discipline and sets the hyper parameters of the optimizers. Besides, also the job of the specialized engineers remains of paramount importance, as in the other phases of the design cycle every discipline needs to be verified by a high fidelity model.

Future developments

The MDO methodology implemented in this thesis has been thought in a modular way, in order to easily improve it. The topic is very large, spacing from engineering to pure mathematics thus hereunder are listed just part of the possible future developments. Therefore, improvements of this methodology can be achieved acting on two different plains: the engineering and the mathematical one. As regards the engineering prospective, every discipline "*black box*" can be improved or new ones can be added in the optimization architecture.

- The propulsion system can be enhanced considering: solid rocket motor grain geometry, in

this way the optimizer can act directly on the propellant grain shape to obtain the thrust ( $\rightarrow S_b \rightarrow p_c \rightarrow T$); more realistic control law for liquid rocket mass flow rate, model for hybrid rocket propulsion.

- The aerodynamic "*black box*" can be improved by substituting the analytic aerodynamic model with a surrogate one based on CFD analysis, as described in App. C. In this way, will be solved the problem of the pressure coefficient overestimation of the analytic method in transonic regime and the accuracy of CoP determination will increase not impacting the computational time.
- The trajectory model can be updated by introducing the controlled descent phase of the stages in order to consider re-usable launch vehicle configurations. The first stage maneuver can also be modified allowing a nonzero angle of attack instead of the pure gravity turn after the pitch over.
- In the structural model, new components can be inserted, for instance: the LRE combustion chamber, different typologies of thrust skirt, aerodynamic breakers and landing legs for re-usable LV configurations. Moreover, the material type can be added as a design variable, thus including other materials such as titanium alloy. Besides, hybrid rocket tanks can be created by connecting the existing LRE tank and SRM case. Regarding the applied forces, the sloshing can be modeled inside the liquid tanks via equivalent mechanical models.
- The GNC discipline can be developed and integrated inside the MDO architecture in an advanced LV development phase. In this way it will be possible to design a realistic TVC system of a flexible launch vehicle in order to ensure dynamic controllability. To do this is necessary to consider the combined effects of the modes of vibrations, aerodynamic loads and sloshing in case of liquid based LV. Moreover a wind profile model is needed to correctly evaluate the angle of attack due to lateral gust along all the duration of first stage flight.
- Through the insertion of a thermal analysis the mass of the insulation can be evaluated based on the physics of the considered phenomena, increasing the accuracy with respect to the mass estimation relationships.
- Another black box to add is the one related to the cost model of the LV, which will be considered as a further objective.

From a mathematical point of view new algorithms and optimization strategies can be adopted.

- In particular, the surrogate FEM model, which is trained on a suitable dataset before the optimization cycle, can be updated during the optimization process. For example, after the completion of a generation, the best designs can be inserted into the initial dataset to update the training of the virtual model, which, in this way adapts and evolves toward the optimal solution.
- The introduction of the statistical uncertainties of every design variable will allow to perform robust MDO, in which a solution less subjected to parameters fluctuation will be found.
- The constraints aggregation technique should be exploited to reduce the number of constraints and so to reduce the computational time.

Bibliography

- [1] Walter Edward Hammond. *Design methodologies for space transportation systems*. AIAA, 2001.
- [2] L Mancini, A Neri, E Cavallini, D Barbagallo, T Fossati, and F Serraglia. Optimal design of a first stage srm for a class of vega light vehicles. In *Proceedings of 6th Space Propulsion, Seville, Spain*, 2018.
- [3] Lorenzo Federici, Alessandro Zavoli, Guido Colasurdo, Lucandrea Mancini, and Agostino Neri. Integrated optimization of first-stage srm and ascent trajectory of multistage launch vehicles. *Journal of Spacecraft and Rockets*, 58(3):786–797, 2021.
- [4] Jahangir Jodei, Masoud Ebrahimi, and Jafar Roshanian. Multidisciplinary design optimization of a small solid propellant launch vehicle using system sensitivity analysis. *Structural and Multidisciplinary Optimization*, 38(1):93–100, 2009.
- [5] Francesco Castellini. *Multidisciplinary design optimization for expendable launch vehicles*. Ph.d. thesis, Polytechnic University of Milan, 2012.
- [6] Mathieu Balesdent, Nicolas Bérend, Philippe Dépincé, and Abdelhamid Chriette. A survey of multidisciplinary design optimization methods in launch vehicle design. *Structural and Multidisciplinary Optimization*, 45(5):619–642, 2012.
- [7] Ezgi Civek Coskun. Multistage launch vehicle design with thrust profile and trajectory optimization. *Middle East Technical University, PhD Thesis*, 2014.
- [8] Loic Brevault, Mathieu Balesdent, and Ali Hebbal. Multi-objective multidisciplinary design optimization approach for partially reusable launch vehicle design. *Journal of Spacecraft and Rockets*, 57(2):373–390, 2020.
- [9] Kai Dresia, Simon Jentzsch, Günther Waxenegger-Wilfing, Robson Dos Santos Hahn, Jan Deeken, Michael Oswald, and Fabio Mota. Multidisciplinary design optimization of reusable launch vehicles for different propellants and objectives. *Journal of Spacecraft and Rockets*, 58(4):1017–1029, 2021.
- [10] Martin Delavenne, Bernard Barriety, Fabio Vetrano, Valerie Ferrand, and Michel Salaun. Surrogate-based optimization of a morphing winglet for flexible aircraft. In *International Forum on Aeroelasticity and Structural Dynamics, Savannah, GE*, 2019.

- [11] Lucandrea Mancini, Leandro Lucchese, Francesco Saltari, Franco Mastroddi, and Agostino Neri. Surrogate finite-element modelling for launch vehicle multidisciplinary optimization. In *AIAA SCITECH 2022 Forum*, page 2443, 2022.
- [12] John Henry Holland et al. *Adaptation in natural and artificial systems: an introductory analysis with applications to biology, control, and artificial intelligence*. MIT press, 1992.
- [13] David E Goldberg and John Henry Holland. *Genetic algorithms and machine learning*. Kluwer Academic Publishers-Plenum Publishers; Kluwer Academic Publishers . . . , 1988.
- [14] Michael D McKay, Richard J Beckman, and William J Conover. A comparison of three methods for selecting values of input variables in the analysis of output from a computer code. *Technometrics*, 42(1):55–61, 2000.
- [15] Magnus R Hestenes. Multiplier and gradient methods. *Journal of optimization theory and applications*, 4(5):303–320, 1969.
- [16] J Stoer. Foundations of recursive quadratic programming methods for solving nonlinear programs. *Computational Mathematical Programming*, 15, 1985.
- [17] Joseph-Louis Lagrange. *Mécanique analytique*. La Haye, Veuve Desaint, Paris, 1788.
- [18] RH Goddard. A method of reaching extreme altitudes. *Smithsonian Miscellaneous Collections*, 71(2), 1919.
- [19] Hermann Oberth. *Die Rakete zu den Planetenräumen*. Oldenbourg Wissenschaftsverlag, 1984.
- [20] Walter Hohmann. The attainability of heavenly bodies. Technical Report NASA TT F-44, National Aeronautics and Space Administration, 1960.
- [21] Frank J Malina and Martin Summerfield. The problem of escape from the earth by rocket. *Journal of the Aeronautical Sciences*, 14(8):471–480, 1947.
- [22] M Vertregt. Calculation of step-rockets. In *Bericht über den V. Internationalen Astronautischen Kongreß: Innsbruck, 5. bis 7. August 1954*, pages 157–161. Springer, 1955.
- [23] Martin Goldsmith. On the optimization of two-stage rockets. *Journal of Jet Propulsion*, 27(4):415–428, 1957.
- [24] HH Hall and ED Zambelli. On the optimization of multistage rockets. *Journal of Jet Propulsion*, 28(7):463–465, 1958.
- [25] Lucien A Schmit. Structural design by systematic synthesis. In *Proceedings of the Second National Conference on Electronic Computation, ASCE, Sept., 1960*, 1960.
- [26] L Berke and NS Khot. *Use of optimality criteria methods for large scale systems*. Air Force Flight Dynamics Laboratory, 1974.
- [27] NS Khot, VB Venkayya, and L Berke. Experiences with minimum weight design of structures using optimality criteria methods. *SAE Transactions*, pages 2244–2254, 1977.

- [28] Theodor Von Kármán, Ernest E Sechler, and LH Donnell. The strength of thin plates in compression. *Transactions of the American Society of Mechanical Engineers*, 54(2):53–56, 1932.
- [29] Jaroslaw Sobieszczanski-Sobieski. A linear decomposition method for large optimization problems. Technical Report TM 83248, NASA, 1982.
- [30] Jaroslaw Sobieszczanski-Sobieski and Jean-Francois M Barthelemy. Improving engineering system design by formal decomposition, sensitivity analysis, and optimization. In *Proceedings of International Conference of Engineering Design, Hamburg, West Germany*, 1985.
- [31] Jaroslaw Sobieszczanski-Sobieski. Optimization by decomposition: a step from hierarchic to non-hierarchic systems. In *Second NASA/Air Force Symposium on Recent Advances in Multidisciplinary Analysis and Optimization, Hampton, VA, NASA CP*, volume 3031, pages 51–78, 1988.
- [32] Robert David Braun. *Collaborative optimization: an architecture for large-scale distributed design*. Stanford University, 1996.
- [33] Jaroslaw Sobieszczanski-Sobieski, Jeremy Agte, and Robert Sandusky, Jr. Bi-level integrated system synthesis (bliss). In *7th AIAA/USAF/NASA/ISSMO Symposium on Multidisciplinary Analysis and Optimization*, page 4916, 1998.
- [34] S Kodiyalam, RJ Yang, L Gu, and C-H Tho. Multidisciplinary design optimization of a vehicle system in a scalable, high performance computing environment. *Structural and Multidisciplinary Optimization*, 26:256–263, 2004.
- [35] Yuping He and John McPhee. Multidisciplinary design optimization of mechatronic vehicles with active suspensions. *Journal of Sound and Vibration*, 283(1-2):217–241, 2005.
- [36] Cyrus D Jilla, David W Miller, and Raymond J Sedwick. Application of multidisciplinary design optimization techniques to distributed satellite systems. *Journal of Spacecraft and Rockets*, 37(4):481–490, 2000.
- [37] E Riddle Taylor. Evaluation of multidisciplinary design optimization techniques as applied to spacecraft design. In *2000 IEEE Aerospace Conference. Proceedings (Cat. No. 00TH8484)*, volume 1, pages 371–384. IEEE, 2000.
- [38] Daniele Peri and Emilio F Campana. Multidisciplinary design optimization of a naval surface combatant. *Journal of Ship Research*, 47(01):1–12, 2003.
- [39] SS Talya, Aditi Chattopadhyay, and JN Rajadas. Multidisciplinary design optimization procedure for improved design of a cooled gas turbine blade. *Engineering Optimization*, 34(2): 175–194, 2002.
- [40] Timothy W Simpson, Timothy M Mauery, John J Korte, and Farrokh Mistree. Kriging models for global approximation in simulation-based multidisciplinary design optimization. *AIAA journal*, 39(12):2233–2241, 2001.

- [41] RD Braun, RW Powell, RA Lepsch, DO Stanley, and IM Kroo. Comparison of two multidisciplinary optimization strategies for launch-vehicle design. *Journal of Spacecraft and Rockets*, 32(3):404–410, 1995.
- [42] R Braun, A Moore, and I Kroo. Use of the collaborative optimization architecture for launch vehicle design. In *6th Symposium on Multidisciplinary Analysis and Optimization*, page 4018, 1996.
- [43] Robert D Braun, Arlene A Moore, and Ilan M Kroo. Collaborative approach to launch vehicle design. *Journal of spacecraft and rockets*, 34(4):478–486, 1997.
- [44] Laura A Ledsinger and John R Olds. Optimized solutions for kistler k-1 branching trajectories using multidisciplinary design optimization techniques. *Journal of Spacecraft and Rockets*, 39(3):420–429, 2002.
- [45] Saqlain Akhtar and He Linshu. Support vector regression-driven multidisciplinary design optimization for multi-stage space launch vehicle considering throttling effect. In *44th AIAA aerospace sciences meeting and exhibit*, page 341, 2006.
- [46] Douglas J Bayley, Roy J Hartfield Jr, John E Burkhalter, and Rhonald M Jenkins. Design optimization of a space launch vehicle using a genetic algorithm. *Journal of Spacecraft and Rockets*, 45(4):733–740, 2008.
- [47] Masoud Ebrahimi, Mohammad Reza Farmani, and Jafar Roshanian. Multidisciplinary design of a small satellite launch vehicle using particle swarm optimization. *Structural and Multidisciplinary Optimization*, 44:773–784, 2011.
- [48] MW Van Kesteren. Air launch versus ground launch: a multidisciplinary design optimization study of expendable launch vehicles on cost and performance. Master’s thesis, Delft University of Technology, 2013.
- [49] Jafar Roshanian and Masoud Ebrahimi. Latin hypercube sampling applied to reliability-based multidisciplinary design optimization of a launch vehicle. *Aerospace Science and Technology*, 28(1):297–304, 2013.
- [50] Francesco Castellini, Annalisa Riccardi, Michèle Lavagna, and Christof Büskens. Global and local multidisciplinary design optimization of expendable launch vehicles. In *52nd AIAA/ASME/ASCE/AHS/ASC Structures, Structural Dynamics and Materials Conference 19th AIAA/ASME/AHS Adaptive Structures Conference 13t*, page 1901, 2011.
- [51] Loïc Brevault. *Contributions to multidisciplinary design optimization under uncertainty, application to launch vehicle design*. PhD thesis, Ecole Nationale Supérieure des Mines de Saint-Etienne, 2015.
- [52] Loïc Brevault, Mathieu Balesdent, Ali Hebbal, and Antoine Patureau De Mirand. Surrogate model-based multi-objective mdo approach for partially reusable launch vehicle design. In *AIAA Scitech 2019 Forum*, page 0704, 2019.

- [53] Mathieu Balesdent, Nicolas Bérend, and Philippe Dépincé. Optimal design of expendable launch vehicles using stage-wise mdo formulation. In *13th AIAA/ISSMO multidisciplinary analysis optimization conference*, page 9324, 2010.
- [54] MSC NASTRAN. *Quick Reference Guide*. MSC Software Corporation, 2018.
- [55] Joaquim RRA Martins and Andrew B Lambe. Multidisciplinary design optimization: a survey of architectures. *AIAA journal*, 51(9):2049–2075, 2013.
- [56] Vilfredo Pareto. *Manuale di economia politica: con una introduzione alla scienza sociale*, volume 13. Società editrice libraria, 1919.
- [57] Ronald Aylmer Fisher. Design of experiments. *British Medical Journal*, 1(3923):554, 1936.
- [58] John Von Neumann. Various techniques used in connection with random digits. *John von Neumann, Collected Works*, 5:768–770, 1963.
- [59] Il'ya Meerovich Sobol'. On the distribution of points in a cube and the approximate evaluation of integrals. *Zhurnal Vychislitel'noi Matematiki i Matematicheskoi Fiziki*, 7(4):784–802, 1967.
- [60] Thomas H Cormen, Charles E Leiserson, Ronald L Rivest, and Clifford Stein. *Introduction to algorithms*. MIT press, 2022.
- [61] Frank Yates. *The design and analysis of factorial experiments*. Imperial Bureau of Soil Science, 1937.
- [62] Genichi Taguchi, Subir Chowdhury, and Yui Wu. *Taguchi's quality engineering handbook*. John Wiley & Sons, Inc., 2004.
- [63] Jasbir Singh Arora. *Introduction to optimum design*. Elsevier, 2004.
- [64] Matthias Ehrgott. *Multicriteria optimization*, volume 491. Springer Science & Business Media, 2005.
- [65] Colin Reeves and Jonathan E Rowe. *Genetic algorithms: principles and perspectives: a guide to GA theory*, volume 20. Springer Science & Business Media, 2002.
- [66] Silvia Poles. Moga-ii an improved multi-objective genetic algorithm. *Estecotechnical Report*, 6, 2003.
- [67] Stefania Gemma and Franco Mastroddi. Multi-disciplinary and multi-objective optimization of an unconventional aircraft concept. In *16th AIAA/ISSMO Multidisciplinary Analysis and Optimization Conference*, page 2327, 2015.
- [68] Stefania Gemma and Franco Mastroddi. Multi-disciplinary and multi-objective optimization of an over-wing-nacelle aircraft concept. *CEAS Aeronautical Journal*, 10(3):771–793, 2019.
- [69] Claude Lemaréchal. Cauchy and the gradient method. *Doc Math Extra*, 251(254):10, 2012.
- [70] Haskell B Curry. The method of steepest descent for non-linear minimization problems. *Quarterly of Applied Mathematics*, 2(3):258–261, 1944.

- [71] Konstantin Eduardovich Tsiolkovsky. Exploration of the universe with reaction machines. *The Science Review*, 5, 1903.
- [72] Wiley J Larson, Gary N Henry, and Ronald W Humble. *Space propulsion analysis and design*. McGraw-Hill, 1995.
- [73] Enrico Cavallini, Bernardo Favini, and Agostino Neri. Vega solid stages performance analysis: Static firing tests and flights. In *6th European Conference for Aerospace Science*, 2015.
- [74] Ed Casillas. System engineering & trades large srm space launch booster applications. In *AIAA 44th AIAA/ASMA/SAE/ASEE, Joint Propulsion Conference, Hartford CT*, 2008.
- [75] Enrico Cavallini, Bernardo Favini, and Agostino Neri. Analysis and performance reconstruction of vega solid rocket motors qualification flights. In *50th AIAA/ASME/SAE/ASEE Joint Propulsion Conference*, page 3805, 2014.
- [76] Lucandrea Mancini, Agostino Neri, and Enrico Cavallini. Uncertainty-dispersion analysis of srm performance prediction & reconstruction. In *AIAA Propulsion and Energy 2021 Forum*, page 3705, 2021.
- [77] Enrico Cavallini, Bernardo Favini, and Agostino Neri. Effective semi-empirical model of nozzle thermo-chemical erosion in solid rocket motors. In *53rd AIAA/SAE/ASEE Joint Propulsion Conference*, page 4780, 2017.
- [78] Sanford Gordon and Bonnie J McBride. Computer program for calculation of complex chemical equilibrium compositions and applications: Part i analysis. *NASA reference publication*, 1311, 1994.
- [79] BJ McBride and S Gordon. Computer program for calculation of complex chemical equilibrium compositions and applications: Part ii user manual and program description. *NASA reference publication*, 1311, 1996.
- [80] George P Sutton and Oscar Biblarz. *Rocket propulsion elements*. John Wiley & Sons, 2016.
- [81] Dieter K Huzel. *Modern engineering for design of liquid-propellant rocket engines*, volume 147. American Institute of Aeronautics and Astronautics, Inc., 1992.
- [82] William M Marshall. *Experimental studies on combustion instabilities in a multi-element, rectangular rocket chamber*. The Pennsylvania State University, 2008.
- [83] R Cook and G Coffey. Space shuttle orbiter engine main combustion chamber cooling and life. In *9th Propulsion Conference*, page 1310, 1973.
- [84] DL Akin. Mass estimating relations", enae 791 – launch and entry vehicle design. University of Maryland, 2022. <https://spacecraft.ssl.umd.edu/academics/791S22/791S22L08.MERsx.pdf>.
- [85] Don Edberg and Willie Costa. *Design of Rockets and Space Launch Vehicles*. American Institute of Aeronautics and Astronautics, Inc., 2020.

- [86] R Rohrschneider. Development of a mass estimating relationship database for launch vehicle conceptual design. *AE8900 Special Project, School of Aerospace Engineering, Georgia Institute of Technology*, 2002.
- [87] Lester Lees. Hypersonic flow. In *Proceedings of the Fifth International Aeronautical Conference, Institute of the Aeronautical Sciences*, pages 241–76, 1955.
- [88] Nikolai F Krasnov. Aerodynamics of bodies of revolution. Technical report, RAND CORP SANTA MONICA CALIF, 1965.
- [89] Filippo Sabetta. *Gasdinamica*, volume 6. Sapienza Università Editrice, 2009.
- [90] Gerard WH Van Es. Rapid estimation of the zero-lift drag coefficient of transport aircraft. *Journal of aircraft*, 39(4):597–599, 2002.
- [91] Eugene L Fleeman. Tactical missile design, american institute of aeronautics and astronautics. *Inc., Reston, USA*, 2001.
- [92] Jeremy Rea. Launch vehicle trajectory optimization using a legendre pseudospectral method. In *AIAA guidance, navigation, and control conference and exhibit*, page 5640, 2003.
- [93] US Standard Atmosphere. *US standard atmosphere*. National Oceanic and Atmospheric Administration, 1976.
- [94] Mauro Pontani and Paolo Teofilatto. Simple method for performance evaluation of multistage rockets. *Acta Astronautica*, 94(1):434–445, 2014.
- [95] Robin Churchill. The 1982 united nations convention on the law of the sea. In Donald R. Rothwell, Alex G. Oude Elferink, Karen N. Scott, and Tim Stephens, editors, *Oxford handbook on the law of the sea*, pages 24–45. Oxford University Press, 2015.
- [96] WA Wagner. Liquid rocket metal tanks and tank components. Technical Report 8088, National Aeronautics and Space Administration, 1974.
- [97] Arianspace. *VEGA User’s Manual*, issue 4 revision 0 edition, 2014.
- [98] ESTECO SpA. *modeFRONTIER User’s manual*, 2022.
- [99] C Barret. Design of launch vehicle flight control augmentors and resulting flight stability and control. Technical Report 3704, NASA, 1997.
- [100] Cornelius T Leondes and Robert Willard Vance. *Lunar missions and exploration*. Wiley, 1964.
- [101] Martin D Buhmann. *Radial basis functions: theory and implementations*, volume 12. Cambridge university press, 2003.
- [102] Enrico Rigoni. Radial basis functions response surfaces. Technical Report 4, ESTECO modeFRONTIER, 2007.
- [103] T. Hastie, R. Tibshirani, and J. Friedman. *The Elements of Statistical Learning*. Springer, 2001.

- [104] Jerome H Friedman. Greedy function approximation: a gradient boosting machine. *Annals of statistics*, pages 1189–1232, 2001.
- [105] Steven G Ritz, Roy J Hartfield, Jeffrey A Dahlen, John E Burkhalter, and Walter S Woltosz. Rapid calculation of missile aerodynamic coefficients using artificial neural networks. In *2015 IEEE Aerospace Conference*, pages 1–19. IEEE, 2015.
- [106] Pin Wu, Wenyan Yuan, Lulu Ji, Ling Zhou, Zhu Zhou, Weibing Feng, and Yike Guo. Missile aerodynamic shape optimization design using deep neural networks. *Aerospace Science and Technology*, 126:107640, 2022.
- [107] Kumpati S Narendra and Kannan Parthasarathy. Learning automata approach to hierarchical multiobjective analysis. *IEEE Transactions on systems, man, and cybernetics*, 21(1):263–272, 1991.
- [108] Andrew R Barron. Universal approximation bounds for superpositions of a sigmoidal function. *IEEE Transactions on Information theory*, 39(3):930–945, 1993.

Appendix A

Lagrangian optimizer for staging

This appendix presents the Lagrangian optimizer devoted to find the optimal partition of Δv between the stages of a launch vehicle, given target payload and orbit.

The optimal staging problem can be solved via the Lagrangian multiplier method. Given an objective function $f(\mathbf{x})$ to minimize, subjected to equality constraints $h(\mathbf{x})$ where \mathbf{x} is the vector of design variables, it can be written the Lagrangian function, where μ is the vector of Lagrangian multipliers.

$$\mathcal{L}(\mathbf{x}, \mu) = f(\mathbf{x}) + \mu^T h(\mathbf{x}) \quad (\text{A.1})$$

Find a minimum which respect the constraint means that the gradient of the Lagrangian function must be equal to zero:

$$\nabla \mathcal{L}(\mathbf{x}, \mu) = 0 \quad (\text{A.2})$$

In this particular problem of optimal staging, given a LV with N stages, once defined the mass ratios MR_j (ratio between final m_f and initial m_0 mass) and the payload ratios λ_j (which depend on the structural coefficient k_{s_j}) for the j -th stage,

$$MR_j = \frac{m_{f_j}}{m_{0_j}} \quad (\text{A.3})$$

$$\lambda_j = \frac{MR_j - k_{s_j}}{1 - k_{s_j}} \quad (\text{A.4})$$

the function to minimize is the logarithm of the inverse of the total payload ratio, where m_{pl} is the payload mass.

$$f(MR_j) = \ln \left(\frac{m_0}{m_{pl}} \right) = \ln \left(\prod_{j=1}^N \frac{1}{\lambda_j} \right) = \sum_{j=1}^N \ln \left(\frac{1 - k_{s_j}}{MR_j - k_{s_j}} \right) \quad (\text{A.5})$$

The sum of ΔV of each stage (which depends on effective velocity c_j and k_{s_j}) must be equal to the total mission velocity.

$$h(MR_j) = \Delta V_{tot} + \sum_{j=1}^N c_j \ln(MR_j) = 0 \quad (\text{A.6})$$

For the upper stages the effective velocity is the vacuum one, instead for the first stage must be

taken a value between the sea level c_{sl} and vacuum c_{vac} , in fact, it is taken suggestion of Ref. [100]

$$c_{j>2} = c_{vac_{j>2}} \quad (\text{A.7})$$

$$c_1 = \frac{(c_{sl} + 2c_{vac_1})}{3} \quad (\text{A.8})$$

Thus, introducing the Lagrangian multiplier μ , the Lagrangian function for the optimal staging problem is:

$$\mathcal{L}(MR_j, \mu) = \sum_{j=1}^N \ln \left(\frac{1 - k_{s_j}}{MR_j - k_{s_j}} \right) + \mu \left[\Delta V_{tot} + \sum_{j=1}^N c_j \ln(MR_j) \right] \quad (\text{A.9})$$

By performing the derivative and imposing it equal to zero (Eq. (A.10)), it is obtained the optimal mass ratio function of the multiplier μ (Eq. (A.11)).

$$\frac{\partial \mathcal{L}(MR_j, \mu)}{\partial MR_j} = -\frac{1}{MR_j - k_{s_j}} + \mu \frac{c_j}{MR_j} = 0 \quad (\text{A.10})$$

$$MR_i = \frac{\mu c_i k_{s_i}}{\mu c_i - 1} \quad (\text{A.11})$$

At this point, in order to find the value of the Lagrangian multiplier, it is necessary to substitute the optimal mass ratio in Eq. (A.6), thus it is obtained the new function $g(\mu)$ (Eq. (A.12)), which must be equal to zero.

$$g(\mu) = \Delta V_{tot} + \sum_{j=1}^N c_j \ln \left(\frac{\mu c_j k_{s_j}}{\mu c_j - 1} \right) \quad (\text{A.12})$$

A possible way to find the zero is to implement Newton-Raphson method calculating the derivative of $g(\mu)$ (Eq. (A.13)) using the starting point μ_0 (Eq. (A.14)), where β_0 is 0.5; and continuing the procedure with the subsequent point μ_{k+1} (Eq. (A.15)),

$$g'(\mu) = -\sum_{j=1}^N \frac{\mu}{\mu(\mu c_j - 1)} \quad (\text{A.13})$$

$$\mu_0 = \max_i \left(\frac{\beta_0}{c_i(\beta_0 - k_{s_i})} \right) \quad (\text{A.14})$$

$$\mu_{k+1} = \mu_k - \alpha_\mu \frac{g'(\mu_k)}{g(\mu_k)} \quad (\text{A.15})$$

where α_μ is 1 or it is halved if μ_k is less than μ_0 .

Appendix B

Response Surface Models

This appendix presents the two RSM used to create the surrogate Finite Element model: Radial basis Functions and Gradient Boosting Machine.

B.1 Radial Basis Functions

The present section provides general details about RBFs, which are a powerful tool for data interpolation even considering training points that are not sampled on a regular grid. They are theoretically described in Ref. [101] and rely on the following approximation:

$$s(x) = \sum_{j=1}^n c_j \phi \left(\frac{\|x - x_j\|}{\delta} \right) \quad (\text{B.1})$$

where ϕ is the radial function, c_j are the free parameters of the model, and delta is the scaling parameter. The problem consists in the calculation of the unknown coefficient vector c

$$c = A^{-1}f \quad (\text{B.2})$$

where A is the collocation matrix and f is imposed equal to s according to the interpolation equations.

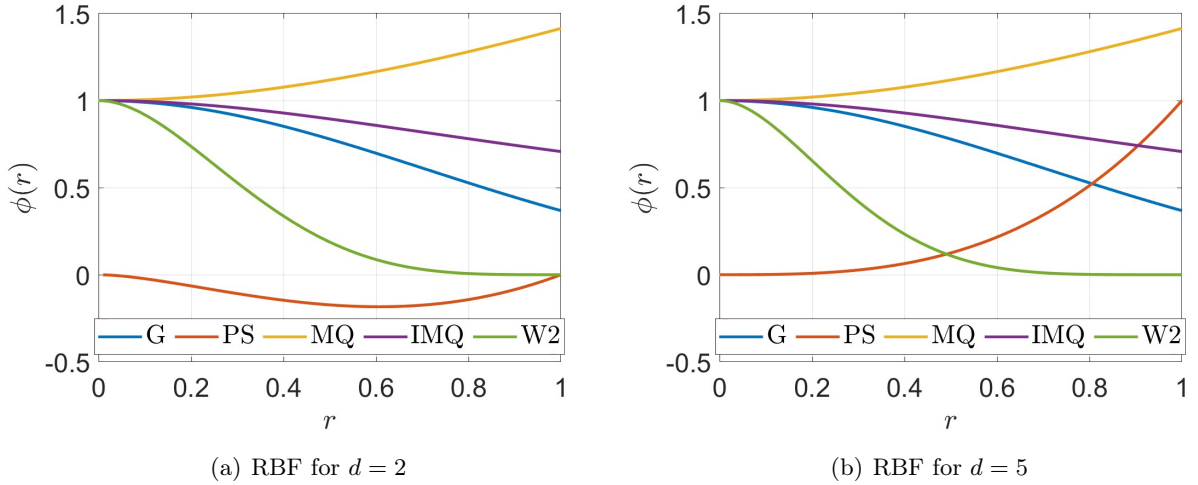
$$A_{ij} = \phi \left(\frac{\|x_i - x_j\|}{\delta} \right) \quad (\text{B.3})$$

$$f_i = s(x_i) \quad (\text{B.4})$$

The type of functions available in modeFRONTIER© which are listed in Tab. B.1 (see Ref. [102]) are Gaussian (G), Hardy's direct (MQ) and inverse (IMQ), Duchon's Polyharmonic Splines (PS) and Wendland's Compactly Supported C^2 (W2), as displayed in Fig. B.1.

Table B.1: Available RBFs (Ref. [102]).

Type	Function
G	$\phi(r) = e^{-r^2}$
PS	$\phi(r) = \begin{cases} r^3 & \text{if } d \text{ odd} \\ r^2 \log(r) & \text{if } d \text{ even} \end{cases}$
MQ	$\phi(r) = (1 + r^2)^{0.5}$
IMQ	$\phi(r) = (1 + r^2)^{-0.5}$
W2	$\phi(r) = \begin{cases} (1 - r)_+^3 (3r + 1) & \text{if } d = 1 \\ (1 - r)_+^4 (4r + 1) & \text{if } d = 2, 3 \\ (1 - r)_+^5 (5r + 1) & \text{if } d = 4, 5 \end{cases}$


Figure B.1: Radial basis functions plot.

B.2 Gradient Boosting Machine

Gradient boosting is a forward machine learning method which predicts the output based on progressive refined approximations. Given a generic dataset composed by N input rows (design samples) and n output rows $D = \{(x_i, y_i)\}_{i=1}^N$ and a differentiable loss function $L(y_i, f(x_i))$ where y_i are the observed values and $f(x_i)$ are the predicted ones. The algorithm described in Ref. [103] is composed by the following steps:

1. The first step consists in initializing the algorithm with a constant value:

$$f_0(x) = \arg \min_{\gamma} \sum_{i=1}^N L(y_i, \gamma) \quad (\text{B.5})$$

if the loss function is equal to $L(y_i, f(x)) = \frac{1}{2}(y_i - f(x))^2$, the value that minimizes the sum expressed in Eq. B.5 is the average of the observed values. Thus the initial value of the

algorithm is the same for every input vector, which means that they can be represented by a tree with just one leaf.

2. The second step consists in performing a loop to build all the m^{th} trees until M .

a) The loop starts by computing the pseudo residuals r for the sample i and the tree m

$$r_{im} = - \left[\frac{\partial L(y_i, f(x_i))}{\partial f(x_i)} \right]_{f=f_{m-1}} \quad \text{for } i = 1, 2, \dots, N \quad (\text{B.6})$$

b) Then there is the creation of the terminal regions R_{jm} fitting a regression tree to the targets r_{jm} with a number of leaves J_m . The terminal regions are the leaves of the tree.

c) For each leaf (for $j = 1, 2, \dots, J_m$) must be determined

$$\gamma_{jm} = -\arg \min_{\gamma} \sum_{x_i \in R_{jm}} L(y_i, f_{m-1}(x_i) + \gamma) \quad (\text{B.7})$$

d) Now a new prediction for each sample can be made

$$f_m(x) = f_{m-1}(x) + \nu \sum_{j=1}^{J_m} \gamma_{jm} I(x \in R_{jm}) \quad (\text{B.8})$$

where the factor $0 < \nu < 1$ is the learning rate which controls the shrinkage, scaling the contribution of each tree. As demonstrated in Ref. [104] small values of ν improve accuracy, but this choice requires a high number of tree M , increasing the computational time.

3. The third and final step consists in computing

$$\hat{f}(x) = f_M(x) \quad (\text{B.9})$$

where M is the last tree and $\hat{f}(x)$ is the GBM surrogate model.

The most used loss function is

$$L(y_i, f(x)) = \frac{1}{2} (y_i - f(x))^2 \quad (\text{B.10})$$

because its derivative is the negative of the residuals.

$$\frac{dL(y_i, f(x))}{df(x_i)} = -(y_i - f(x)) \quad (\text{B.11})$$

Appendix C

Neural Network based LV aerodynamic

This appendix presents a preliminary attempt to apply neural network-based identification techniques to obtain a data-driven reduced-order model for the aerodynamics of a launch vehicle.

Once the flow properties (Mach number) are fixed, the aerodynamic of a launch vehicle is determined exclusively by the LV profile and the angle of attack. For instance, in Fig. C.1(a) is displayed an LV profile and in Fig. C.1(b) its corresponding lateral force distribution. This distribution can be obtained by a CFD analysis or by an analytical ROM aerodynamic, however both these methods present criticizes: CFD is too expensive for MDO applications in terms of computational time, instead the analytical ROMs aerodynamic are not accurate, especially in transonic regime. Therefore, a viable approach consists in create an aerodynamic model based on neural networks. In Ref. [105] the aerodynamic of missiles is reconstructed using Artificial Neural Network Ensemble (ANNE) taking as input the geometrical parameters; while in Ref. [106] the aerodynamic coefficients are calculated via Convolutional Neural Network (CNN) considering as input the shape of missile.

The solution proposed here is to create a Recurrent Neural Network (RNN) based aerodynamic ROM to obtain the estimate of the lateral force distribution given the LV profile and the angle of attack (for a fixed Mach number). Specifically, the ROM is a Nonlinear Autoregressive Exogenous Model (NARX) (see Ref. [107]), which involves feedback from the estimated output passing through the delay lines (together with the input signal). This type of model is trained with time series to reproduce the dynamic behavior over time of the process to be identified. However, both the LV profile and lateral force distribution are a function of spatial discretization (along the axis of the LV). Therefore, to use the proposed model, it is necessary to consider the geometrical profile and lateral force as if they were signals in time, as shown in Figs. C.1(c) and C.1(d). By dividing the x component by the length of the LV, the axis changes between 0 and 1 along with the corresponding time signal. Thus, a dataset can be created generating different time signals (diverse LV profile) comprises between 0 and 1 second. An example of dataset is shown in Fig. C.2(a), which presents 4 different LV profiles in L/D similarity, where L and D are respectively the length and diameter of the launch vehicle. The chosen LV presents two different diameters, two shrinking factors, two angles of fairing and interstage. By using an analytical model presented in Sec. 2.5, it can be easily get the lateral force distribution envelopes shown in Fig. C.2(b). The use of analytical ROM is functional for the rapid demonstration of the proposed methodology. In fact, to obtain a more efficient and reliable reduced-order model of aerodynamics, it would be more suitable to generate the training data set with high-fidelity fluid dynamic simulations.

The proposed methodology provides a noticeable computational cost advantage. In fact, only a few simulations (whether fluid dynamic or analytical) are needed to train a network capable of returning an adequate estimate of the lateral force distribution. Specifically, preliminary results obtained by training a network with only 4 LV signals/profiles (the same shown in Fig. C.2(a)). In addition to them, two additional profiles necessary for model validation (to avoid overfitting on the training data) are also considered. Indeed, the neural network can interpolate profile signals inside this band and understand the correspondence between geometry and lateral force distribution. The scheme of the selected NN is displayed in Fig. C.3. The input is represented by the LV profile passing through 4 delay lines, the angle of attack and the estimate of the lateral force passing through one delay line (in feedback). The network has one hidden layer with 20 neurons having hyperbolic tangent sigmoid function as activation function. This kind of structure works as a universal approximator, thus guaranteeing the capability to map any continuous nonlinear function (see Ref. [108]).

The results are displayed in Fig. C.4. For three different LV profiles is shown the difference between ROM and neural network aerodynamic considering $AoA = 1\ deg$ and $Mach = 1.5$. The fitness is calculated as:

$$Fit = 100 \left(1 - \frac{|f_{NN} - f_{ROM}|}{|f_{NN} - \bar{f}_{ROM}|} \right) \quad (C.1)$$

where f_{NN} is the lateral force distribution obtained via neural network, f_{ROM} is the one obtained via ROM aerodynamic and \bar{f}_{ROM} is its mean value. The first profile in Fig. C.4(a) has a maximum radius of 1 m, with a considered angle of attack of 1 deg, the lateral force distribution (Fig. C.4(b)) presents a maximum of 0.05; the fitness between the ROM and NN curves is equal to 85 %. The second profile in Fig. C.4(a) presents a radius of 1.5 m, the lateral force distribution (Fig. C.4(b)) has a maximum of about 0.1; the fitness is equal to 86 %. The third profile in Fig. C.4(e) is cylindrical with a radius of 2 m, the maximum of lateral force distribution is 0.15 (Fig. C.4(f) and the fitness is 91 %.

The neural network have been trained on results provided by the analytical aerodynamic ROM, so a future development will consist in the creation of a dataset based on CFD simulations. Based on the type of dataset, the proposed methodology can be used to meet two different objectives. By collecting data as the profile geometry changes (as shown in Fig. C.2(a)) for a reference flight condition, a ROM can be trained to represent the aerodynamics inside the MDO loop (in place of the actual analytical aerodynamic ROM). On the other hand, by fixing the geometry of the profile and varying the flight conditions, a tool that describes the aerodynamics of a reference launch vehicle can be obtained quickly in order to make an appropriate sizing of the TVC.

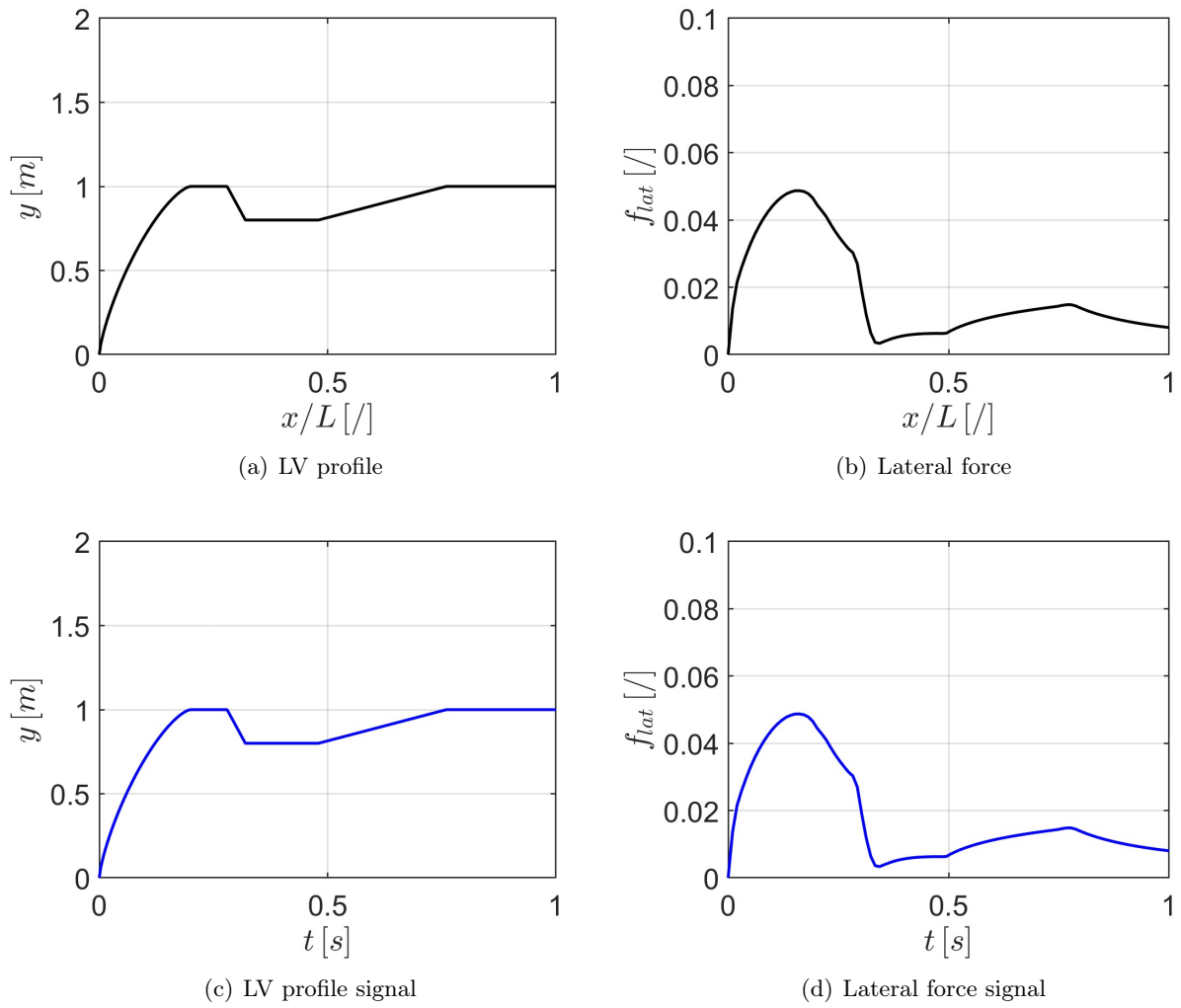


Figure C.1: LV axis from space to time discretization.

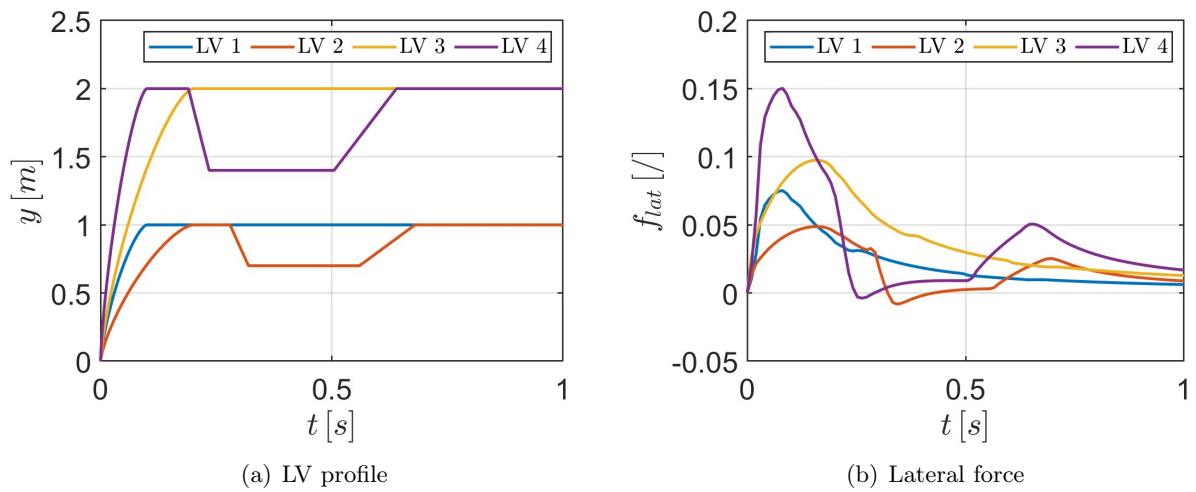


Figure C.2: Dataset for NN training and validation.

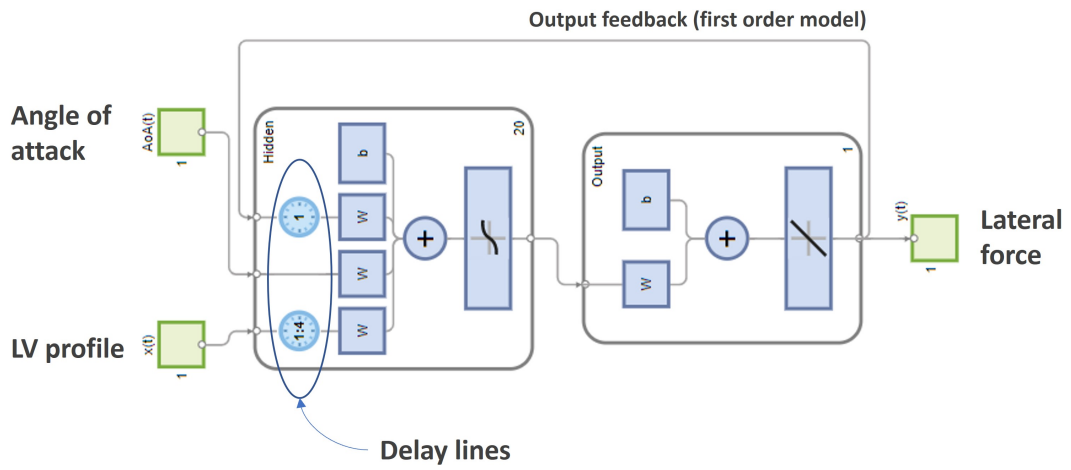
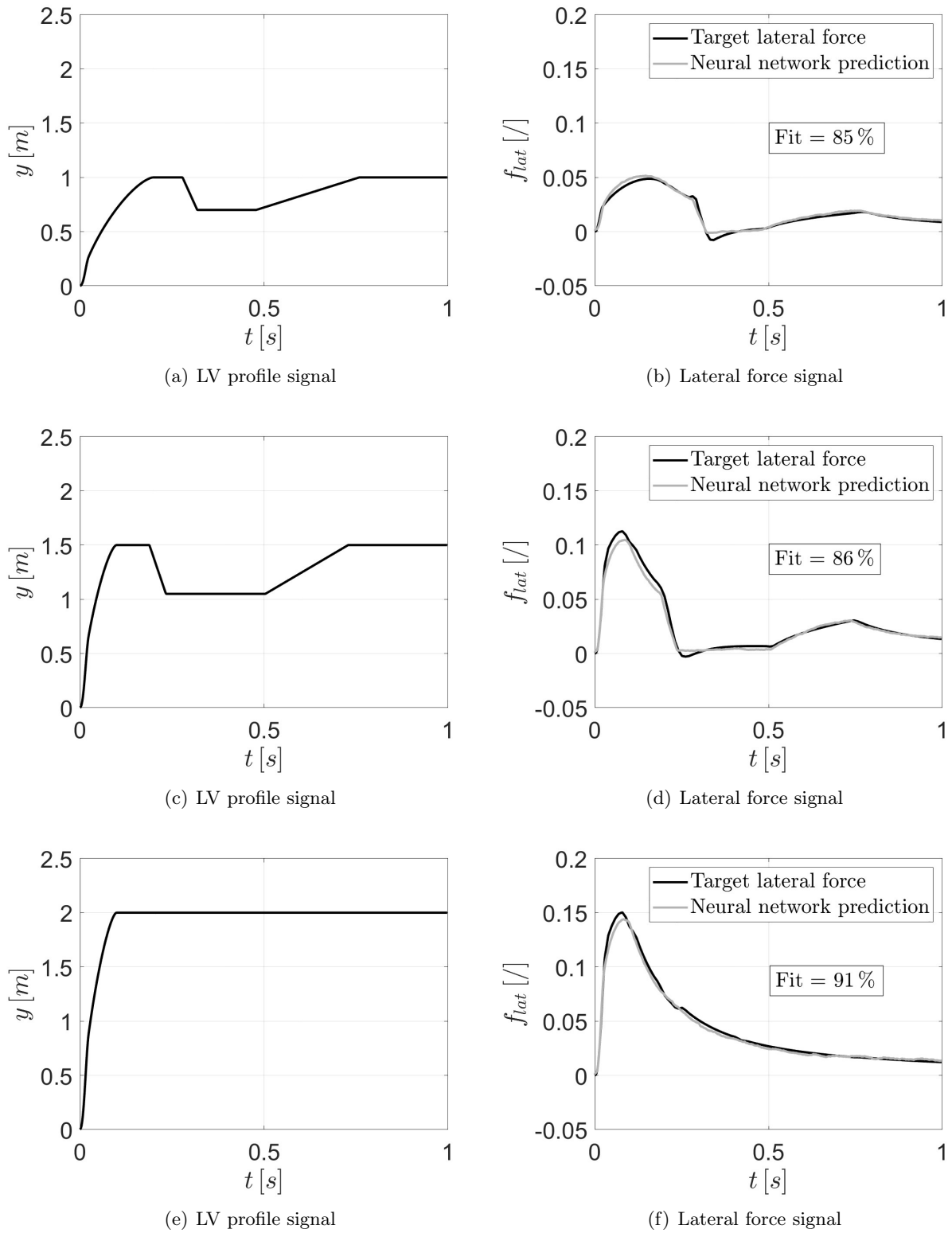


Figure C.3: Neural Network scheme.

**Figure C.4:** Neural Network LV aerodynamic results.

Acknowledgements

A multi-disciplinary thesis, it can only conclude with a multitude of thankfulness.

First and foremost, I would like to express my sincere gratitude to my thesis advisor Prof. Franco Mastroddi, who was always available to give me explanations about structures and optimization. His multidisciplinary vision has helped me a lot during these 3 years. In addition he, is very good from the human point of view in managing his research group, because before engineers we are people.

I am deeply thankful to my thesis co-advisor Eng. Agostino Neri of ESA ESRIN, who always gave me technical support to the entire period of the PhD. He possesses an impressive knowledge of launch vehicles from a system perspective. Talking to him is equivalent to reading many books on the subject. Without his vision this thesis would not exist.

Special thanks to research fellow Francesco Saltari, he taught me how to create a FEM model by highlighting the main features of the system. He makes very complex things easy.

Thanks also to Prof. Alessandro Zavoli for his contribution regarding trajectory analysis and the use of the genetic algorithm. When there is a problem he knows what to do.

Another big thank you to Prof. Fulvio Stella, he taught me everything I know about launch vehicle aerodynamics. He is very patient and conveys calmness in doing things.

To researcher Marco Pizzoli, thank you for teaching me how to make a surrogate model and neural network theory. The aerodynamics model based on neural networks was developed together with him.

Thanks to research fellow Luca Pustina, who recently helped me to make the optimization faster with his knowledge in the computational field.

Thanks also to PhD student Marta Colella, she is also doing a multidisciplinary optimization thesis, and many problems regarding MDO we solved together.

Another thanks to PhD student Leandro Lucchese, with whom the FEM model generator was developed during his master's thesis.

Finally, thanks to all the other Professors, students and staff in the Department of Mechanical and Aerospace Engineering who helped me even if only with advice or a coffee break.

Finiti i ringraziamenti istituzionali, è tempo di scrivere queste ultimissime righe in madrelingua. Il dottorato è stato come una lunga partita a scacchi e qui voglio ringraziare i miei "tifosi" che mi hanno supportato e sopportato durante questi 3 anni per dare "scacco matto" al problema trattato in questa tesi. Grazie a tutti i miei amici ed i miei famigliari, in particolare ai miei genitori per avermi fatto coltivare la passione per la matematica e lo spazio. Per ultima ma non per importanza voglio amorevolmente ringraziare mia moglie per essermi sempre stata accanto, soprattutto nei momenti più difficili, ed aver prestato attenzioni a nostra figlia nei periodi in cui ero impegnato a scrivere questa tesi. Ti prometto che da oggi passerò meno tempo con la testa tra le stelle e più tempo sulla Terra con te e la bambina.

Lucandrea Mancini, December 2023
